

UC Riverside

UC Riverside Electronic Theses and Dissertations

Title

Interfacing CsPbBr₃ Perovskite Nanocrystals for Efficient Charge Transfer

Permalink

<https://escholarship.org/uc/item/44w8s3f7>

Author

Tamayo, Jesse A.

Publication Date

2020

Copyright Information

This work is made available under the terms of a Creative Commons Attribution License, available at <https://creativecommons.org/licenses/by/4.0/>

Peer reviewed|Thesis/dissertation

UNIVERSITY OF CALIFORNIA
RIVERSIDE

Interfacing CsPbBr₃ Perovskite Nanocrystals for Efficient Charge Transfer

A Dissertation submitted in partial satisfaction
of the requirements for the degree of

Doctor of Philosophy

in

Chemistry

by

Jesse Alejandro Tamayo

September 2020

Dissertation Committee

Dr. Valentine Vullev, Chairperson

Dr. Yadong Yin

Dr. W. Hill Harman

Copyright by
Jesse Alejandro Tamayo
2020

The Dissertation of Jesse Alejandro Tamayo is approved:

Committee Chairperson

University of California, Riverside

Acknowledgements:

I want to express my extreme gratitude to my advisor Dr. Valentine Vullev. I am very thankful he accepted me into his group after I had departed my previous group. He provided me with several professional opportunities during my time with him which helped me grow as a person and professional. His vast knowledge in both life and science are things that I will never forget in my life.

Thank you to my committee members: Dr. Yadong Yin and Dr. Hill Harman for their participation and feedback afforded to me during my 5 years at UCR. Additionally, I would like to thank the entire chemistry department at UCR for the opportunities afforded me and the comradery I experienced in my time here. I truly believe UCR is a great place to learn to become a scientist.

I want to thank my fiancé and soon to be wife, Isabel, for always supporting me and my grumpiness during the past 5 years and for being an amazing mother to our two children Leonardo and Alessandra.

Thank you to all my past and present lab members who assisted me in projects or helped me understand a new task. Being able to learn from my peers has been an extremely helpful event during graduate school. I also want to thank several undergraduates I had the honor to mentor during my time as a graduate student. These include Danielle Hamilton, Maryann Morales, Cambria Bennett, Pauline Do, Tori Do, and Karen El-Maraghy.

Thank you to all the mentors and faculty who assisted me in my long journey. I have been so fortunate to have people be willing to impact my life in such a positive manner. This includes my time at a community college with Dr. Tatjana Omrcen and UC-Davis with Dr. William Casey.

ABSTRACT OF THE DISSERTATION

Interfacial Charge Transfer between CsPbBr₃ Nanocrystals and Electron Donating Molecules

by

Jesse Alejandro Tamayo

Doctor of Philosophy, Graduate Program in Chemistry
University of California, Riverside, September 2020
Dr. Valentine Vullev, Chairperson

Charge transfer (CT) is an essential part of life. Ubiquitous in nature, CT is the principal foundation for biological processes, solar-energy conversion and electronics.

Understanding CT processes at the molecular and nanoscale levels and interface between them is essential for energy science, biomedical advances, and organic electronics. As important as interfacing, or “wiring,” molecular moieties with conducting solid substrates is for materials and device development, it still remains a formidable challenge. Over the last decade lead halide perovskite compositions have attracted tremendous interests due to their uniquely promising electronic and optical properties. The dynamic nature of ligand binding to such materials makes the wiring of CT molecular moieties to them especially challenging.

Here we show how effective interfacing between semiconducting all inorganic CsPbBr₃ perovskite nanocrystals and electron donating molecules facilitates charge transfer. We illustrate the important dual benefits that a binding motif offers: (1) electronic coupling essential for efficient interfacial CT and (2) surface-trap passivation eliminating non-

radiative pathways of exciton deactivation. Aliphatic amines show the strongest known propensity for perovskite surfaces. We show that an increase in the amounts of such Lewis bases etches the perovskite material, changing the shape and size of the nanocrystals and degrading them. Our results demonstrate that concentration control allows for optimal loading of amine moieties on perovskite nanomaterials without compromising their morphology, permitting efficient interfacial CT even in non-polar media. These findings reinforce and open doors for a wide range of photonics and electronics applications including solar-energy conversion, photocatalysis and molecular electronics.

Table of Contents

Chapter 1. Introduction	1
Fundamental concepts of charge transfer.....	1
Thermodynamic considerations.....	2
Marcus Transition-State Theory for Analysis of Electron Transfer.....	6
Influence of Dipoles on Charge Transfer.....	12
Dipole effects in device design and engineering.....	13
How to translate what we have learned about CT from nature to materials and devices?.....	22
Single-molecule junctions.....	23
Junctions based on self-assembled monolayers.....	24
Junctions with multiscale architectures.....	28
Synthesis and optoelectronic properties of all inorganic halide perovskites.....	34
Summary.....	36
References.....	37
 Chapter 2: Title: Interfacial charge transfer for extracting holes from perovskite nanocrystals. Dual benefits from molecular “wiring”	50
Authors.....	50
Abstract.....	50
Author contributions.....	51
Introduction.....	51
Results and discussion.....	57
Synthesis of CsPbBr ₃ nanocrystals.....	57
Phenothiazine as hole acceptors and electrochemistry.....	59
Steady state optical spectroscopy.....	61
TEM and NC morphology and size distribution.....	63
¹ H-NMR ligand analysis.....	65
Time resolved optical spectroscopy.....	71
Global fit analysis via Poisson Distribution.....	74
Conclusions.....	80
Methods.....	81
References.....	82

Chapter 3: Title: Bidirectional Solvatofluorochromism of a Pyrrolo[3,2- <i>b</i>]pyrrole– Diketopyrrolopyrrole Hybrid.....	86
Authors and Affiliations.....	86
Abstract.....	86
Introduction.....	87
Experimental Section.....	90
Synthesis.....	90
Absorption and Emission Spectroscopy.....	92
Transient-Absorption Spectroscopy.....	92
Electrochemistry.....	93
Theoretical Calculations.....	94
Results and Discussion.....	95
Design and Synthesis.....	95
Optical properties of 1, 2, and 3.....	97
Theoretical Analysis.....	100
Electrochemical Properties of 1 and 2.....	105
Excited-State Dynamics.....	106
Conclusions.....	109
References.....	110
Appendix Title: Facile synthesis and cleaning of CsPbBr ₃ nanocrystals for high Photoluminesence.....	115
Authors.....	115
Introduction.....	115
Results and Discussion.....	116
Conclusions.....	124
References.....	125

List of Figures

Chapter 1:

Figure I-1: Molecular orbital diagram depicting examples of ground state ET.....	3
Figure I-2: Molecular orbital diagrams representing long range photoinduced charge transfer occurring via different mechanisms, involving photoexcitation.....	7
Figure I-3: Marcus state diagrams.....	8
Figure I-4: Summary image of Marcus theory.....	10
Figure I-5: Bioinspired molecular electrets based on anthranilamide with dipoles.....	14
Figure I-6: Molecular orbital diagrams showing the dipole effects on long range PET....	15
Figure I-7: General scheme for photoinduced water splitting at an electrode surface.....	32
Figure I-8: ABX_3 perovskite structure showing BX_6 octahedral and larger A cation occupied in cubo-octahedral site.....	34

Chapter 2:

Figure 1-1: $CsPbBr_3$ perovskite nanocrystals in the absence and presence of Ptz and Ptz-NH₂	58
Figure 1-2: Electrochemical properties of Ptz for different solvents.....	59
Figure 1-2b: Dependence of the reduction potentials for neat solvents on the Born polarity parameter.....	60
Figure 1-3: Optical properties of $CsPbBr_3$ NCs in the absence and presence of Ptz and Ptz NH ₂	62
Figure 1-4: 1H NMR analysis of suspensions of $CsPbBr_3$ NCs in deuterated benzene...	66
Figure 1-5: Time resolved spectroscopy analysis of $CsPbBr_3$ NCs, suspended in benzene.....	72

Chapter 3:

Figure 2-1: Absorption and fluorescence spectra of 1, 2, and 3 molecules.....	96
Figure 2-2: Dependence of photophysical properties of 1, 2, and 3 on solvent polarity represented in terms of the Onsager solvation function.....	99

Figure 2-3: TD-DFT analysis of the optical transitions of 3, with cyclohexane implemented as the solvation medium.....	103
Figure 2-4: Electrochemical and spectroelectrochemical properties 1 and 2.....	104
Figure 2-5: TA dynamics of 1, 2, and 3.....	106

Appendix:

Figure A-1: Steady state absorption and photoluminescence of CsPbBr ₃	117
Figure A-2: TCSPC decays.....	119
Figure A-3: NMR spectra illustrating concentration decrease.....	120
Figure A-4: NMR spectra comparison with solvent.....	121

List of Charts

Chapter 2:

Chart 2-1: N-alkylated phenothiazine derivatives selected for electron donors, along with thermodynamic considerations for interfacial CT with CsPbBr₃ Perovskite NCs.....55

Chapter 3:

Chart 3-1 Dyad system showing donor and acceptor molecules.87

List of Tables

Chapter 1:

Table 1-1: Parameters extracted from Poisson fitting.....	77
---	----

Chapter 2:

Table 2-1: Solvent dependence for photophysics on dyad.....	102
---	-----

Chapter 1

Introduction

The multifaceted aspects of charge transfer (CT) and charge transport (CTr) make life on Earth and the modern human civilization possible. Discussing the same processes in electronics and photonics reveals their broad importance. Understanding the ubiquity of CT and CTr in living and manmade systems advances CT science and transforms energy, materials and device engineering. The importance of CT and charge transport CTr for basic science and applied engineering should not be underestimated. The ability to control and guide charge transduction is of key importance for molecular and cell biology, for electronic design and development, and for energy science and engineering.¹⁻⁵

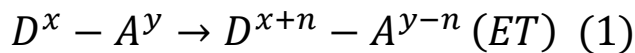
Fundamental concepts of charge transfer

Charge transfer, CT, involves transitions between well-defined single states. Conversely, transitions of electrons or holes between media with multiple states, such as conductors and semiconductors, are representative of charge transport (CTr). In biology, ion transport is another type of CTr that is crucially important for vitality of cells.^{39,40} Similar to the bridge in a D-B-A system, the media between two metallic or semiconductor surfaces can provide pathways for electron tunneling (Figure 3a). Such CTr mechanism encompasses *off-resonance* electron transport or hole transport depending if it involves transitions from the conduction or the valence bands, respectively.⁴¹ In contrast, *on-resonance* CTr involves electron or hole hopping along sites in the media connecting the

conducting or semiconducting surfaces (Figure 3b,c). While rate constants and $-\Delta G^{(0)}$ are features of CT processes, electrical currents and potentials are a principal means for characterizing CTr.

Thermodynamic considerations

CT encompasses a transition between two defined (electronic) states that have distinctly different charge distribution. As a sub-set of CT, electron transfer (ET) involves movement of negative charges, i.e., of electrons (e^-), whereas the changes in the nuclear geometry are small to negligible. Conversely, movement of the positively charged nuclei such as protons (H^+) represents another type of CT, e.g., proton transfer (PT). To preserve electroneutrality, frequently PT and ET occur in a concerted step, i.e., as a proton-coupled electron transfer (PCET).^{6,7} Photoexcitation that leads to opposite shifts in the pKa characteristics of two neighboring protonatable sites can lead to excited state proton transfer (ESPT).^{8,9} ET occurs between an electron donor (D) and an electron acceptor (A). Transferring n electrons from a donor to an acceptor causes a positive shift in the charge of the donor and a negative shift in the charge of the acceptor:



Where x and y are the charges of the donor and the acceptor, respectively, prior to ET. These changes in the charge states of the participating moieties make ET immensely susceptible to the local electric fields and to the solvating environment.

For thermodynamic feasibility of ET, the reduction potential of D^{x+n} should be more negative than the reduction potential of A^y , i.e., $E_{D^{x+n}|D^x}^{(0)} < E_{A^y|A^{y-n}}^{(0)}$, when estimated for the same solvent medium. It ensures that the energy level of the highest occupied molecular orbital (**HOMO**) of the donor is above that of the lowest unoccupied molecular orbital (**LUMO**) of the acceptor (Figure 1), providing favorable driving force, $-\Delta G_{ET}^{(0)}$, for ET in medium with dielectric constant ϵ :^{10,11}

Concurrently, the lowest unoccupied molecular orbital (LUMO) of the donor should also be above that of the acceptor. (fig 2)

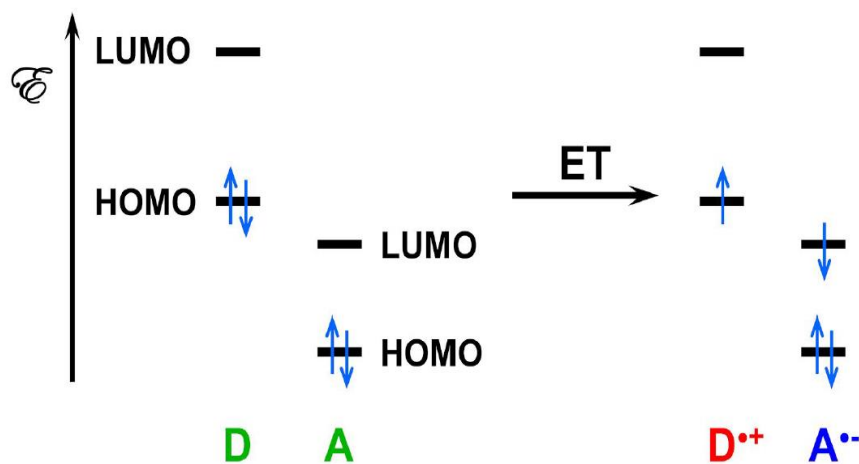
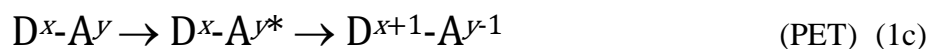
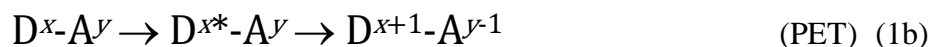


Figure 1 Molecular-orbital (**MO**) diagrams depicting examples of ground-state electron transfer.

As a side note, the accepted convention for standard electrochemical potentials is to report them as reduction potentials.¹² Namely, $E_{A^y/A^{y-1}}^{(0)}$ represents the one-electron reduction of the acceptor, $A^y + e^- \rightarrow A^{y-1}$, and corresponds the energy level of its LUMO. For the donor, $E_{D^{x+1}/D^x}^{(0)}$ corresponds to the energy level of its HOMO, but represents the reduction of its oxidized form, $D^{x+1} + e^- \rightarrow D^x$. That is, $E_{D^{x+1}/D^x}^{(0)}$ is a reduction potential of the oxidation of the donor. The reduction and oxidation potentials of the same process have opposite signs.¹³ This convention for using the reduction potentials for representing the electrochemical potentials causes two potential “confusions.” (1) While the reduction potentials linearly relate to the energy levels of the frontier orbitals, this relationship has inverse proportionality. Lowering the energy levels of the orbitals makes the species better electron acceptors and easier to reduce. Hence, as the energies of the frontier orbitals become more negative, the reduction potentials become more positive.¹² (2) The broadly used designation of the electrochemical potentials places the oxidized over the reduced form, i.e., $E_{Ox/Red}^{(0)}$, which seems to represent the oxidation process of the redox couple, $Red \rightarrow Ox + e^-$. When adding, rather than subtracting, the logarithmic term in the Nernst equation for a half-cell reaction, the activity of the oxidized form is in the numerator and the activity of the reduced form – in the denominator. Conversely, the convention for representing an electrochemical cell places the anode on the left and the cathode on the right side to ensure that the electrons flow from left to right. Therefore, for the cathode, along with the half-cell reduction, the oxidized species are on the left hand side and the the reduced – on the right, i.e., $Ox|Red$. Using slashes instead of vertical

lines in the designations of electrochemical and electronic devices is not uncommon and it seems to validate the use of $E_{\text{Ox/Red}}^{(0)}$ for reduction potentials. Strictly speaking, however, the reduction potentials should be represented as either $E_{\text{Red/Ox}}^{(0)}$ or $E_{\text{Ox|Red}}^{(0)}$.

The Rehm-Weller equation provides a facile means for quantifying the driving force of PET, expressed as the negative of the change in the Gibbs free energy, $-\Delta G_{ET}^{(0)}$, in terms of experimentally measurable quantities:^{10,11}

$$\Delta G_{ET}^{(0)} = F \left(E_{D^{x+1}|D^x}^{(0)} - E_{A^y|A^{y-1}}^{(0)} \right) - \mathcal{E}_{00} + \Delta G_s + W \quad (2a)$$

Where \mathcal{E}_{00} is the zero-to-zero energy, i.e., the excitation energy, of the donor or the acceptor; the Born solvation term, ΔG_s ,¹⁴ accounts for the variations in the solvation energy of the oxidized and reduced forms of the donor and the acceptor due to differences in the media for which the reduction potentials and \mathcal{E}_{00} are estimated;¹⁰ and W represents the donor-acceptor Coulomb interaction before and after PET.¹⁵ For one-electron ET processes:¹⁰

$$\Delta G_s = \frac{q_e^2}{8\pi\epsilon_0} \left(\frac{2x+1}{r_D} \left(\frac{1}{\epsilon} - \frac{1}{\epsilon_D} \right) - \frac{2y-1}{r_A} \left(\frac{1}{\epsilon} - \frac{1}{\epsilon_A} \right) \right) \quad (2b)$$

Where q_e is the electron charge; x and y are charge of the donor and the acceptor (eq. 1); r_D and r_A are the effective radii of the donor and the acceptor, respectively;¹⁶ ϵ_D and ϵ_A are the relative dielectric constants of the media for which the reduction potential of the donor and the acceptor, respectively, are recorded; and ϵ_0 is the dielectric constant of the media for PET and for which \mathcal{E}_{00} is estimated.

$$W = \frac{(y-x-1)q_e^2}{4\pi\epsilon_0\epsilon R_{DA}} \quad (2c)$$

Where R_{DA} is the center-to-center distance between the donor and the acceptor.

The Rehm-Weller equation provides thermodynamic considerations. It allows for testing if the photoinduced CT processes are possible and what the energy losses for the transition from the LE to CT states are. For evaluating the efficiency of CT and how it competes with other processes occurring in parallel, it is essential to resort to kinetic analysis.

Marcus transition-state theory for analysis of electron transfer

Marcus transition state theory provides a means for evaluating the rate constants of electron transfer and reactivity, k_{ET} , of ET:¹⁷ In the potential energy curves, represented by parabolic functions that show the state between the donor (D) and acceptor (A) or initial and final states of an electron transfer process. Calculations for k_{ET} are enabled through the seminal semiclassical expression (3a).

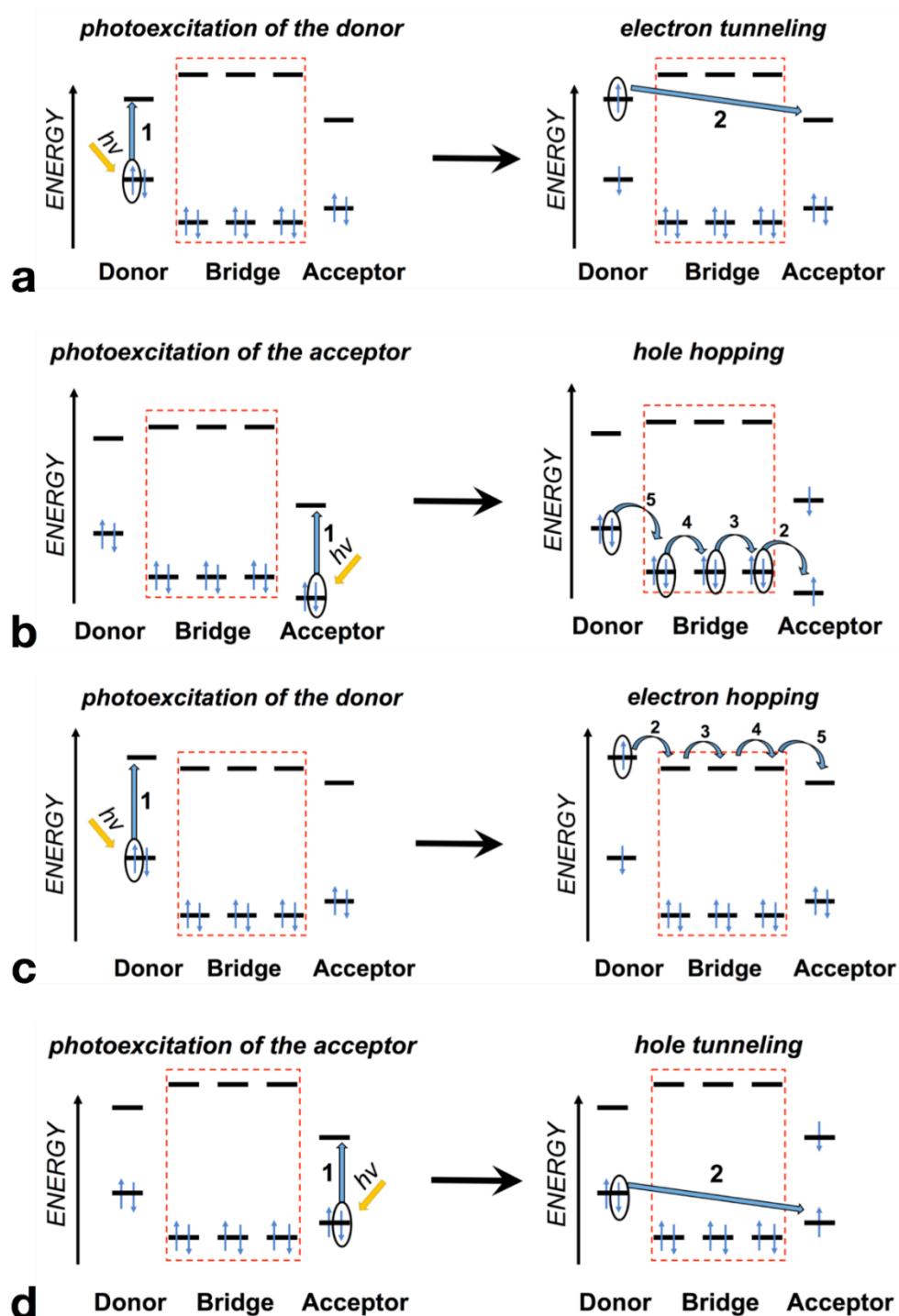


Figure 2 Molecular orbital diagrams representing long-range photoinduced charge transfer occurring via different mechanisms, involving photoexcitation, 1, followed by a sequence of discrete electron-transfer steps, 2 to 5. The transferred electrons are encircled.

$$k_{ET} = \frac{4\pi^2}{h} |H_{DA}|^2 \frac{1}{\sqrt{4\pi\lambda k_B T}} \exp\left(-\frac{(\lambda + \Delta G^0)^2}{4\lambda k_B T}\right) \quad (3a)$$

The equation has three essential variables that can be computed or determined experimentally. The first Marcus parameter is the Gibbs free energy change, ΔG^0 ,

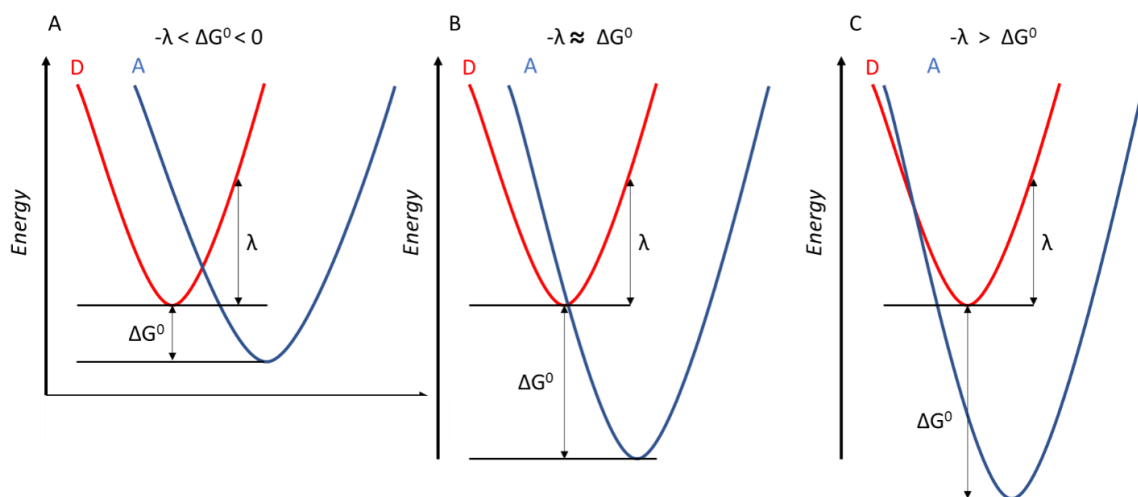


Figure 3 (A-C) State diagrams showing (A) Marcus normal region in which the rate of electron transfer increases with an increase in driving force, $-\Delta G^0$, because ΔG^\ddagger decreases as ΔG^0 becomes more negative, (B) Activationless region where $-\lambda \approx \Delta G^0$, and the potential energy surface of the acceptor crosses the bottom of the well of the donor. Hence, the free activation energy is equal to 0. (C) Marcus inverted region where the potential well of the acceptor crosses the donor at the furthest from the bottom of the potential energy surface of the final state. Thus, an increase in the driving force, $-\Delta G^0$, increases ΔG^\ddagger , and decreases the rate of the reaction.

commonly referred to as the driving force. The reorganization energy, λ , and electronic coupling between donor and acceptor H_{DA} are two other important variables. The electronic coupling can be described as the energy stabilization gained from interactions between the D and A wave functions. When H_{DA} is small

the process is generally referred to as *nonadiabatic* electron transfer. In relation to that, *adiabatic* electron transfer can occur when the electronic coupling is sufficiently large. The Planck constant, h , introduces the fundamental frequency.

In the potential energy curves, represented by parabolic functions that show the state between the donor (D) and acceptor (A) or initial and final states of an electron transfer process. (Fig. 2).

The transition-state energy, ΔG^\ddagger , for nonadiabatic processes involves a quadratic relationship:

$$\Delta G^\ddagger = \frac{((\lambda + \Delta G^\circ)^2)}{4\lambda} \quad (4)$$

This quadratic relationship defines two distinct regions of dependence of the electron-transfer kinetics on the thermodynamic characteristics of the system. When $-\lambda \approx \Delta G^\circ$, electron transfer is in an activationless regime of operation, placing the system at the tip of the Marcus curve (Fig 4.)

The Marcus normal region where ΔG° is less negative than $-\lambda$, i.e., $-\lambda < \Delta G^\circ < 0$, and k_{et} increases with an increasing driving force $-\Delta G^\circ$, which appears quite intuitive (Figure 3).

The Marcus inverted region is where $-\lambda$ is less negative than ΔG° , i.e., $-\lambda > \Delta G^\circ$, the electron transfer is a strongly exergonic process, and k_{et} decreases with an increasing driving force, $-\Delta G^\circ$, which appears somewhat counterintuitive (Figure 3).

Marcus-Hush formalism (eq. 1) aids the understanding of inner sphere electron transfer. This formalism accounts for the solvation effect of charge transfer as introduced by the

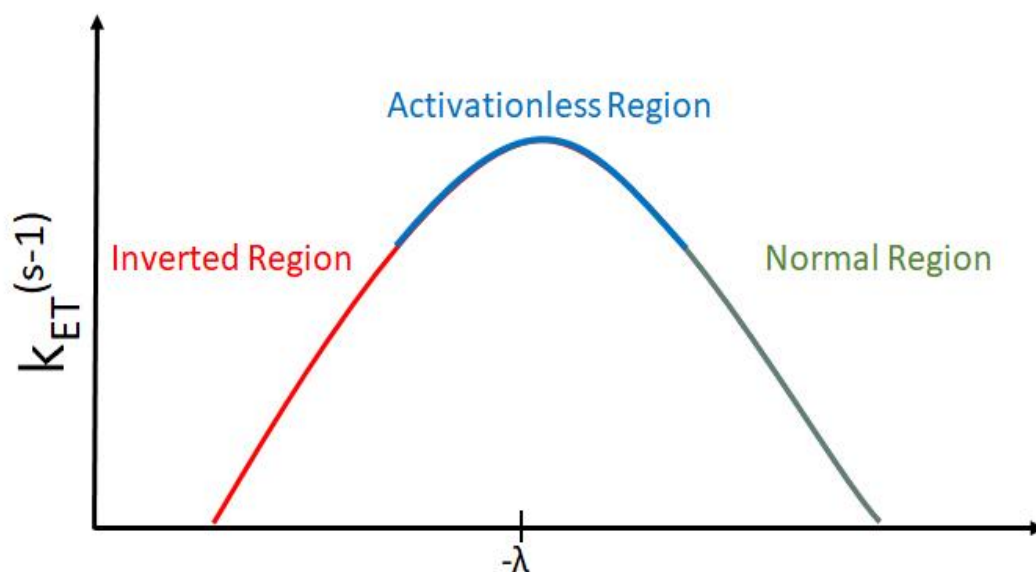


Figure 4 Summary of the Marcus theory showing the relationship between the rate constant and the driving force of the reaction, i.e., the rate of electron transfer increases with an increase in the driving force, to reach $-\lambda \approx \Delta G^\circ$, which corresponds to the activationless region. After this tip of the Marcus curve, as the driving force increases, the rates of electron transfer decreases, illustrating the inverted region.

outer-sphere (or medium) reorganization energy, λ_{outer} . The total reorganization energy, λ , therefore can thus be expressed as the sum of the inner (i.e., molecular reorganization) and the outer (i.e., solvent reorientation) nuclear modes:

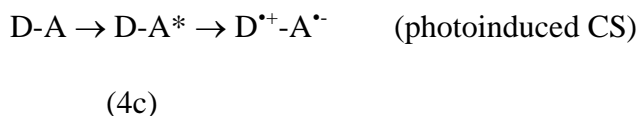
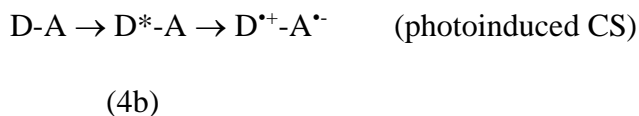
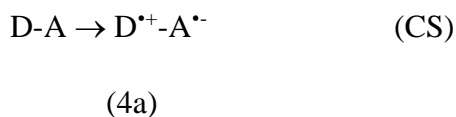
$$\lambda = \lambda_{inner} + \lambda_{outer} \quad (5)$$

This theory focusses on non-adiabatic processes, where the nuclei at the transition state do not move during the electron transfer, illustrating systems with weak donor-acceptor electronic coupling. For strong donor-acceptor electronic couplings, i.e., adiabatic electron transfer, the nuclear motion is coupled to the electron motion, and the “traditional” Marcus theory cannot account for such kinetics.

Furthermore, Marcus-Hush formalism assumes a normal distribution of density of vibrational states at the transition state, as reflected by the Gaussian function. Inclusion of specific frequencies (or an average of frequencies) of vibrational modes that contribute considerably to the electron transfer, as proposed by J. Jortner, leads to the Marcus-Levich-Jortner formalism

Considering that the lifetimes of LE states of good photosensitizers range from between sub-nano to microseconds, k_{ET} should be at least 10^6 s^{-1} , and ideally exceed 10^{10} s^{-1} , for attaining efficient photoinduced CT. It places limits on the feasible range of non-adiabatic CT since H_{if} tends to decrease exponentially with the donor-acceptor distances.

When the donor and the acceptor are not charged, i.e., $x = y = 0$, ET leads to charge separation (CS). That is, an electron moves from the donor to the acceptor leaving a positive charge, i.e., a hole (h^+), behind. ET, or PET specifically, leads to separating a positive from a negative charge:



Charge recombination (CR) encompasses the back ET that brings the CT state to the

ground state: $D^{\bullet+}-A^{\bullet-} \rightarrow D-A$ (CR)

(4d)

The concept of charge separation is not limited to non-charged donors and acceptors.¹⁸⁻²⁰

In general, ET always leads to a positive shift in the charge of the donor and negative shift in the charge of the acceptor (eq. 1). Regardless the initial changes of the CT moieties, during PET the LE state or the exciton dissociates to place an electron on the acceptor and a hole (i.e., a positive charge) on the donor (eq. 1b,c). Therefore, PET leads to separation of the charges composing the excitons, that is, to CS.

At a supramolecular and mesoscopic scales, CS can take on a different connotation. For bulk heterojunction (BHJ) media, for example, a CS state comprises an electrons and a hole that are sufficiently separated and/or energetically rich to prevent attractive interactions,²¹ i.e., the emphasis is on “separation” in the term “charge separation.” Conversely, a CT state in BHJ is Coulombically trapped at the interface between the donor and the acceptor media and can undergo efficient CR.^{22,23}

Influence of dipoles on charge transfer

Electric fields, and in particular local fields originating from molecular dipoles and ordered ion pairs, offer an invaluable means for guiding CT and CTr. Due to dielectric asymmetry, for example, only a single CT pathway is favorable in the bacterial photosynthetic reaction center (RC), despite its pseudo C_2 structural symmetry, i.e., two-fold radial symmetry.^{24,25} Furthermore, junctions containing such RC protein exhibit CTr

rectification.²⁶ Conversely, electric fields in the vicinity of active sites of enzymes affect their catalytic activity.²⁶⁻²⁹ (fig 5)

Since the 1960s, the idea about dipole effects on CT has gradually developed.^{24,25,30,31} In the late 1990s, the first reports providing direct experimental evidence about dipole-induced rectification of long range CT^{32,33} commenced the development of the field and the growth of the interest in this phenomenon. For the last half of a century, the focus has principally been on biological and biomimetic systems where polypeptide helices or polar groups in protein interior are the source of dipole-generated electric fields.^{32,34,35} The first examples involving donor–bridge–acceptor(D–B–A) systems, where the bridges are a polypeptide helices, illustrate a means for investigating CT kinetics for solution-based homogeneous conditions.³² Employing self-assembled monolayers (SAMs) of polypeptide helices on conducting surfaces furthers the field to exploration of interfacial CT.³⁶ Incorporating the similar helix SAMs in metal–insulator–metal (MIM) electrical junctions opens doors for bringing the field to CTr systems and device engineering.^{37,38}

Dipole effects in device design and engineering

Electronic devices comprising conjugated organic materials have a promising future as transistors⁴², rectifiers⁴³, photodetectors⁴⁴ and organic light emitting diodes (OLEDs)⁴⁵. In OLEDs, electrons and holes from metal electrodes into organic materials where they recombine and emit light. Efficient electron injection is an important aspect of the process and one method of improving efficiency is to modify the Schottky energy barrier. Indeed, the smaller the barrier the more efficient the electron and hole injections.

Modifying the electronic properties of materials interfaces renders immensely useful for design and development of devices.

In electronic devices, local fields originating from charge misbalance are intricate for materials interfaces. For organic and hybrid photovoltaics, for example, such interfacial fields may aid the photogenerated charge carrier to escape the Coulomb traps after the exciton dissociation.⁴⁶⁻⁴⁸ Introducing molecular dipoles to surface designs provides a means for modifying the interfacial fields, i.e., enhance them, change their direction, or cancel them, depending on the targeted functionality.

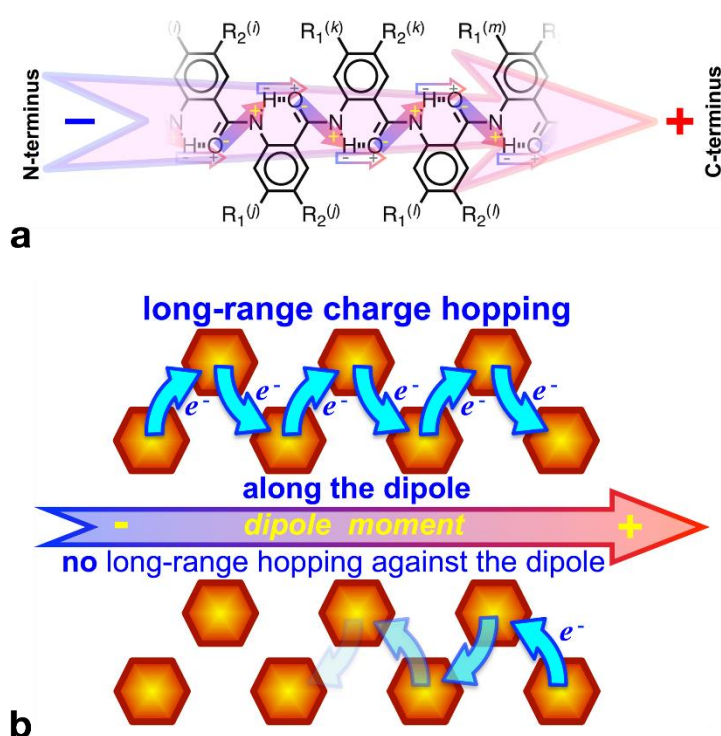
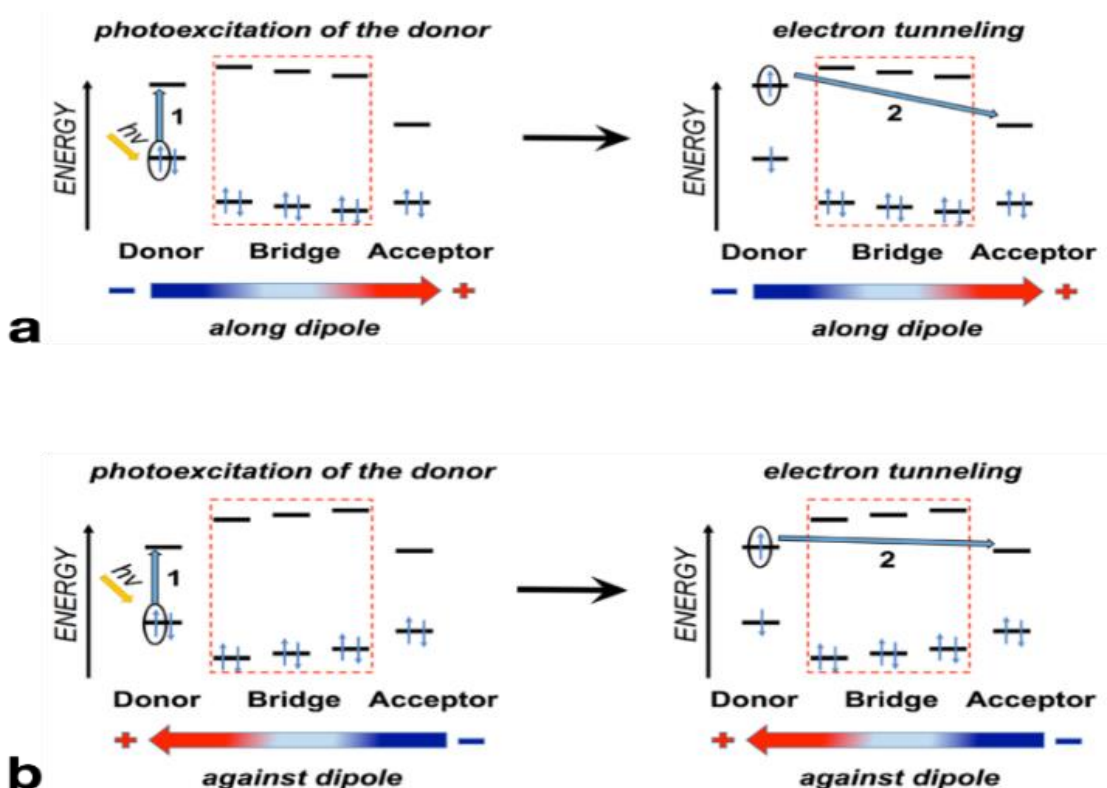


Figure 5 Bioinspired molecular electrets based on anthranilamide (Aa) motifs. (a) Origin of the ground-state electric macrodipole of Aa electrets from ordered orientation of the amide linkers and from the polarization due to the formation of the hydrogen bonds. (b) Long-range charge transduction mediated via electron hopping, or on-resonance electron transport, along the Aa residues and the effect of the macrodipole on the preferred directionality of the ET steps.

Placing permanent dipole on surfaces of conductors and semiconductors changes their effective work functions. Anchoring dipolar molecules as SAMs to a metallic substrate further modifies its work function due to the formation of an interfacial dipole originating from: (1) the push-back of the metal electrons, reduction of the intrinsic interfacial dipole, and (2) the charge redistribution resulting from the formation of bonds between the docking functional group and the metal surface. For example, the intrinsic dipoles of oligopeptides attached to gold nanoclusters change the reduction potentials of the oxidation of the metal particles.⁴⁹ When the dipoles point toward the gold surface they cause up to a 0.8-V positive shift in the reduction potentials.⁴⁹ Conversely, similar



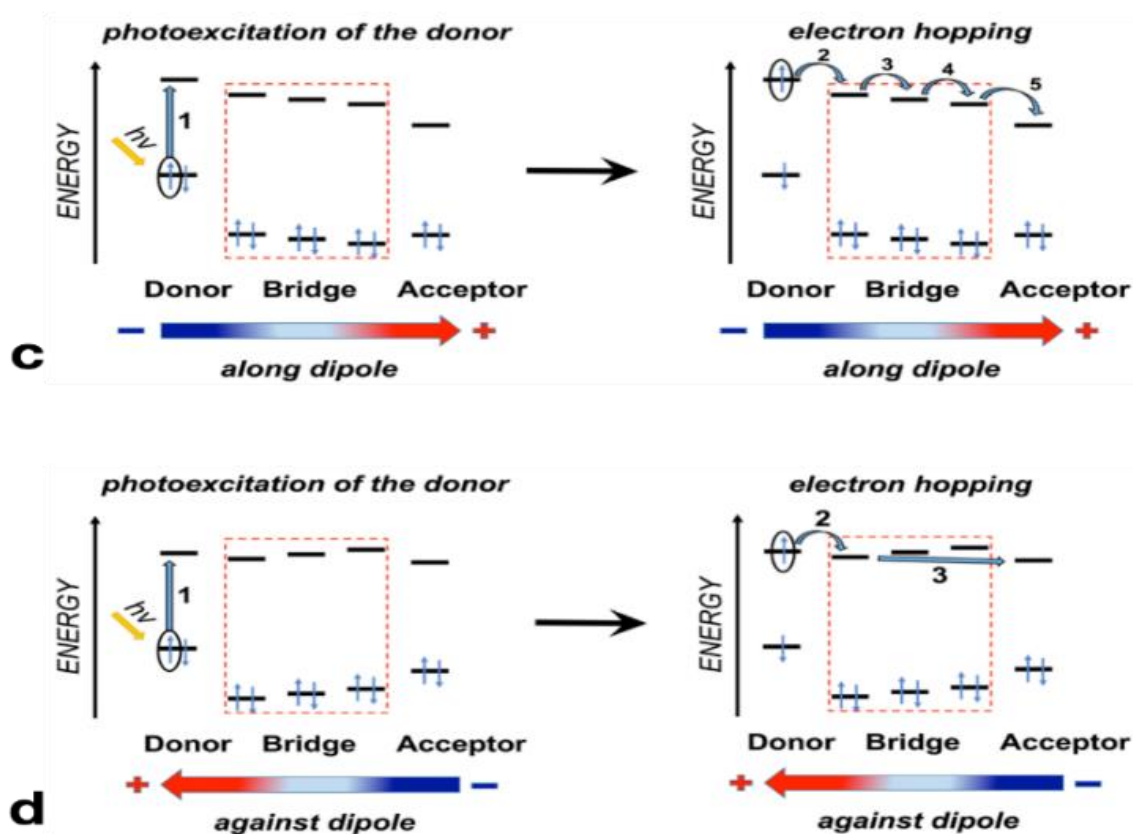


Figure 6 Molecular orbital diagrams showing the dipole effects on long-range PET occurring via different mechanisms, mediated by D–B–A conjugates. (a and b) For tunneling, or super-exchange mechanism, the photoexcitation, 1, is followed by a long-range electron tunneling step, 2. The electret dipole alters the energy levels of the frontier orbitals and, most importantly, the reduction potentials of the donor and the acceptor. Therefore, ΔG_{ET}^0 is different for ET along and against the dipole. (c) For electron hopping along the dipole, the photoexcitation, 1, is followed by multiple short tunneling steps, i.e., hopping steps, 2 to 5. The electret dipole alters the energy levels of the frontier orbitals generating cascade ET pathways along the bridge, i.e., each hopping step has $\Delta G_{ET}^0 < 0$, which is immensely beneficial for long range ET. In comparison, in the absence of a dipole, each hopping step has $\Delta G_{ET}^0 = 0$ (Fig. 2c). (d) For electron hopping against the dipole, the photoexcitation, 1, is followed by a hopping step, 2, and a long-range tunneling step, 3. The number of hopping steps for this case depends on the extent to which the dipole field shifts the energy levels of the frontier orbitals. The

polypeptides attached to mercury surface cause negative shifts in the reduction potential of an axillary redox pair regardless the orientation of their dipoles.⁵⁰ This discrepancy indicates that other factors overcome the expected effects from the peptide dipoles. Adsorption of ions presents a simpler manner for generating surface dipoles in comparison with forming SAMs of polar molecules. Such surface-charge electrets can impact significantly the performance of devices. Since the first reports by Grätzel *et al.*, dye-sensitized solar cells (DSSCs) have attracted considerable interest for their ability to convert solar light to electrical energy. In addition to the ruthenium-based photosensitizer, the initial designs employ lithium iodide as an electrolyte for the liquid junction and shuttling electrons from the cathode.⁵¹ Since the first reports, it has become known that additives such as lithium ions and 4-*tert*-butylpyridine (TBP) affect the power-conversion efficiency of DSSCs.^{52,53} It is commonly believed that the adsorption of Li⁺ ions affects the band energies of TiO₂. Incorporation of the small positive ions into the surface of the TiO₂ lattice causes positive shift of the electrochemical potential of the semiconductor,⁵⁴ and increases the driving force for electron injection from the photoexcited sensitizer. Indeed, the diffusion coefficient and the undesired CR kinetics correlates with the Li⁺ concentration.^{55,56} Evidences from transient absorption and electrochemical impedance spectroscopy suggest that improved electron injection efficiency is due to the interfacial dipole, pointing from the electrode to the electrolyte, originating from the lithium ions adsorbed on the titania nanocrystals, which in turn, facilitate exciton dissociation despite the small loss of photovoltage.⁵⁷⁻⁵⁹ In addition to affecting liquid junction, dipoles originated from adsorbed cations alter the properties of

junctions between solid materials. Dynamics of ions, responsible for the interfacial dipoles and the energy-conversion efficiency of DSSCs and perovskite devices, causes the hysteresis at low frequencies.⁶⁰

Surface dipoles from polar molecules attached to TiO₂ tunes the band-edge energies of the semiconductor and modulates the electron injection rates.⁶¹ Incorporating permanent dipoles in CT conjugates linking photosensitizers with the TiO₂ surface is an important handle for improving the performance of DSSC. Three analogous porphyrin-bridge-anchor derivatives, two of which contain oppositely-oriented intramolecular dipoles in the bridging unit, provide a means for examining this concept. Comparison between assemblies of these conjugates on the surface of mesoporous nanoparticle ZrO₂ films reveals *no* dipole effect on the electronic properties of the porphyrin.⁶² The dipoles of the same conjugates attached to TiO₂ cause 200-meV shift in its bands energies. The dipole orientation, however, has no noticeable effect on the electron-injection rates. The relatively small magnitude of the dipoles in the bridging conjugates is most likely the reason for the lack of observable effect on the CT kinetics.⁶³

Placing organic polar molecules, in an ordered manner, between two electrodes provides a means for controlling the *I-V* properties of the formed junctions. Molecular level rectification of the current is the most sought out property from such devices. These molecular or organic diodes mediate efficient CTr in one direction but not in the other, resulting in asymmetric *I-V* curves.

Metzger et al. utilize π -conjugated zwitterions as a CTr media for organic junctions.⁶⁴ Depositing monolayers or multilayers of such zwitterions between aluminum surfaces

yields a junction that manifests superior rectifying I - V behavior.⁶⁴ Placing non-charged molecules with dipoles ranging from 2.8 to 6.8 D between gold surface and gold nanoparticles results in molecular junctions with a pronounced rectifying behavior. The ratios between the magnitude of the electric current against and along the dipole range between 2 and 9 for junctions comprising molecules with different dipole magnitude.^{43,65,66}

Ensuing, replacement of the groups for binding the polar molecules to the gold surfaces from thiol to isocyanide results in a notable difference in rectification. This change in the anchoring groups causes more than two-fold reduction in the molecular dipole moment. Furthermore, calculations show a localization of the HOMO and LUMO on the terminal thiols, and delocalization of the frontier orbitals in the cyano-capped molecule.⁶⁷

Assemblies of identical QDs with ligands with different dipoles, and thus different band energies, can generate cascades for directing electron and hole transport, e.g.,

“unidirectional” or “bidirectional” configuration for charge-transport pathways.

Heterojunction PV devices, comprising such QD assemblies, show the favorability of the former, i.e., unidirectional configuration improves the power-conversion efficiency.⁶⁸ It is favorable because of a potential barrier for electrons or holes at the interface at different quantum dot layers.⁶⁸ The small size of the aromatic ligands ensures sufficient electronic coupling between neighboring QDs to ensure the efficiency of the interfacial charge transfer steps and of the long-range charge transport.

Coating silicon surfaces with small polar molecules with different dipole moments causes substantial effect on surface band bending and on the Si work function. Completing the

“wiring” of the molecules with a metal electrode yields a junction with pronounced rectifying characteristics.⁶⁹ Such metal-semiconductor junction form Schottky diodes with inherent dipole at the interface between the two materials. Intercalating polar organic SAMs between the metal and the semiconductor strongly affects the behavior of the Schottky diode. Metal-organic Schottky energy barriers follow ideal Schottky behavior. Namely, the electron Schottky barrier is determined by the energy difference between the metal work function and the electron affinity of the organic material, which is related to the reduction potential of the comprising molecules.⁷⁰ Thus, typically low work function metals are used for electron injection, and high work function metals – for hole injection.

Polar adsorbates allow for investigating the effects of a molecular dipole moment oriented both towards and away from an Ag electrode. These tests demonstrate control of the Schottky energy barrier. Specifically, when the dipole is oriented away from the electrode the energy barrier decreases; and when the dipole points toward the electrode the barrier increases.⁷¹ The Schottky barrier height for an n-type semiconductor, ϕ^b , is estimated as:

$$\phi^b = \phi^m - \chi^{SC} + eV^i \quad (7)$$

Where ϕ^m is the work function of the metal, χ^{SC} the electron affinity of the semiconductor, and V^i is the voltage drop due to an interface dipole which forms as a result of charge rearrangement upon the formation of the interface.⁷² Cahen *et al.* report

that molecular dipole monolayers as an effective tool for modifying barrier heights of Schottky junctions. The dipoles can affect both, ϕ^m and χ^{SC} of Au|SiO₂|Si diodes. Changing the terminal group from electron donating to electron withdrawing provides a means for altering the molecular dipole moment.^{73,74}

Employing polar molecules in junctions for attaining CTr rectification presents two important challenges: (1) ensuring sufficient length of the organic CTr pathway between the two conducting or semiconducting electrodes; and (2) ensuring symmetry of the wiring of the molecular species. Frequently, differences in the chemistry and the electronic properties of the manner of bonding of a molecule to the two electrodes may be the principal source of CTr rectification. Such asymmetry of the “wiring” to the electrodes can completely overcome any effect from the molecular dipoles.⁷⁵ When it comes to Schottky diodes, however, the semiconductor-metal junction is already asymmetric and the polar molecule only modify that asymmetry. Conversely, if the molecule is relatively small and strongly coupled electronically with the electrodes, the wave functions of the conducting substrate may penetrate through the whole molecule and perturb its electronic properties.⁷⁶ It may suppress the generated dipoles and eliminate the effects they may have.

Interfacing molecules with two electrodes presents some of the biggest challenges in the design of organic and molecular electronic devices. At the regions of molecular contacts, redistribution of the free charge carriers in the conducting substrates often may generate fields that overwhelm the effects of the molecular dipoles in the junction. Molecular

electrets that possess large dipoles and mediate long-range CT and CTr provide a means for eliminating the prevailing effect of the molecular contacts.

How to translate what we have learned about CT from nature to materials and devices?

Incorporating molecular and supramolecular species as a bridge in a DBA conjugate offer some of the best means for experimental characterization of their CT properties. The bridges can vary from small molecular moieties to large macromolecular and biomolecular assemblies. Placing the same bridging molecules and macromolecules in an electrical junction allows for characterizing their CTr properties and sets key foundations for device engineering.⁷⁷

The electrical molecular junctions are DBA systems with electrodes acting as a donor and an acceptor. Varying the potential difference between the electrodes varies the CTr driving forces, and the measured current flowing through it reveals the CTr efficiency. Furthermore, flipping the polarity of the applied voltage changes the position of the “donor” and the “acceptor” and the direction of the current. Therefore, the current-voltage (I-V) characteristics of a junction provides information about the CTr properties of the molecules incorporated in it. Such integration of organic and bioorganic conjugates in circuits and exploration of their CTr features has spun out the field of molecular electronics that has over 40 years of history.⁷⁸⁻⁸⁰

Single-molecule junctions

In the 1970s, the cornerstone report by Aviram and Ratner, describing the theoretical design of a molecular rectifier,⁸¹ has set the quest for single-molecule junctions and for deterministic effects that emerge from quantum phenomena.⁸²⁻⁸⁴ Like all single-molecule experiments, such electric junctions unveil the stochastic nature of nanoscale phenomena, which makes them unique tools for the CT and CTr science. The evolution of different experimental designs has allowed to address principal challenges with wiring of a molecule to two electrodes simultaneously.^{84,85}

Commonly, a molecule in a junction is orders of magnitude smaller than the electrodes to which it is attached,⁸⁶ making the formation of single-molecule junctions quite challenging. In break junctions, for example, freshly formed metal surfaces slowly recede from each other in a controllable manner while immersed in a diluted solution of the examined molecule, which is usually bifunctional.⁸⁷⁻⁸⁹

For imaging, scanning tunnelling microscopy (STM) utilizes the horizontal movement of a metal tip over a conducting surface with potential applied between them. Mapping the measured currents vs. the coordinates of the tip provides ångström-resolution images of the surface topology and thus, of the molecules adsorbed on it.⁹⁰ In addition, STM has introduced the capabilities for mechanical manipulation of surface structures.⁹¹ These features of STM provide an excellent means for formation of single-molecule junctions between the tip and the surface, and for interrogation of their I-V characteristics.⁹⁰

The electrical contacts of a molecule in a junction can have deterministic effects on its I-V performance.⁹² Some of the best means for incorporating a bifunctional molecule in a junction involves rapid formation of coordinate and covalent bonds with the conductive substrates of the two electrodes. Sulphur functional groups, such as thiols, thioethers and thioester, provides the most popular approach for attaching a molecule to gold electrodes in a that such covalent bonds not only are stable, but also provide strong electronic coupling.⁹³ The strength of the sulphur-gold bond is about 2 eV.⁹⁴

Junctions based on self-assembled monolayers

Translation from single-molecule setups to molecular ensembles illustrates an important path of evolution toward applied science and technology development.⁹⁵ Some of the initial work in molecular electronics involved electrical junctions comprising self-assembled monolayers (SAMs) sandwiched between flat metal electrodes.⁷⁹ Such metal-insulator-metal (MIM) junctions have the architecture of capacitors with dielectric layers that are nanometre-thick, allowing for efficient CTr (Figure 8). These devices bring molecular CTr to the realm of organic electronics.

One way to picture SAM devices is as a superposition of a large-number of parallel single-molecule junctions. Conversely, the molecules in such SAM junctions are closely packed together and the intermolecular electronic coupling provides parallel CTr pathways, especially when the SAM molecules assume large tilt angles on the conductive surfaces. Such CTr involving multiple pathways can lead to emergence of new properties of the molecular ensembles that are not inherent to the individual molecules.

Furthermore, incorporating π -conjugated CTr molecules in SAMs of alkyl conjugates allows for probing specifically the CTr moieties without interference from lateral intermolecular CT steps.^{96,97} Indeed, it is essential to prevent phase separation during the SAM formation, i.e., to ensure that the π -conjugated molecules do not cluster together forming isles in the alkyl SAM.

Attaining nanometre-thick layers extending throughout the large areas of the MIM junctions presents grave challenges for the fidelity of the SAMs and the electrode surfaces. While well-packed SAMs on atomically flat substrates are not too demanding to attain, the edges and the tips of the grains of many electrode materials are sites for defects in the surface coatings. Mercury is a liquid conductor with sufficient surface energy to always form atomically flat surfaces over areas of square millimetres and larger. Therefore, mercury has been the metal of choice for designs of MIM junctions.⁹⁸⁻¹⁰¹

The chemical inertness of gold has made it one of the most popular materials for electrodes in molecular electronics. The grainy nature of gold surfaces, however, presents inherent challenges for SAM MIM junctions. Depositing gold films on naturally flat substrates, such as mica, allows for overcoming the grainy nature of the metal surfaces. Lifting the mica off, exposes gold surfaces that, while composed of packed grains, adopt the topology of the flat substrates.¹⁰² Such flat metal surfaces are superior electrodes for MIM junctions.¹⁰³

Any pinhole defect can serve as a point of a short circuit and thoroughly compromise the performance of the device. Nevertheless, the balance of the interaction forces between the

self-assembling molecules, the substrate surface and the solvent can drive the formation of SAMs with high fidelity. Many SAMs of long molecules can even assume two-dimensional crystalline structures.¹⁰⁴⁻¹⁰⁷ The SAM molecules possess a functional group at one of their termini that can quickly form bonds with the substrate. In the initial phase, the molecules adsorb flat on the surface. Inherently, the intermolecular van der Waals interactions are always stronger than the interactions between these organic conjugates and the inorganic surfaces or the solvent, as the Hamaker constants can readily reveal (after all, like prefers like).¹⁰⁸ In alkyl SAMs, each methylene contributes about 0.07 eV to the heat of formation.¹⁰⁹ Therefore, as the surface density of the adsorbed species increases this balance between the van der Waals interactions drives the molecules to pack against each other (each molecule stretching nearly orthogonally to the surface) with their functional groups anchored to the substrate. The energetically favorable minimization of the contact area of each organic moiety with the inorganic surface and the solvent, while increasing the intermolecular contact area, drives the formation of such SAMs. Heating and occasional sonication during the self-assembly process aid the improvement of the quality of the molecular packing and the removal of the potential defects in the formed SAM.^{110,111}

The ease of self-assembly of organic thiols into tightly packed layers on gold and other coinage metals, has made these surface structures the most widely used SAMs in chemistry, physics, and biology, in the last three decades.^{93,94,112} The facile preparation of thiol SAMs has also impacted the field of molecular electronics.^{113,114} Bringing a hanging mercury drop, coated with thiol SAM, into contact with another metal surface, coated

with the same or different SAM, forms a MIM junction that allows for characterizing the CTr properties of the molecular assemblies sandwiched between the conductive interfaces.⁹⁸⁻¹⁰¹ Instead of using a liquid metal, bringing in contact two orthogonally oriented SAM-coated metal wires leads to the formation of a MIM junction.^{115,116} The curvature of the wires, that are usually micrometre thick, determines the area of such crossed-wire junctions and allows attainment of single-molecule contacts.¹¹⁵

Despite their immense popularity, however, SAMs of thiols on gold possess inherent properties that make them less than optimal for electronic applications. The susceptibility to oxidation of the sulphurs anchoring the organic molecules to the metal makes the SAMs vulnerable to damage and desorption, and under ambient conditions (even when immersed in protective liquid) their lack of durability sets major limitations. Therefore, using only freshly prepared thiol SAMs for the MIM junctions is essential for obtaining reliable and reproducible results.

On the other hand, silanization of silicon and metal-oxide substrates yields SAMs that are pronouncedly stable. SAMs of silanes, however, do not have the molecular order that thiol SAMs can achieve. Nevertheless, the immense durability of silane SAMs has made silanization a popular approach for introducing molecules into electrical junctions.^{117,118}

Silanization anchors the organic molecules to silicon via C-Si-O-Si bonding patterns and the presence of a thin insulating layer of SiO₂ between the organic moieties and the Si semiconducting phase is usually unavoidable.^{15,119,120} Attaching organic moieties directly to silicon via carbon-silicon bonds is the way to address this issue.^{121,122} The C-Si bonds

are immensely stable and the use of such organic coatings for passivating silicon surfaces is well established.^{121,122} Similar to alkylthiols on coinage metals and mercury, alkyls on silicon can form densely packed and ordered SAMs.¹²³⁻¹²⁵ Binding organic moieties to silicon directly via C-Si bonds is considerably more difficult and more involved than attaching thiols to gold. As a result, thiol SAMs on metals and chalcogenides have gained incomparable popularity for surface design and materials engineering.

Organic electronics offers countless functionalities that are easily attainable via established synthetic procedures. Electroconductive carbon materials provide excellent platforms not only for interfacing organic molecules in devices, but also for pursuing unprecedented possibilities for energy storage and energy conversion. Silicon electronics, on the other hand, is mature and responsible for countless technological breakthroughs of the 20th and 21st centuries. Silicon electronic, therefore, is here to stay. To take advantage of the countless functionalities of that organic electronics can offer, it is essential to interface it with silicon. Placing efforts and resources on developing C-Si interfaces will set the stage for unprecedented technological advances driven by the unique features of the carbon, organic and biomolecular electronics.

Junctions with multiscale architectures

In many electrical junctions, it suffices to attach the molecule to only one of the electrodes. Liquid solution, which is conductive or containing an electron shuttle, establishes a “remote” electrical contact with the other electrode. That is, the junction comprises molecules sandwiched between a solid electrode and a liquid. Such liquid

junctions have made enormous impacts on energy science and engineering, encompassing devices such as dye-sensitized solar cells (DSSCs), and other photoelectrochemical cells, along with various architectures for artificial photosynthesis and an “artificial leaf.” In fact, in the 19th century the first demonstration of the photovoltaic effect employed a liquid-junction device.

The liquid-mediated electric contact in such junctions permits significant freedoms for the geometry of the electrodes. DSSCs comprises an anode with highly porous morphology that not only provides a huge surface area for adsorbing monolayers of sensitizer, but also causes significant light scattering throughout the electrode active layer.¹²⁶

Avoiding the use of liquids, bulk-heterojunction (BHJ) PV devices comprise blends of electron-donor and electron-acceptor solid materials.¹²⁷ The intertwining donor and acceptor phases in BHJs ensure: (1) a large contact area between the two phases, across which the initial photoinduced CT occurs; and (2) a decrease in the required distances for exciton migration to a CT interface.^{128,129} The continuity of each phase provides electrical contact between the CT interface and the electrodes of the device.¹³⁰

While PV devices mediate the conversion of light radiation into electrical energy, light-emitting diodes (LEDs) convert electrical currents into light.¹³¹⁻¹³⁴ Furthermore, at a molecular level, CT strongly impacts the optical properties of the systems.⁹ In LEDs, CR produces excited states that deactivate radiatively. Nowadays, organic light-emitting diodes (OLEDs) are the mainstream in display technologies. Each new cell phone touts

the latest in display technologies. The 30-year development from laboratory research to mass production is truly phenomenal.^{135,136} Some of the latest developments encompass a variety of emitters that exhibit phosphorescence and thermally activated delayed fluorescence.¹³⁶ Hierarchical ultrastructures found in fireflies offer guidelines for bioinspired designs of OLED.¹³¹ DNA bases can serve as hole-injection and hole-transport media in such devices. Specifically, comparison between adenine- and uracil-containing polymers shows that OLEDs containing the former exhibit improved thermal and redox stability, as well as solvent resistance due to increased cross-linking in the organic media.¹³⁷ Biomimetic brightness-enhancement layers reduce the reflection at the interfaces leading to improvements in the illumination efficiency of LEDs.¹³⁸

The dominating common theme in molecular electronics is the focus on two-terminal devices. That is, the molecules serve as “wires,” rectifiers, light-energy converters, CT catalysts, and light emitters. How about three-terminal devices, such as transistors, and even molecular integrated circuits? The immense challenges for wiring a molecule to two electrodes make the thoughts about electricals contact at three different points of a nanometre-size objects sound absurd. Nevertheless, the designs of three-terminal molecular devices is already on the way.¹³⁹ Furthermore, a third terminal, such as a transistor gate, does not necessarily require a direct electrical contact with the CT media, it just needs to be able to modulate its CTr properties by applying electrical potentials. This way of thinking has made the field-effect transistor (FET) architectures immensely popular in molecular and organic electronics.^{140,141} Light illumination provides another alternative for affecting the CTr properties of molecular and organic devices and it can

serve as a “third terminal” in a device, which has set the stage for development of photosensors and numerous other optoelectronic devices.^{44,142} Another important discovery, which is still in the realm of basic science, encompasses the utility of infrared radiation for affecting selected vibrational modes in the moieties mediating CT, and in this way, modulating the CT and CTr properties of the molecular systems.^{143,144}

These examples illustrate how the discoveries in molecular and biological CT drive technological developments that have global impacts on improving our day-to-day lives. While many technologies are already mature, it is truly important to pursue novel ideas and paradigms that may appear as “unappealing investment” because currently they do not seem to have any direct application. Setting new ways of thinking at this point in time, however, is important for the technological impacts decades from now, and such “long-term investments” are key for sustainability of progress.

Photoelectrochemical (PEC) water splitting has shown potential as a route for renewable energy via solar energy.^{145,146} Photosynthetic cells such as (Fig XXX) convert light to electric power utilizing two redox systems: one reacting with holes at the surface of a semiconductor electrode such as TiO₂ (bandgap 3-3.2 eV and UV absorber) and the second reaction at the counter electrode with electrons. Water is oxidized to oxygen at the semiconductor photoanode and reduced to hydrogen at the cathode.

During water splitting, the contact between the electrode and electrolyte leads to a charge transfer process at the solid-liquid interface due to potential differences between the two

phases. This potential difference leads to an accumulation of charges at the interface which introduces band bending as shown in (fig 7).

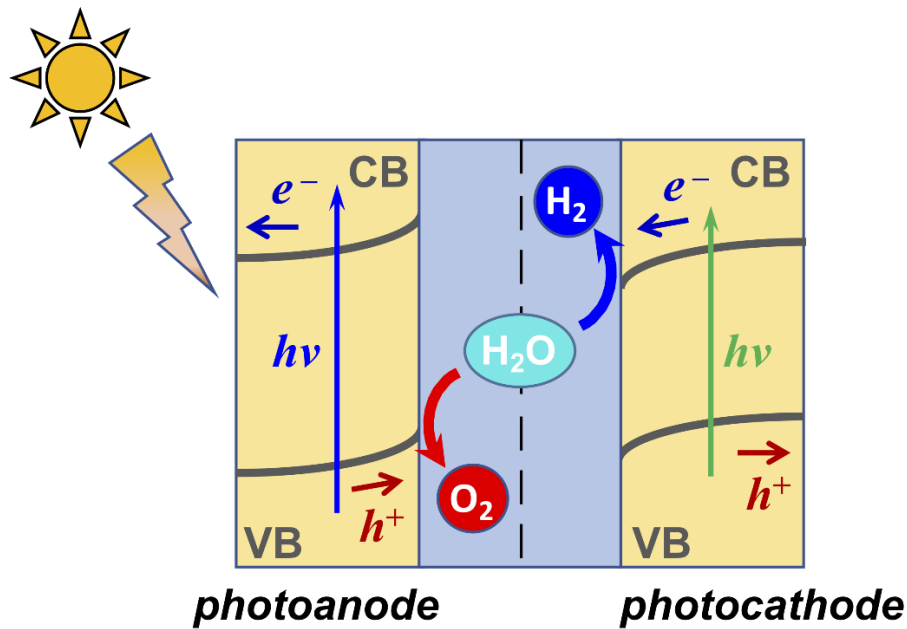


Figure 7 General scheme for photoinduced water splitting at an electrode surface.

One of the most studied transition metal oxides and archetypical photoactive electrode material is TiO_2 . TiO_2 exists in several polymorphs¹⁴⁷ with rutile and anatase the most common and stable among them. Both polymorphs form polarons with different behaviors. While both polymorphs form polarons, the rutile polymorph form localized small polarons easier in both pristine and defective rutile the same is not true of anatase which has only shown to form small polarons in samples with defects or vacancies.^{148,149}

A polaron is a quasiparticle formed by the interactions between charge carriers and lattice ion vibrations.¹⁵⁰ Two types of polarons, large and small, exist with the differences

between the two being defined by the strength of the electron-phonon coupling and extension of the lattice distortion near the electron. Small polarons exhibit weak coupling with large distortions. This distortion of the lattice, which stabilizes or traps a conduction electron, impedes the charge transport resulting in low mobilities and an upper limit of $0.1\text{-}1\text{ cm}^2\text{V}^{-1}\text{s}^{-1}$ having been calculated. The electron moves from site to site via a hopping mechanism facilitated by thermal energy.¹⁵¹

$$\rho(T) \propto T \exp\left(\frac{E_a}{k_B T}\right)$$

A variety of experimental techniques have been used to investigate the presence and mobility of small polarons in metal-oxides such as conductivity,¹⁵²⁻¹⁵⁴ EPR,^{155,156} STM,¹⁴⁸ optical¹⁵⁷ and IR spectroscopy.¹⁵⁸⁻¹⁶⁰ In fact, the first experimental observation of polarons are attributed to conductivity measurements as a function of temperature wherein increasing hole conductivity correlates with increased temperature which is a characteristic of small polaron hopping upon thermal activation. Typically, when reporting experimental observations, they may also be coupled with first principle modeling to help understand and interpret findings.

While no standardized data exists for charge mobility in TiO_2 , most of the data concerns electron mobility and shows that hole transport in TiO_2 is slower than electron transport.¹⁵⁰ Hole transfer in rutile has been shown to be adiabatic in nature along many directions while hole transfer in anatase is adiabatic only in one direction. Hole mobilities in rutile have been reported to be

$0.16 \text{ cm}^2\text{V}^{-1}\text{s}^{-1}$ with polaron lattice distortions greater for holes than electrons. Thus, polaron formation in transition metal oxides have shown to have a strong influence on the rate of charge transfer which is significant for PEC cell design and efficiency.

Synthesis and optoelectronic properties of all inorganic halide perovskites

The popularity of halide perovskites has grown immensely in the past ten years due to the unprecedented acceleration of the power conversion efficiency in thin film solar cells.¹⁶¹ Additionally, their low cost simple synthesis that yields variable color emission, high photoluminescence quantum yields (PLQYs), and outstanding excitonic and charge carrier properties make them quite useful in device applications such as LEDs, lasers, solar cells, and photodetectors. The base formula for halide perovskites is ABX_3 ,

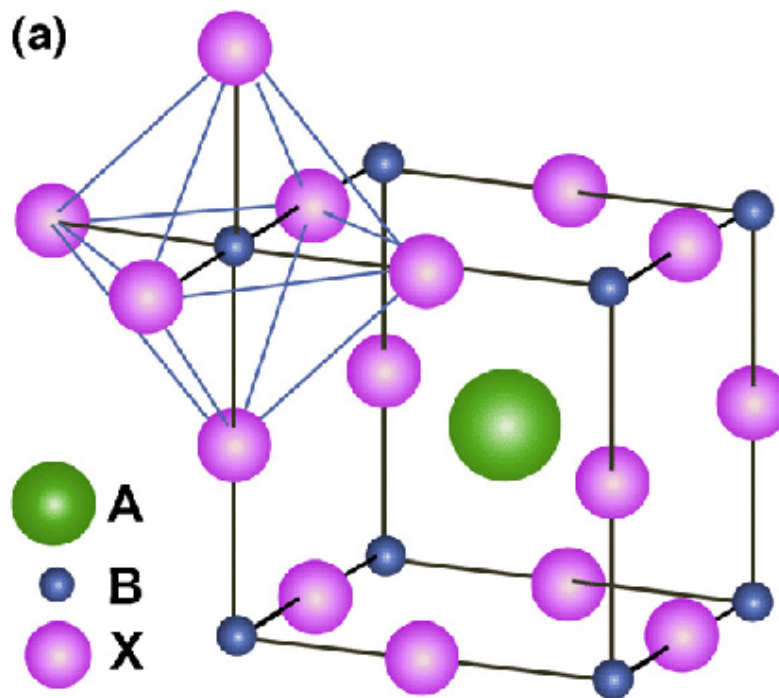


Figure 8 (a) ABX_3 perovskite structure showing BX_6 octahedral and larger A cation occupied in cubo-octahedral site.

(fig 8) where the A-site cation consists of Cs^+ , methylammonium (CH_3NH_3^+ , MA) or formamidinium [$(\text{CH}(\text{NH}_2)_2)^+$, FA] resides in the void formed by the corner sharing of BX_6 octahedra. Additional isomorphs can be synthesized by varying the B-site cation (Pb^{2+} , Sn^{2+} , Ge^{2+} , Bi^{3+} , In^{3+} or Sb^{3+}) or the X halides ($\text{X} = \text{Cl}^-$, Br^- , I^-). Multi-composition perovskite can also be made by mixing multiple cations or anions together in stoichiometric ratios.¹⁶²⁻¹⁶⁴ Like the chalcogenide nanoparticles, the perovskites bandgap and carrier confinement properties can be tuned by adjusting the halide composition and sizes of the particles.¹⁶⁵ The PL wavelength can be tuned from the visible to the near-infrared (NIR) region which can be achieved by either post-synthetic methods i.e. halide exchange or mixed halide precursors during synthesis. (Figure). The halide dependent emission tuning emerges from the bandgap changes of the band-edge states formed from the hybridized *s* and *p* orbitals of the halides and the B-site cations. (image). The exciton binding energies change as the halide composition changes thus changing the excitonic and charge carrier lifetimes. These lifetimes are also influenced by the A-site cation and the size of the particle.

During the standard synthesis of perovskite crystals the growth of the crystals can be confined to the nanometer scale by utilizing long chain organic ligands capped by carboxylic acids and amines. The typical synthesis is a hot injection method wherein the size and morphology can be controlled through ligand chain length and reaction temperature.¹⁶²

CsPbBr_3 nanocrystals used herein form a cubic phase regardless of halide when the temperature of the synthesis is between 120-200 °C.¹⁶² The nanocrystals are direct

bandgap semiconductors wherein the band edge of the halide perovskites is composed of the anti-bonding atomic orbitals of the $[\text{BX}_6]^{4-}$ octahedra.^{166,167} The conduction band minimum (CBM) is composed of the sigma (σ^*) and pie (π^*) antibonding orbitals that are formed by the hybridization of 6p-orbitals of lead and *s* and *p* orbitals of the halides. (fig). Conversely, the 6*s* and 6*p* orbitals of the halides form the valence band minimum (VBM).

The simple synthesis combined with exciting photophysical properties of halide perovskites has led to promising advanced in optoelectronics. The facile ability to modify the absorption and photoluminescence of perovskites makes studying these properties a worthwhile endeavor. Because of this my research utilized these exciting materials as a key component to understanding interfacial charge transfer.

Summary: My research has focused on and is impactful in the field of surface chemistry and the interfacing of perovskite CsPbBr_3 nanocrystals with redox active heterocyclic organic molecules. The research is designed to investigate a successful interface for perovskite nanocrystals while maintaining their stability and performance. Therein, the interfacing would incorporate dipole mediated CT and ultimately the possibility of device fabrication such as PV devices would use these dipolar molecules as interfacing agents that could control, rectify and enhance CT across the interface of nano sized materials with organic molecules.

References:

1. Rich, P.R. & Marechal, A. The mitochondrial respiratory chain. *Essays in Biochemistry: Mitochondrial Function* **47**, 1-23 (2010).
2. Gust, D., Moore, T.A. & Moore, A.L. Solar Fuels via Artificial Photosynthesis. *Accounts of Chemical Research* **42**, 1890-1898 (2009).
3. Karkas, M.D., Johnston, E.V., Verho, O. & Akermark, B. Artificial Photosynthesis: Photosynthesis: From Nanosecond Electron Transfer to Catalytic Water Oxidation. *Accounts of Chemical Research* **47**, 100-111 (2014).
4. Warren, J.J., Winkler, J.R. & Gray, H.B. Hopping maps for photosynthetic reaction centers. *Coordination Chemistry Reviews* **257**, 165-170 (2013).
5. Fukuzumi, S., Ohkubo, K. & Suenobu, T. Long-Lived Charge Separation and Applications in Artificial Photosynthesis. *Accounts of Chemical Research* **47**, 1455-1464 (2014).
6. Hammes-Schiffer, S. Proton-Coupled Electron Transfer: Moving Together and Charging Forward. *Journal of the American Chemical Society* **137**, 8860-8871 (2015).
7. Lennox, J.C., Kurtz, D.A., Huang, T. & Dempsey, J.L. Excited-State Proton-Coupled Electron Transfer: Different Avenues for Promoting Proton/Electron Movement with Solar Photons. *Acs Energy Letters* **2**, 1246-1256 (2017).
8. Wierzchowski, J. EXCITED-STATE PROTON TRANSFER AND PHOTOTAUTOMERISM IN NUCLEOBASE AND NUCLEOSIDE ANALOGS: A MINI-REVIEW. *Nucleosides Nucleotides & Nucleic Acids* **33**, 626-644 (2014).
9. Skonieczny, K. et al. How To Reach Intense Luminescence for Compounds Capable of Excited-State Intramolecular Proton Transfer? *Chemistry-a European Journal* **22**, 7485-7496 (2016).
10. Bao, D. et al. Electrochemical Oxidation of Ferrocene: A Strong Dependence on the Concentration of the Supporting Electrolyte for Nonpolar Solvents. *J. Phys. Chem. A* **113**, 1259-1267 (2009).
11. Rehm, D. & Weller, A. Kinetics of Fluorescence Quenching by Electron and H-Atom Transfer. *Israel Journal of Chemistry* **8**, 259-271 (1970).
12. Trasatti, S. The Absolute Electrode Potential - an Explanatory Note (Recommendations 1986). *Pure and Applied Chemistry* **58**, 955-966 (1986).
13. Latimer, W.M. THE SIGN OF OXIDATION-REDUCTION POTENTIALS. *Journal of the American Chemical Society* **76**, 1200-1201 (1954).

14. Born, M. Volumes and heats of hydration of ions. *Zeitschrift fuer Physik* **1**, 45-8 (1920).
15. Wan, J. et al. Solvent dependence of the charge-transfer properties of a quaterthiophene-anthraquinone dyad. *J. Photochem. Photobiol., A* **197**, 364-374 (2008).
16. Bao, D. et al. Electrochemical Reduction of Quinones: Interfacing Experiment and Theory for Defining Effective Radii of Redox Moieties. *J. Phys. Chem. B* **114**, 14467-14479 (2010).
17. Marcus, R.A. & Sutin, N. Electron Transfers in Chemistry and Biology. *Biochimica Et Biophysica Acta* **811**, 265-322 (1985).
18. Yonemoto, E.H. et al. Photoinduced Electron-Transfer in Covalently Linked Ruthenium Tris(Bipyridyl) Viologen Molecules - Observation of Back Electron-Transfer in the Marcus Inverted Region. *Journal of the American Chemical Society* **114**, 8081-8087 (1992).
19. Yonemoto, E.H. et al. Electron-Transfer Reactions of Ruthenium Trisbipyridyl-Viologen Donor-Acceptor Molecules - Comparison of the Distance Dependence of Electron-Transfer Rates in the Normal and Marcus Inverted Regions. *Journal of the American Chemical Society* **116**, 4786-4795 (1994).
20. Clark, C.D., Debad, J.D., Yonemoto, E.H., Mallouk, T.E. & Bard, A.J. Effect of oxygen on linked Ru(bpy)(3)(2+)-viologen species and methylviologen: A reinterpretation of the electrogenerated chemiluminescence. *Journal of the American Chemical Society* **119**, 10525-10531 (1997).
21. Savoie, B.M. et al. Unequal Partnership: Asymmetric Roles of Polymeric Donor and Fullerene Acceptor in Generating Free Charge. *Journal of the American Chemical Society* **136**, 2876-2884 (2014).
22. Savoie, B.M., Jackson, N.E., Chen, L.X., Marks, T.J. & Ratner, M.A. Mesoscopic Features of Charge Generation in Organic Semiconductors. *Accounts of Chemical Research* **47**, 3385-3394 (2014).
23. Heitzer, H.M., Savoie, B.M., Marks, T.J. & Ratner, M.A. Organic Photovoltaics: Elucidating the Ultra-Fast Exciton Dissociation Mechanism in Disordered Materials. *Angewandte Chemie-International Edition* **53**, 7456-7460 (2014).
24. Steffen, M.A., Lao, K.Q. & Boxer, S.G. DIELECTRIC ASYMMETRY IN THE PHOTOSYNTHETIC REACTION-CENTER. *Science* **264**, 810-816 (1994).
25. Tanaka, S. & Marcus, R.A. Electron transfer model for the electric field effect on quantum yield of charge separation in bacterial photosynthetic reaction centers. *Journal of Physical Chemistry B* **101**, 5031-5045 (1997).

26. Suydam, I.T., Snow, C.D., Pande, V.S. & Boxer, S.G. Electric fields at the active site of an enzyme: Direct comparison of experiment with theory. *Science* **313**, 200-204 (2006).
27. Sigala, P.A., Fafarman, A.T., Bogard, P.E., Boxer, S.G. & Herschlag, D. Do ligand binding and solvent exclusion alter the electrostatic character within the oxyanion hole of an enzymatic active site? *Journal of the American Chemical Society* **129**, 12104-+ (2007).
28. Fried, S.D. & Boxer, S.G. Response to Comments on "Extreme electric fields power catalysis in the active site of ketosteroid isomerase". *Science* **349**(2015).
29. Fried, S.D., Bagchi, S. & Boxer, S.G. Extreme electric fields power catalysis in the active site of ketosteroid isomerase. *Science* **346**, 1510-1514 (2014).
30. Hush, N.S. et al. Exchange Reactions and Electron Transfer Reactions Including Isotopic Exchange - General Discussion. *Discussions of the Faraday Society*, 113-136 (1960).
31. Boxer, S.G. MECHANISMS OF LONG-DISTANCE ELECTRON-TRANSFER IN PROTEINS - LESSONS FROM PHOTOSYNTHETIC REACTION CENTERS. *Annual Review of Biophysics and Biophysical Chemistry* **19**, 267-299 (1990).
32. Galoppini, E. & Fox, M.A. Effect of the electric field generated by the helix dipole on photoinduced intramolecular electron transfer in dichromophoric alpha-helical peptides. *Journal of the American Chemical Society* **118**, 2299-2300 (1996).
33. Fox, M.A. & Galoppini, E. Electric field effects on electron transfer rates in dichromophoric peptides: The effect of helix unfolding. *Journal of the American Chemical Society* **119**, 5277-5285 (1997).
34. Gao, J.A. et al. Electron Transfer in Peptides: The Influence of Charged Amino Acids. *Angewandte Chemie-International Edition* **50**, 1926-1930 (2011).
35. Kapetanaki, S.M., Ramsey, M., Gindt, Y.M. & Schelvis, J.P.M. Substrate electric dipole moment exerts a pH-dependent effect on electron transfer in Escherichia coli photolyase. *Journal of the American Chemical Society* **126**, 6214-6215 (2004).
36. Yasutomi, S., Morita, T., Imanishi, Y. & Kimura, S. A molecular photodiode system that can switch photocurrent direction. *Science* **304**, 1944-1947 (2004).
37. Sek, S., Swiatek, K. & Misicka, A. Electrical behavior of molecular junctions incorporating alpha-helical peptide. *Journal of Physical Chemistry B* **109**, 23121-23124 (2005).
38. Sek, S., Misicka, A., Swiatek, K. & Maicka, E. Conductance of alpha-helical peptides trapped within molecular junctions. *Journal of Physical Chemistry B* **110**, 19671-19677 (2006).

39. Doyle, D.A. et al. The structure of the potassium channel: Molecular basis of K⁺ conduction and selectivity. *Science* **280**, 69-77 (1998).
40. Dutzler, R., Campbell, E.B., Cadene, M., Chait, B.T. & MacKinnon, R. X-ray structure of a CIC chloride channel at 3.0 angstrom reveals the molecular basis of anion selectivity. *Nature* **415**, 287-294 (2002).
41. Simmons, J.G. Generalized Formula for Electric Tunnel Effect between Similar Electrodes Separated by a Thin Insulating Film. *Journal of Applied Physics* **34**, 1793-& (1963).
42. Sekitani, T., Zschieschang, U., Klauk, H. & Someya, T. Flexible organic transistors and circuits with extreme bending stability. *Nature Materials* **9**, 1015-1022 (2010).
43. Morales, G.M. et al. Inversion of the rectifying effect in diblock molecular diodes by protonation. *Journal of the American Chemical Society* **127**, 10456-10457 (2005).
44. Zhang, H. et al. Transparent Organic Photodetector using a Near-Infrared Absorbing Cyanine Dye. *Scientific Reports* **5**(2015).
45. Ly, K.T. et al. Near-infrared organic light-emitting diodes with very high external quantum efficiency and radiance. *Nature Photonics* **11**, 63-68 (2017).
46. Zhu, X.Y., Yang, Q. & Muntwiler, M. Charge-Transfer Excitons at Organic Semiconductor Surfaces and Interfaces. *Acc. Chem. Res.* **42**, 1779-1787 (2009).
47. Barbour, L.W., Hegadorn, M. & Asbury, J.B. Watching electrons move in real time: Ultrafast infrared spectroscopy of a polymer blend photovoltaic material. *Journal of the American Chemical Society* **129**, 15884-15894 (2007).
48. Lu, H. et al. Pyridine-coated lead sulfide quantum dots for polymer hybrid photovoltaic devices. *Adv. Sci. Lett.* **3**, 101-109 (2010).
49. Holm, A.H. et al. Effect of peptide ligand dipole moments on the redox potentials of Au-38 and Au-140 nanoparticles. *Langmuir* **22**, 10584-10589 (2006).
50. Becucci, L., Guryanov, I., Maran, F. & Guidelli, R. Effect of a Strong Interfacial Electric Field on the Orientation of the Dipole Moment of Thiolated Aib-Oligopeptides Tethered to Mercury on Either the N- or C-Terminus. *Journal of the American Chemical Society* **132**, 6194-6204 (2010).
51. Oregan, B. & Gratzel, M. A LOW-COST, HIGH-EFFICIENCY SOLAR-CELL BASED ON DYE-SENSITIZED COLLOIDAL TiO₂ FILMS. *Nature* **353**, 737-740 (1991).
52. Katoh, R. et al. Effects of 4-tert-Butylpyridine and Li Ions on Photoinduced Electron Injection Efficiency in Black-Dye-Sensitized Nanocrystalline TiO₂ Films. *Journal of Physical Chemistry C* **113**, 20738-20744 (2009).

53. Koops, S.E., O'Regan, B.C., Barnes, P.R.F. & Durrant, J.R. Parameters Influencing the Efficiency of Electron Injection in Dye-Sensitized Solar Cells. *Journal of the American Chemical Society* **131**, 4808-4818 (2009).
54. Kelly, C.A., Farzad, F., Thompson, D.W., Stipkala, J.M. & Meyer, G.J. Cation-controlled interfacial charge injection in sensitized nanocrystalline TiO₂. *Langmuir* **15**, 7047-7054 (1999).
55. Kambe, S., Nakade, S., Kitamura, T., Wada, Y. & Yanagida, S. Influence of the electrolytes on electron transport in mesoporous TiO₂-electrolyte systems. *Journal of Physical Chemistry B* **106**, 2967-2972 (2002).
56. Haque, S.A. et al. Parameters influencing charge recombination kinetics in dye-sensitized nanocrystalline titanium dioxide films. *Journal of Physical Chemistry B* **104**, 538-547 (2000).
57. Yu, Q.J. et al. High-Efficiency Dye-Sensitized Solar Cells: The Influence of Lithium Ions on Exciton Dissociation, Charge Recombination, and Surface States. *Acs Nano* **4**, 6032-6038 (2010).
58. Jennings, J.R. & Wang, Q. Influence of Lithium Ion Concentration on Electron Injection, Transport, and Recombination in Dye-Sensitized Solar Cells. *Journal of Physical Chemistry C* **114**, 1715-1724 (2010).
59. Bai, Y., Zhang, J., Wang, Y.H., Zhang, M. & Wang, P. Lithium-Modulated Conduction Band Edge Shifts and Charge-Transfer Dynamics in Dye-Sensitized Solar Cells Based on a Dicyanamide Ionic Liquid. *Langmuir* **27**, 4749-4755 (2011).
60. Contreras, L. et al. Specific cation interactions as the cause of slow dynamics and hysteresis in dye and perovskite solar cells: a small-perturbation study. *Physical Chemistry Chemical Physics* **18**, 31033-31042 (2016).
61. Meng, S. & Kaxiras, E. Electron and Hole Dynamics in Dye-Sensitized Solar Cells: Influencing Factors and Systematic Trends. *Nano Letters* **10**, 1238-1247 (2010).
62. Ngo, K.T. et al. Photoelectrochemical properties of porphyrin dyes with a molecular dipole in the linker. *Faraday Discussions* **185**, 497-506 (2015).
63. Nieto-Pescador, J. et al. Heterogeneous Electron-Transfer Dynamics through Dipole-Bridge Groups. *Journal of Physical Chemistry C* **120**, 48-55 (2016).
64. Metzger, R.M. et al. Unimolecular electrical rectification in hexadecylquinolinium tricyanoquinodimethanide. *Journal of the American Chemical Society* **119**, 10455-10466 (1997).

65. Jiang, P., Morales, G.M., You, W. & Yu, L.P. Synthesis of diode molecules and their sequential assembly to control electron transport. *Angewandte Chemie-International Edition* **43**, 4471-4475 (2004).
66. Oleynik, I.I., Kozhushner, M.A., Posvyanskii, V.S. & Yu, L. Rectification mechanism in diblock oligomer molecular diodes. *Physical Review Letters* **96**(2006).
67. Lee, Y.G., Carsten, B. & Yu, L. Understanding the Anchoring Group Effect of Molecular Diodes on Rectification. *Langmuir* **25**, 1495-1499 (2009).
68. Santra, P.K., Palmstrom, A.F., Tanskanen, J.T., Yang, N. & Bent, S.F. Improving Performance in Colloidal Quantum Dot Solar Cells by Tuning Band Alignment through Surface Dipole Moments. *Journal of Physical Chemistry C* **119**, 2996-3005 (2015).
69. Hiremath, R.K., Rabinal, M.K., Mulimani, B.G. & Khazi, I.M. Molecularly controlled metal-semiconductor junctions on silicon surface: A dipole effect. *Langmuir* **24**, 11300-11306 (2008).
70. Parker, I.D. CARRIER TUNNELING AND DEVICE CHARACTERISTICS IN POLYMER LIGHT-EMITTING-DIODES. *Journal of Applied Physics* **75**, 1656-1666 (1994).
71. Campbell, I.H. et al. Controlling Schottky energy barriers in organic electronic devices using self-assembled monolayers. *Physical Review B* **54**, 14321-14324 (1996).
72. Ishii, H., Sugiyama, K., Ito, E. & Seki, K. Energy level alignment and interfacial electronic structures at organic metal and organic organic interfaces. *Advanced Materials* **11**, 605-+ (1999).
73. Vilan, A., Shanzer, A. & Cahen, D. Molecular control over Au/GaAs diodes. *Nature* **404**, 166-168 (2000).
74. Selzer, Y. & Cahen, D. Fine tuning of Au/SiO₂/Si diodes by varying interfacial dipoles using molecular monolayers. *Advanced Materials* **13**, 508-+ (2001).
75. Jia, C.C. & Guo, X.F. Molecule-electrode interfaces in molecular electronic devices. *Chemical Society Reviews* **42**, 5642-5660 (2013).
76. Sayed, S.Y., Fereiro, J.A., Yan, H.J., McCreery, R.L. & Bergren, A.J. Charge transport in molecular electronic junctions: Compression of the molecular tunnel barrier in the strong coupling regime. *Proc. Natl. Acad. Sci. U. S. A.* **109**, 11498-11503 (2012).
77. Vuillaume, D. Molecular Electronics: From Single-Molecule to Large-Area Devices. *Chempluschem* **84**, 1215-1221 (2019).
78. Joachim, C., Gimzewski, J.K. & Aviram, A. Electronics using hybrid-molecular and mono-molecular devices. *Nature* **408**, 541-548 (2000).

79. Mann, B. & Kuhn, H. TUNNELING THROUGH FATTY ACID SALT MONOLAYERS. *Journal of Applied Physics* **42**, 4398-& (1971).
80. Polymeropoulos, E.E. & Sagiv, J. ELECTRICAL-CONDUCTION THROUGH ADSORBED MONOLAYERS. *Journal of Chemical Physics* **69**, 1836-1847 (1978).
81. Aviram, A. & Ratner, M.A. MOLECULAR RECTIFIERS. *Chemical Physics Letters* **29**, 277-283 (1974).
82. Reed, M.A., Zhou, C., Muller, C.J., Burgin, T.P. & Tour, J.M. Conductance of a molecular junction. *Science* **278**, 252-254 (1997).
83. Xu, B.Q. & Tao, N.J.J. Measurement of single-molecule resistance by repeated formation of molecular junctions. *Science* **301**, 1221-1223 (2003).
84. Nitzan, A. & Ratner, M.A. Electron transport in molecular wire junctions. *Science* **300**, 1384-1389 (2003).
85. Tao, N.J. Electron transport in molecular junctions. *Nature Nanotechnology* **1**, 173-181 (2006).
86. Prokopuk, N., Son, K.A. & Waltz, C. Free Standing Nanocrossbar Arrays with Molecular Throughput. *Nanoscience and Nanotechnology Letters* **2**, 96-101 (2010).
87. Azzaroni, O., Mir, M., Alvarez, M., Tiefenauer, L. & Knoll, W. Electrochemical rectification by redox-labeled bioconjugates: Molecular building blocks for the construction of biodiodes. *Langmuir* **24**, 2878-2883 (2008).
88. Bang, G.S. et al. High-fidelity formation of a molecular-junction device using a thickness-controlled bilayer architecture. *Small* **4**, 1399-1405 (2008).
89. Grunder, S. et al. Synthesis and Optical Properties of Molecular Rods Comprising a Central Core-Substituted Naphthalenediimide Chromophore for Carbon Nanotube Junctions. *European Journal of Organic Chemistry*, 478-496 (2011).
90. Ho, W. Single-molecule chemistry. *Journal of Chemical Physics* **117**, 11033-11061 (2002).
91. Binning, G., Rohrer, H., Gerber, C. & Weibel, E. SURFACE STUDIES BY SCANNING TUNNELING MICROSCOPY. *Physical Review Letters* **49**, 57-61 (1982).
92. Vilan, A., Aswal, D. & Cahen, D. Large-Area, Ensemble Molecular Electronics: Motivation and Challenges. *Chemical Reviews* **117**, 4248-4286 (2017).
93. Laibinis, P.E. et al. COMPARISON OF THE STRUCTURES AND WETTING PROPERTIES OF SELF-ASSEMBLED MONOLAYERS OF NORMAL-ALKANETHIOLS ON THE COINAGE METAL-SURFACES, CU, AG, AU. *Journal of the American Chemical Society* **113**, 7152-7167 (1991).

94. Nuzzo, R.G., Zegarski, B.R. & Dubois, L.H. FUNDAMENTAL-STUDIES OF THE CHEMISORPTION OF ORGANOSULFUR COMPOUNDS ON AU(111) - IMPLICATIONS FOR MOLECULAR SELF-ASSEMBLY ON GOLD SURFACES. *Journal of the American Chemical Society* **109**, 733-740 (1987).
95. Choi, H. & Mody, C.C.M. The Long History of Molecular Electronics: Microelectronics Origins of Nanotechnology. *Social Studies of Science* **39**, 11-50 (2009).
96. Bahng, H.W., Hagfeldt, A. & Moser, J.E. Donor Effect on the Photoinduced Interfacial Charge Transfer Dynamics of D- π -A Diketopyrrolopyrrole Dye Sensitizers Adsorbed on Titanium Dioxide. *Journal of Physical Chemistry C* **122**, 19359-19369 (2018).
97. Bahng, H.W., Hagfeldt, A. & Moser, J.E. Lateral Intermolecular Electronic Interactions of Diketopyrrolopyrrole D- π -A Solar Dye Sensitizers Adsorbed on Mesoporous Alumina. *Journal of Physical Chemistry C* **122**, 19348-19358 (2018).
98. Slowinski, K., Fong, H.K.Y. & Majda, M. Mercury-mercury tunneling junctions. 1. Electron tunneling across symmetric and asymmetric alkanethiolate bilayers. *Journal of the American Chemical Society* **121**, 7257-7261 (1999).
99. Slowinski, K. & Majda, M. Mercury-mercury tunneling junctions - Part II. Structure and stability of symmetric alkanethiolate bilayers and their effect on the rate of electron tunneling. *Journal of Electroanalytical Chemistry* **491**, 139-147 (2000).
100. Galperin, M., Nitzan, A., Sek, S. & Majda, M. Asymmetric electron transmission across asymmetric alkanethiol bilayer junctions. *Journal of Electroanalytical Chemistry* **550**, 337-0 (2003).
101. Tran, E., Cohen, A.E., Murray, R.W., Rampi, M.A. & Whitesides, G.M. Redox Site-Mediated Charge Transport in a Hg-SAM//Ru(NH₃)(6)(3+/2+)/SAM-Hg Junction with a Dynamic Interelectrode Separation: Compatibility with Redox Cycling and Electron Hopping Mechanisms. *Journal of the American Chemical Society* **131**, 2141-2150 (2009).
102. Rubtsov, I.V. Relaxation-Assisted Two-Dimensional Infrared (RA 2DIR) Method: Accessing Distances over 10 angstrom and Measuring Bond Connectivity Patterns. *Accounts of Chemical Research* **42**, 1385-1394 (2009).
103. Weiss, E.A. et al. Influence of defects on the electrical characteristics of mercury-drop junctions: Self-assembled monolayers of n-alkanethiolates on rough and smooth silver. *Journal of the American Chemical Society* **129**, 4336-4349 (2007).
104. Agina, E.V. et al. Formation of Self-Assembled Organosilicon-Functionalized Quinquethiophene Monolayers by Fast Processing Techniques. *Langmuir* **28**, 16186-16195 (2012).

105. Gholamrezaie, F. et al. Ordered Semiconducting Self-Assembled Monolayers on Polymeric Surfaces Utilized in Organic Integrated Circuits. *Nano Letters* **10**, 1998-2002 (2010).
106. Mikayelyan, E. et al. Real time studies of thiophene-based conjugated oligomer solidification. *Rsc Advances* **5**, 1319-1322 (2015).
107. Sizov, A.S. et al. Easily Processable Highly Ordered Langmuir-Blodgett Films of Quaterthiophene Disiloxane Dimer for Mono layer Organic Field-Effect Transistors. *Langmuir* **30**, 15327-15334 (2014).
108. Takenaga, M., Jo, S., Graupe, M. & Lee, T.R. Effective van der Waals surface energy of self-assembled monolayer films having systematically varying degrees of molecular fluorination. *Journal of Colloid and Interface Science* **320**, 264-267 (2008).
109. Love, J.C., Estroff, L.A., Kriebel, J.K., Nuzzo, R.G. & Whitesides, G.M. Self-assembled monolayers of thiolates on metals as a form of nanotechnology. *Chemical Reviews* **105**, 1103-1169 (2005).
110. Wang, H., Chen, S.F., Li, L.Y. & Jiang, S.Y. Improved method for the preparation of carboxylic acid and amine terminated self-assembled monolayers of alkanethiolates. *Langmuir* **21**, 2633-2636 (2005).
111. Cerruti, M. et al. Poly(ethylene glycol) monolayer formation and stability on gold and silicon nitride substrates. *Langmuir* **24**, 10646-10653 (2008).
112. Chang, S.C., Chao, I. & Tao, Y.T. STRUCTURES OF SELF-ASSEMBLED MONOLAYERS OF AROMATIC-DERIVATIZED THIOLS ON EVAPORATED GOLD AND SILVER SURFACES - IMPLICATION ON PACKING MECHANISM. *Journal of the American Chemical Society* **116**, 6792-6805 (1994).
113. Lukkari, J. et al. Organic thiosulfates (Bunte salts): Novel surface-active sulfur compounds for the preparation of self-assembled monolayers on gold. *Langmuir* **15**, 3529-3537 (1999).
114. Heimel, G., Romaner, L., Zojer, E. & Bredas, J.L. The interface energetics of self-assembled monolayers on metals. *Accounts of Chemical Research* **41**, 721-729 (2008).
115. Kushmerick, J.G. et al. Effect of bond-length alternation in molecular wires. *Journal of the American Chemical Society* **124**, 10654-10655 (2002).
116. Kushmerick, J.G. et al. Metal-molecule contacts and charge transport across monomolecular layers: Measurement and theory. *Physical Review Letters* **89**(2002).

117. Liu, G.S. et al. Comprehensive Stability Improvement of Silver Nanowire Networks via Self-Assembled Mercapto Inhibitors. *Acs Applied Materials & Interfaces* **10**, 37699-37708 (2018).
118. Min, H. et al. Ambient-ageing processes in amine self-assembled monolayers on microarray slides as studied by ToF-SIMS with principal component analysis, XPS, and NEXAFS spectroscopy. *Analytical and Bioanalytical Chemistry* **403**, 613-623 (2012).
119. Nanci, A. et al. Chemical modification of titanium surfaces for covalent attachment of biological molecules. *Journal of Biomedical Materials Research* **40**, 324-335 (1998).
120. Luderer, F. & Walschus, U. Immobilization of oligonucleotides for biochemical sensing by self-assembled monolayers: Thiol-organic bonding on gold and silanization on silica surfaces. *Immobilisation of DNA on Chips I* **260**, 37-56 (2005).
121. Linford, M.R., Fenter, P., Eisenberger, P.M. & Chidsey, C.E.D. ALKYL MONOLAYERS ON SILICON PREPARED FROM 1-ALKENES AND HYDROGEN-TERMINATED SILICON. *Journal of the American Chemical Society* **117**, 3145-3155 (1995).
122. Grandbois, M., Beyer, M., Rief, M., Clausen-Schaumann, H. & Gaub, H.E. How strong is a covalent bond? *Science* **283**, 1727-1730 (1999).
123. Ito, T., Namba, M., Buhlmann, P. & Umezawa, Y. Modification of silicon nitride tips with trichlorosilane self-assembled monolayers (SAMs) for chemical force microscopy. *Langmuir* **13**, 4323-4332 (1997).
124. Yang, J.Y.M. & Frank, C.W. Composition of binary self-assembled monolayers of alkyltrichlorosilanes. in *Organic Thin Films: Structure and Applications*, Vol. 695 (ed. Frank, C.W.) 67-80 (1998).
125. Appelhans, D. et al. Self-assembled monolayers prepared from omega-thiophene-functionalized n-alkyltrichlorosilane on silicon substrates. *Colloids and Surfaces a-Physicochemical and Engineering Aspects* **161**, 203-212 (2000).
126. Hwang, K.J., Park, D.W., Jin, S.H., Kang, S.O. & Cho, D.W. Influence of dye-concentration on the light-scattering effect in dye-sensitized solar cell. *Materials Chemistry and Physics* **149**, 594-600 (2015).
127. Park, H.J. & Guo, L.J. Advanced Manufacturing Technology of Polymer Photovoltaic Cells. *Progress in High-Efficient Solution Process Organic Photovoltaic Devices: Fundamentals, Materials, Devices and Fabrication* **130**, 349-373 (2015).
128. Lee, H., Park, C., Sin, D.H., Park, J.H. & Cho, K. Recent Advances in Morphology Optimization for Organic Photovoltaics. *Advanced Materials* **30**(2018).

129. Pivrikas, A., Neugebauer, H. & Sariciftci, N.S. Influence of processing additives to nano-morphology and efficiency of bulk-heterojunction solar cells: A comparative review. *Solar Energy* **85**, 1226-1237 (2011).
130. Sandberg, O.J., Sundqvist, A., Nyman, M. & Osterbacka, R. Relating Charge Transport, Contact Properties, and Recombination to Open-Circuit Voltage in Sandwich-Type Thin-Film Solar Cells. *Physical Review Applied* **5**(2016).
131. Kim, J.J. et al. Biologically Inspired Organic Light-Emitting Diodes. *Nano Letters* **16**, 2994-3000 (2016).
132. Petrova, P. & Tomova, R. Materials used for organic light-emitting diodes - organic electroactive compounds. *Bulgarian Chemical Communications* **41**, 211-225 (2009).
133. Rogach, A.L. et al. Light-emitting diodes with semiconductor nanocrystals. *Angewandte Chemie-International Edition* **47**, 6538-6549 (2008).
134. Tomova, R., Petrova, P., Buroff, A. & Stoycheva-Topalova, R. Organic light-emitting diodes (OLEDs) - the basis of next generation light-emitting devices. *Bulgarian Chemical Communications* **39**, 247-259 (2007).
135. Kaur, H. et al. Luminescent metal-organic frameworks and their composites: Potential future materials for organic light emitting displays. *Coordination Chemistry Reviews* **401**(2019).
136. Salehi, A., Fu, X.Y., Shin, D.H. & So, F. Recent Advances in OLED Optical Design. *Advanced Functional Materials* **29**(2019).
137. Cheng, C.C. et al. New bioinspired hole injection/transport materials for highly efficient solution-processed phosphorescent organic light-emitting diodes. *Nano Energy* **13**, 1-8 (2015).
138. Nien, C.K. & Yu, H.H. The applications of biomimetic cicada-wing structure on the organic light-emitting diodes. *Materials Chemistry and Physics* **227**, 191-199 (2019).
139. Wang, B. et al. A bundled-stack discotic columnar liquid crystalline phase with inter-stack electronic coupling. *Chemical Communications* **51**, 11837-11840 (2015).
140. Dimitrakopoulos, C.D. & Malenfant, P.R.L. Organic thin film transistors for large area electronics. *Advanced Materials* **14**, 99-+ (2002).
141. Coropceanu, V. et al. Charge transport in organic semiconductors. *Chemical Reviews* **107**, 926-952 (2007).
142. D'Souza, F. & Ito, O. Supramolecular donor-acceptor hybrids of porphyrins/phthalocyanines with fullerenes/carbon nanotubes: electron transfer,

- sensing, switching, and catalytic applications. *Chemical Communications*, 4913-4928 (2009).
143. Lin, Z.W. et al. Modulating Unimolecular Charge Transfer by Exciting Bridge Vibrations. *Journal of the American Chemical Society* **131**, 18060-+ (2009).
 144. Xiao, D.Q., Skourtis, S.S., Rubtsov, I.V. & Beratan, D.N. Turning Charge Transfer On and Off in a Molecular Interferometer with Vibronic Pathways. *Nano Letters* **9**, 1818-1823 (2009).
 145. Gratzel, M. Photoelectrochemical cells. *Nature* **414**, 338-344 (2001).
 146. Bard, A.J. & Fox, M.A. ARTIFICIAL PHOTOSYNTHESIS - SOLAR SPLITTING OF WATER TO HYDROGEN AND OXYGEN. *Accounts of Chemical Research* **28**, 141-145 (1995).
 147. Zhang, M.L., Chen, T.D. & Wang, Y.J. Insights into TiO₂ polymorphs: highly selective synthesis, phase transition, and their polymorph-dependent properties. *Rsc Advances* **7**, 52755-52761 (2017).
 148. Setvin, M. et al. Direct View at Excess Electrons in TiO₂ Rutile and Anatase. *Physical Review Letters* **113**(2014).
 149. Setvin, M. et al. Charge Trapping at the Step Edges of TiO₂ Anatase (101). *Angewandte Chemie-International Edition* **53**, 4714-4716 (2014).
 150. Deskins, N.A. & Dupuis, M. Intrinsic Hole Migration Rates in TiO₂ from Density Functional Theory. *Journal of Physical Chemistry C* **113**, 346-358 (2009).
 151. Holstein, T. STUDIES OF POLARON MOTION .1. THE MOLECULAR-CRYSTAL MODEL. *Annals of Physics* **8**, 325-342 (1959).
 152. Nagels, P., Denayer, M. & Devreese, J. ELECTRICAL PROPERTIES OF SINGLE CRYSTALS OF URANIUM DIOXIDE. *Solid State Communications* **1**, 35-40 (1963).
 153. Tuller, H.L. & Nowick, A.S. SMALL POLARON ELECTRON-TRANSPORT IN REDUCED CeO₂ SINGLE-CRYSTALS. *Journal of Physics and Chemistry of Solids* **38**, 859-867 (1977).
 154. Dewit, H.J. & Crevecoeur, C. DEVIATION FROM OHMS LAW IN AS₂SE₃ GLASS. *Physics Letters A* **33**, 25-+ (1970).
 155. Possenriede, E., Krose, H., Varnhorst, T., Scharfschwerdt, R. & Schirmer, O.F. SHALLOW ACCEPTOR AND ELECTRON CONDUCTION STATES IN BaTiO₃. *Ferroelectrics* **151**, 199-204 (1994).
 156. Yang, S., Brant, A.T., Giles, N.C. & Halliburton, L.E. Intrinsic small polarons in rutile TiO₂. *Physical Review B* **87**(2013).

157. Zhang, S.X. et al. Niobium doped TiO₂: Intrinsic transparent metallic anatase versus highly resistive rutile phase. *Journal of Applied Physics* **102**(2007).
158. Freytag, F., Corradi, G. & Imlau, M. Atomic insight to lattice distortions caused by carrier self-trapping in oxide materials. *Scientific Reports* **6**(2016).
159. Cao, Y.J. et al. Scenarios of polaron-involved molecular adsorption on reduced TiO₂(110) surfaces. *Scientific Reports* **7**(2017).
160. Caliskan, D., Sezen, H., Ozbay, E. & Suzer, S. Chemical Visualization of a GaN p-n junction by XPS. *Scientific Reports* **5**(2015).
161. Yin, W.J., Yang, J.H., Kang, J., Yan, Y.F. & Wei, S.H. Halide perovskite materials for solar cells: a theoretical review. *Journal of Materials Chemistry A* **3**, 8926-8942 (2015).
162. Protesescu, L. et al. Nanocrystals of Cesium Lead Halide Perovskites (CsPbX₃, X = Cl, Br, and I): Novel Optoelectronic Materials Showing Bright Emission with Wide Color Gamut. *Nano Letters* **15**, 3692-3696 (2015).
163. Tian, J.J. et al. Inorganic Halide Perovskite Solar Cells: Progress and Challenges. *Advanced Energy Materials*.
164. Wu, L.Z. et al. From Nonluminescent Cs₄PbX₆ (X = Cl, Br, I) Nanocrystals to Highly Luminescent CsPbX₃ Nanocrystals: Water-Triggered Transformation through a CsX-Stripping Mechanism. *Nano Letters* **17**, 5799-5804 (2017).
165. Chouhan, L., Ghimire, S., Subrahmanyam, C., Miyasaka, T. & Biju, V. Synthesis, optoelectronic properties and applications of halide perovskites. *Chemical Society Reviews* **49**, 2869-2885 (2020).
166. Manser, J.S., Christians, J.A. & Kamat, P.V. Intriguing Optoelectronic Properties of Metal Halide Perovskites. *Chemical Reviews* **116**, 12956-13008 (2016).
167. Huang, L.Y. & Lambrecht, W.R.L. Electronic band structure, phonons, and exciton binding energies of halide perovskites CsSnCl₃, CsSnBr₃, and CsSnI₃. *Physical Review B* **88**(2013).

Chapter 2

Title: Interfacial charge transfer for extracting holes from perovskite nanocrystals.

Dual benefits from molecular “wiring”

Authors: Jesse Tamayo¹, Cambria Bennett^{2,5}, Pauline Do^{3,5}, Tori Do^{4,5}, Karen El-Maraghy^{4,5}, Maximillian F. Mayther¹ & Valentine I. Vullev⁶

1. Department of Chemistry, University of California, Riverside, CA 92521, USA. 2.

Department of Biochemistry, University of California, Riverside, CA, USA. 3.

Department of Biology, University of California, Riverside, CA 92507, USA. 4.

Department of Neuroscience, University of California, Riverside, CA 92521, USA. 5.

These authors are undergraduates. 6. Department of Bioengineering, University of

California, Riverside, CA 92507, USA. Email: vullev@ucr.edu

Abstract

The unprecedented rates of developments in perovskite photovoltaics have driven a 6.5-fold increase in power-conversion efficiency since 2009. This growth testifies for the impacts of these materials that remain underrealized. While solvent polarity enhance charge transfer (CT), the instability of these perovskites in polar environments hurdles the realization of their potentials. This article demonstrates the importance of binding a

redox-active moiety to CsPbBr₃ perovskite nanocrystals (NCs) for achieving efficient CT in hydrocarbon media. Tightly binding compounds, such as amines, etch the perovskites. Under controlled concentrations, however, binding an amine derivative of an electron donor to NC surfaces not only provides electronic coupling for efficient CT, but also eliminates sites responsible for undesired exciton deactivation. This dual benefit from “wiring” CT mediators to perovskite surfaces ensures efficient charge extraction in non-polar media. It opens doors to uncharted frontiers for solar energy, photocatalysis and other areas of phonics and electronics.

Author contributions: J.T. spearheaded the study, designed the NC synthesis, performed structural characterization, and carried out the optical-spectroscopy studies and data analysis. C.B., P.D. T.D. and K.E. carried out the synthesis and the purification of the NCs, as well as the NMR studies. M.F.M. performed the electrochemical studies. V.I.V. concaved the supervised the project, carried out some of the analysis, and along with J.T., prepared the manuscript.

Introduction

Metal-halide perovskites, with composition $A^+B^{2+}X_3^-$, have exerted one of the biggest impacts in the development of photovoltaics (PVs).¹ The unique electronic structure of the $[BX_6]^{4-}$ octahedrons ensures not only long exciton lifetimes, but also separate transport pathways for electrons and holes.² The latter feature, along with the small

exciton binding energy has made these perovskites practically the “perfect” materials for photovoltaics.³

In 2009, Miyasaka et al. reported the first perovskite PV devices that manifested encouraging power-conversion efficiencies (η) between 3% and 4%.⁴ Only three years later, the teams of Grätzel and Park demonstrated perovskite PVs with η exceeding 9%.⁵ This burst in progress led to single-junction perovskite PVs with $\eta \approx 24\%$, developed in the Chinese Academy of Sciences, and tandem perovskite-silicon solar cells with $\eta \approx 28\%$, developed by Oxford PV.^{6,7}

While these rates of evolution are unprecedented for a PV class of materials, the importance of the metal-halide perovskites goes beyond their utility for solar cells. In fact, the report from Chondroudis and Mitzi about electroluminescence of perovskites, targeting light-emitting-diode (LED) applications, predates the first PV publication by 10 years.⁸ The attractive optoelectronic properties of metal-halide perovskites drives the increasing interest in their utility as photoredox catalysts.^{9,10}

The ionic bonding in the $A^+B^{2+}X_3^-$ crystalline structures is relatively weak, allowing for a certain level of plasticity of the metal-perovskite lattices. This softness of the ionic structure, along with the “looseness” of the large counterion, A^+ , is key for the beneficial optoelectronic properties of the metal-halide perovskites. As A^+ , methylammonium and formamidinium are charged species with permanent electric dipoles. Conversely, the

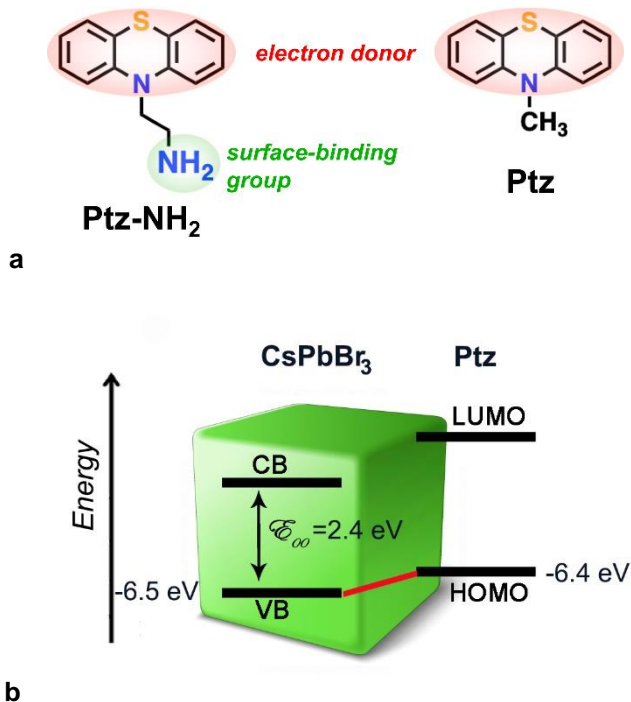
large alkaline cations, such as Cs^+ , are spherically symmetric (with no permanent dipole) but highly polarizable. This propensity of A^+ to induce electronic and orientational polarization¹¹ aids the formation of positive and negative polarons.¹² The polarons keep the holes spatially separated from the electrons, which is crucial for impeding undesired charge recombination.¹²

As important as the lattice softness is for the optoelectronic properties of the metal-halide perovskites, it also is an underlying reason for one of its biggest demises: i.e., the lack of stability and photostability in polar or humid environments.³ Despite the success in the efforts to address this challenge, it still remains an issue.^{2,3,13} All-inorganic metal-halide perovskites, such as CsPbBr_3 , have gained attention in recent years for applications in LEDs,¹⁴ PVs,¹⁵ lasers,¹⁶ and photodetectors¹⁷ due to their strong optical absorptions, narrow line widths, high photoluminescence quantum yields (ϕ_{PL})¹⁸ and increased thermal stability relative to the organic-inorganic perovskite.^{19,20} While they have not matched yet the performance of their hybrid counterparts, PVs of all-inorganic perovskites have gained momentum in recent years, showing an increase in η from about 10% to 19%.¹⁹ Most of the early work on CsPbBr_3 focused on films,²¹⁻²³ and recently research with suspensions of all-inorganic perovskite nanocrystals (NCs) gained traction.^{24,25} The inherent lack of stability of these materials in polar solvents, air and moisture, however, proves especially pronounced for NCs, even with CsPbBr_3 composition.^{20,26}

The limited stability of perovskites in polar media significantly diminishes their utility for photoredox and other charge-transfer (CT) applications. Polar environment inherently stabilizes CT-produced charged species. As important as polar media is for CT processes, selecting large electron donors and acceptors, with reduction potentials corresponding to overestimated CT driving forces, allows for attaining efficient CT in non-polar environments. As an alternative, we have demonstrated that non-polar solvents can enhance the rates of CT in the presence of localized electric fields, originating for example from dipoles.^{27,28} Overall, improved understanding of how to extract holes or electrons from photoexcited perovskites in non-polar media is crucial for the achievement of many of the unrealized promises they offer.

Reliable interfacing, or “wiring,” the perovskite surfaces presents another key challenge for efficient extractions of holes and electrons from them. Aliphatic amines have some of the strongest binding propensity for metal-halide perovskites. Organic coatings of perovskite surfaces, even with amine ligands, are dynamic in nature when immersed in liquid media.²⁶ The ionically bound amines, which convert to ammonium ions after proton exchange, are essential for keeping the material intact. Still, they adsorb and desorb faster than the NMR acquisition timescales.²⁶

Chart 1. *N*-alkylated phenothiazine derivatives selected for electron donors, along with thermodynamic considerations for interfacial CT with CsPbBr₃ Perovskite NCs.



(a) Electron donor with and without aliphatic amine, **Ptz** and **Ptz-NH₂**, respectively. The amine has high propensity for binding to Perovskite surfaces. (b) CB = conduction band and VB = valence band of the NCs; LUMO = lowest unoccupied molecular orbital and HOMO = highest occupied molecular orbital of **Ptz**.

Herein, we focus on interfacial photoinduced hole transfer (PHT) from CsPbBr₃ NCs to an external electron donor in a hydrocarbon solvent medium. An electron-rich organic moiety, *N*-methylated phenothiazine (**Ptz**), serves as an electron donor (Chart 1).

An amine derivative of the electron donor, **Ptz-NH₂**, allows us to examine the role of surface binding for achieving efficient interfacial CT. **Ptz** hardly affects the lifetime of

the NC excitons. At μM concentrations, on the other hand, **Ptz-NH₂** substantially quenches the photoluminescence (PL) of the NCs. Despite the dynamic nature of the surface binding of the amines, their affinity for the NCs ensures the electronic coupling of the donor with the CsPbBr₃ inorganic phase. Increasing the concentrations of **Ptz-NH₂** increases the number of donor moieties per NC and hence, increases the probability for PHT. Such an increase in the amine concentration above 1 mM, however, causes etching of the NCs and a drastic change in their morphology, placing a limit on the feasibly attainable number of **Ptz-NH₂** ligands per NC. Analysis of the results from the time-resolved-spectroscopy studies reveals 700- μs inherent PL lifetimes of the CsPbBr₃ NCs that is drastically shortened by features of the materials itself, which can be assigned to traps in analogy with other semiconductor nanoparticles. The rate constant, k_{PHT} , of hole transfer from a NC to the surface-bound donor is about 10^8 s^{-1} , which is consistent with the electronic coupling pathway through three covalent bonds of the linker (Chart 1a). Most importantly, binding of **Ptz-NH₂** to the NCs eliminates some of the traps responsible for shortening the exciton lifetime, which increases the efficiency of the interfacial CT when it proceeds at such slow rates. While the non-polar media limits the choices of electron donors and acceptors, lowering the polarity of the environment keeps the perovskite structures intact and enhances the ionic binding interactions. Anchoring of amine-derivatized redox species to perovskite surfaces: (1) ensures through-bond electronic coupling for efficient interfacial CT; and (2) eliminates sites responsible for undesirable non-radiative deactivation of the excitons. This dual benefit from using redox-active species with surface-binding groups for efficient extraction of charge

carriers, demonstrates a crucially important paradigm for perusing unexplored optoelectronic properties of metal-halide perovskites.

Results and Discussion

Synthesis of CsPbBr₃ nanocrystals. Adopting previously reported procedures,²⁹ we prepare CsPbBr₃ perovskite nanocrystals (NCs) that assume cubic shapes with edge dimensions of about 11 ± 2 nm (Figure 1a,g). Examining a number of transmission electron microscopy (TEM) images reveals in some of the batches the presence of 1% to 2% particles that are as large as 20 nm. Considering the volume of the particles shows that even in such batches 90% or more of the perovskite material is in the NCs with edge size smaller than about 13 nm (Figure 1g). During the hot-injection synthesis in 1-octadecene (C₁₈H₃₆) solvent, oleylamine (C₁₈H₃₅NH₂) and oleic acid (C₁₇H₃₃CO₂H) coat the formed NCs and maintain their structural integrity and colloidal stability in hydrocarbon solvents. Perovskite NCs are inherently unstable in polar, and even in moderately polar, media.²⁶ While hydrocarbon solvents are essential for preserving the perovskite NCs intact, polar media is paramount for facilitating CT that leads to the formation of charged species. The polarity effects on CT are especially pronounced when small molecular moieties act as electron donors or electron acceptors, i.e., Born, Onsager and high-multipole solvation energies are inversely proportional to the sizes of the solvated species.³⁰

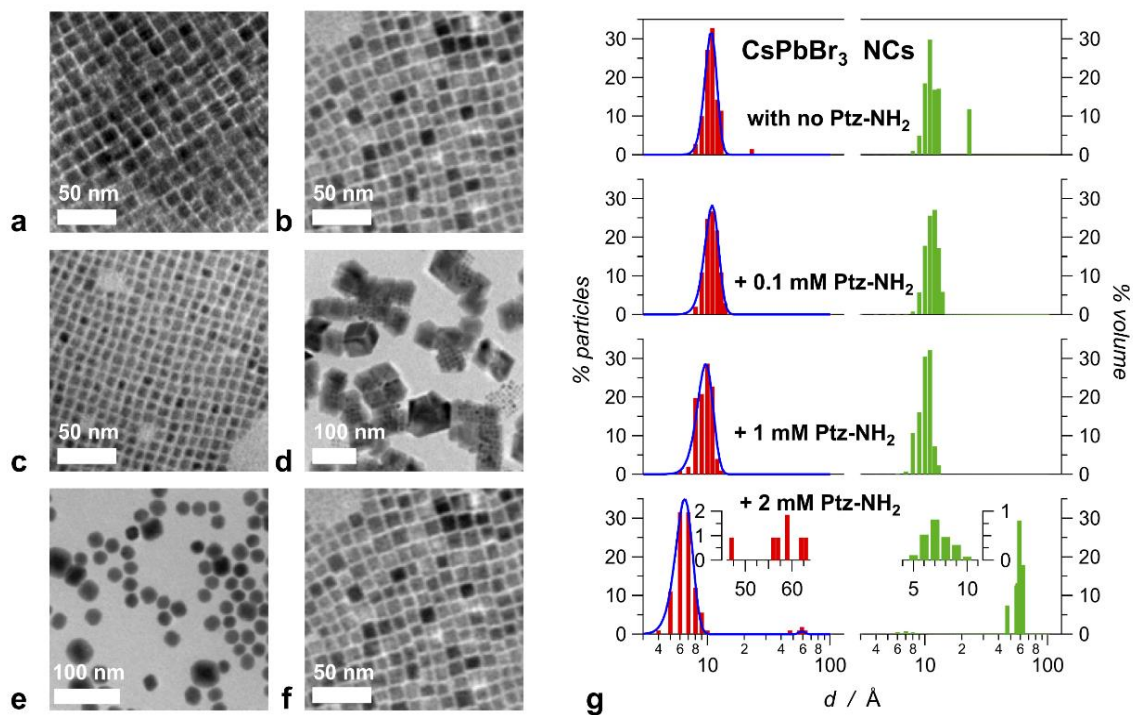


Figure 1 . CsPbBr₃ perovskite nanocrystals in the absence and presence of **Ptz** and **Ptz-NH₂**. (a) TEM images of nanocrystals as synthesized. (b-e) TEM images of nanocrystals incubated with **Ptz-NH₂** in benzene for one hour: (b) 0.1 mM **Ptz-NH₂** in; (c) 1 mM **Ptz-NH₂** in; (d) 2 mM **Ptz-NH₂** in; (e) 5 mM **Ptz-NH₂**. (f) TEM images of nanocrystals incubated with 5 mM **Ptz** in benzene for one hour. (g) Histograms showing the size distribution of the synthesized nanocrystals when incubated with various amounts of **Ptz-NH₂**, represented as a number of particles with edge dimensions, d (1-nm step), and as a volume of inorganic material in nanoparticles with edge dimensions, d (% volume = $d^3 \times$ % particles).

Therefore, we select benzene for a solvent to ensure the NC stability. Benzene, unlike alkanes, provides sufficient solubility for organic conjugates that can serve as electron donors or acceptors. Furthermore, we focus on a relatively large organic conjugate for an electron donor, such as phenothiazine, that comprises three condensed aromatic cycles. In addition to its *N*-methylated derivative, i.e., **Ptz**, we also focus on a conjugate with a free

primary alkyl amine, i.e., **Ptz-NH₂** (Chart 1a). Alkyl amines have a pronounced propensity for binding to perovskite surfaces, which makes **Ptz-NH₂** a good candidate for exploring interfacial CT phenomena involving CsPbBr₃ NCs.

Phenothiazine as hole acceptors and electrochemistry. The electron-rich heterocyclic Ptz oxidizes at 0.78 and 0.98 V vs. SCE when in CH₃CN and CH₂Cl₂, respectively (Figure 2a). The linear relationship between the Born solvation energy of a charged moiety and the inverse of the medium dielectric constant (Figure 2b), allows for extrapolation of the reduction potentials of Ptz^{•+} for other solvents, yielding $E_{\text{Ptz}^{\bullet+}|\text{Ptz}}^{(1/2)} = 1.7 \pm 0.2$ V vs. SCE for benzene, which corresponds to energy $E = -\left(4.68 + F E_{\text{Ptz}^{\bullet+}|\text{Ptz}}^{(1/2)}\right)$

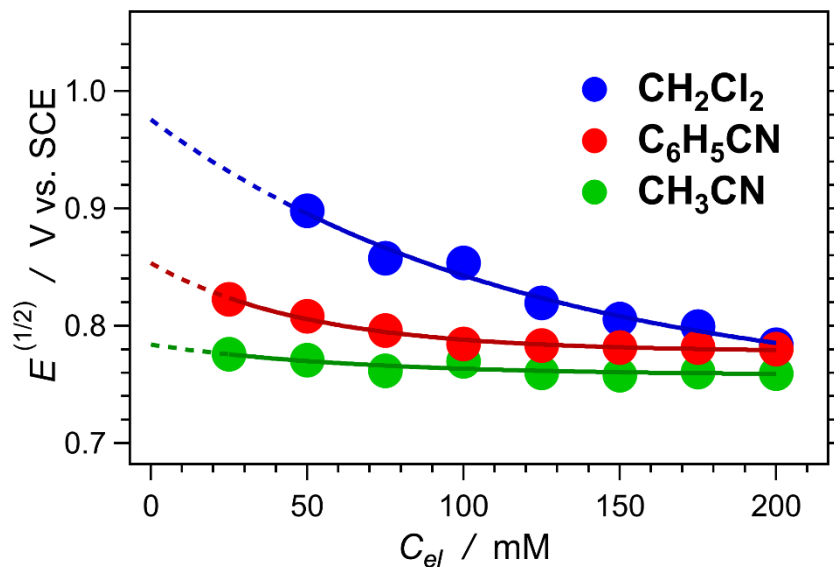


Figure 2 (a) Electrochemical properties of **Ptz** for different solvents. (a) Dependence of reduction potentials of Ptz^{•+}, on the electrolyte concentration, C_{el} . The half-wave reduction potentials, $E_{\text{Ptz}^{\bullet+}|\text{Ptz}}^{(1/2)}$, were determined from cyclic voltammogram, and $N(\text{C}_4\text{H}_9)_4\text{PF}_6$ was used as an electrolyte. Extrapolation to $C_{el} = 0$ allows for estimating the values of $E_{\text{Ptz}^{\bullet+}|\text{Ptz}}^{(1/2)}$ for neat solvents: dichloromethane, benzonitrile and acetonitrile

$= -6.4 \pm 0.2$ eV vs. vacuum.³¹ Concurrently, the reported values for the ionization energy (IE) of CsPbBr₃ films vary widely between about 5.8 and 6.5 eV.³²⁻³⁴ These findings suggest that hole transfer (HT) from photoexcited CsPbBr₃ NCs to Ptz can be exergonic even in hydrocarbon media. It is consistent with reported CT between CsPbBr₃ NCs and this type of an electron donor in alkane solutions.³⁵ Nevertheless, even for the most favorable interpretation of the NC band energy, i.e., IE \approx 6.5 V,³² such photoinduced hole transfer (PHT) operates with a small driving force, $-\Delta G_{\text{PHT}}^{(0)}$. The low solvent polarity, on the other hand, ensures small medium reorganization energy, which favors processes with small driving forces, bringing them close to the activationless region at the tip of the Marcus curve.³⁶

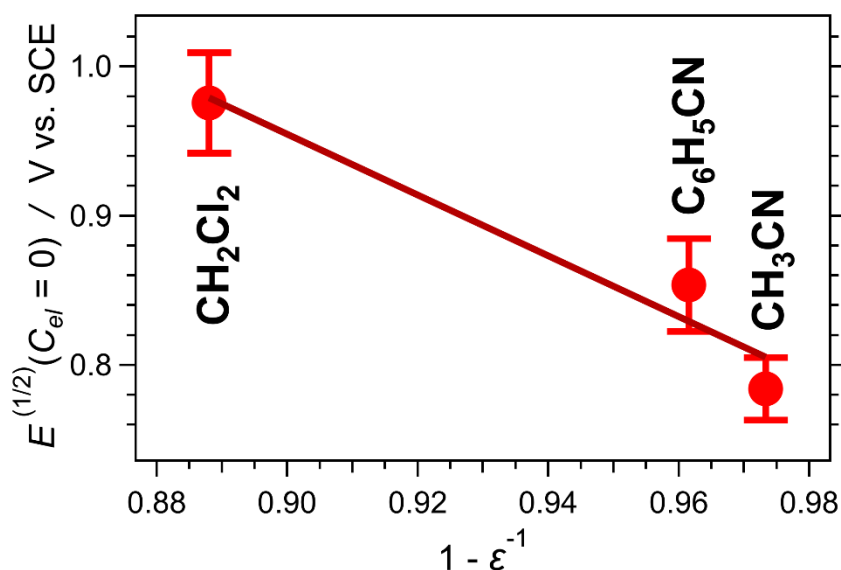


Figure 2b (b) Dependence of the reduction potentials for neat solvents on the Born polarity parameter, $1 - \epsilon^{-1}$; where ϵ is the static relative dielectric constant of the solvent. A linear fit allows for extrapolating the values of $E_{\text{Ptz}^{*+}|\text{Ptz}}^{(1/2)}$ for other solvents, e.g., $E_{\text{Ptz}^{*+}|\text{Ptz}}^{(1/2)}$ for hexane is 1.8 ± 0.2 V vs. SCE, and for benzene and toluene, it is 1.7 ± 0.2 V vs. SCE.

Steady State Optical Spectroscopy. Phenothiazine is a UV absorber. This feature allows for selective photoexcitation of the CsPbBr₃ NCs at wavelengths longer than about 380 nm in the presence of mM amounts of **Ptz** and **Ptz-NH₂** (Figure 3a). The UV/visible absorption and emission spectra of the CsPbBr₃ NCs, suspended in benzene, reveal an optical bandgap of 2.4 eV (Figure 3b), which agrees well with the reported features of such nanomaterials.²⁶ Adding **Ptz** to suspensions of the NCs induces small hypsochromic spectral shifts, along with a minute decrease in the photoluminescence (PL) quantum yield, ϕ_{PL} , of the perovskites (Figure 3). Adding the amine derivative, **Ptz-NH₂**, on the other hand, almost completely quenches the PL of the NCs, while causing a small bathochromic shift (Figure 3). Perturbations in the NC coating of the oleyl ligands, induced by additives to the solvent, can account for small spectral shifts and slight fluctuations of ϕ_{PL} . Such perturbations at the NC surfaces, however, cannot explain the observed drastic decrease in the NC ϕ_{PL} induced by **Ptz-NH₂** (Figure 3c,d). While 100 – 200 μM **Ptz-NH₂** quenches about 90% of the NC PL, **Ptz** at similar concentrations induces only 10% decrease in ϕ_{PL} . This comparison unequivocally indicates that the PL quenching by **Ptz-NH₂** involves a static mechanism. It is consistent with the high affinity for binding to perovskite surfaces that aliphatic amines exhibit.²⁶ Because the primary alkyl amine is the principal difference between **Ptz** and **Ptz-NH₂**, physical binding of **Ptz-NH₂** to the surface of the NCs appears as a necessary condition for the observed PL quenching. The optical-spectroscopy results show that **Ptz** conjugated with a primary alkyl amine invokes alternative pathways for non-radiative deactivation of the perovskite excitons.

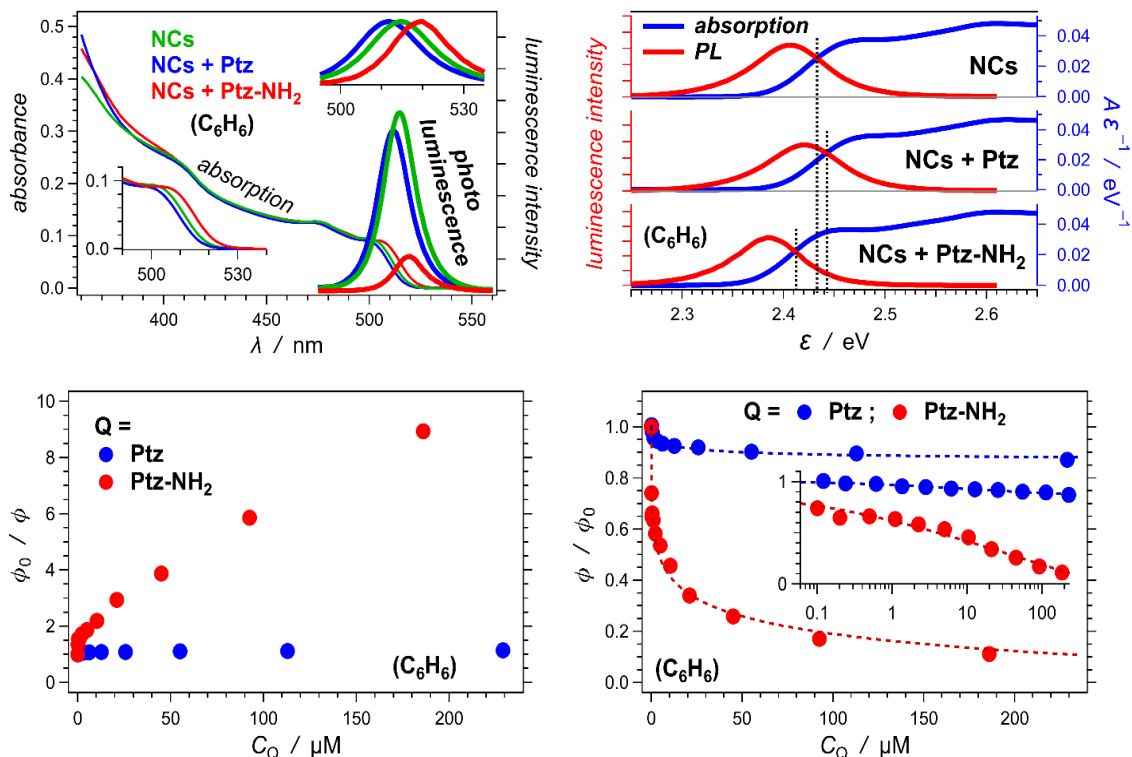


Figure 3 Optical properties of CsPbB₃ NCs in the absence and presence of **Ptz** and **Ptz-NH₂**. (a) Optical absorption and photoluminescence spectra of the NCs by themselves and with 100 μM **Ptz** and **Ptz-NH₂**. For the PL spectra, $\lambda_{\text{ex}} = 400 \text{ nm}$; and the PL spectra are divided by the relative intensity of the absorbed light, i.e., by $(1 - 10^{-A(\lambda_{\text{ex}})})$. To show the spectral shifts, the insets display the bathochromic edges of the absorption spectra and the normalized PL spectra. (b) Normalized absorption and PL spectra plotted against energy. The spectra are corrected for the transfer from wavelength to energy abscissa, [ref] and the crossing between them represents the zero-to-zero energy, ϵ_{00} , i.e., the optical bandgap, as indicated by the dotted vertical lines. (c) Stern-Volmer plot showing the quenching patterns of the NC PL upon addition of **Ptz** and **Ptz-NH₂** as a quencher, Q. (d) The same PL quenching represented as an inverse quantity of the ordinate. The representation of the quenching against a logarithmic abscissa in the inset shows the changes at small quencher concentrations.

Still, a question remains if the observed PL quenching is due: (1) to interfacial phenomena, such as CT or energy transfer with the **Ptz** at the perovskite surfaces, or (2) to changes in the bulk morphology of the NCs. The favorable driving force for PHT, along with propensity of **Ptz** to act as a triplet-energy acceptor,³⁷ makes the former quite a feasible possibility. On the other hand, TEM provides an incomparable means for addressing the latter by examining if the **Ptz** additives induce any changes in the morphology of the inorganic NCs.

Among the interfacial processes, CT is the most likely reason for the observed PL quenching. The optical absorption and emission spectra of **Ptz** and the NCs render resonance energy transfer implausible. Nevertheless, triplet energy transfer (TET) from the NCs to Ptz can present an alternative pathways for the exciton deactivation.³⁸ The energy of ³Ptz*, however, is 2.6 eV,³⁷ which makes TET quite endergonic. Considering the 2.4-eV optical bandgap of the NCs (Figure 3a) makes $\Delta G_{\text{TET}} = 0.2$ eV, which excludes TET as a feasible possibility and makes interfacial PHT the most likely reason for the observed PL quenching by **Ptz-NH₂**.

Transmission electron microscopy and NC morphology and size distribution. TEM images show that upon the addition of up to 1 mM of **Ptz-NH₂** to the perovskite suspension, the NCs retain their morphology (Figure 1b,c,g). As the concentrations of **Ptz-NH₂** exceeds 1 mM, a decrease in the sizes of the majority of the NCs accompanies a persistent appearance of large crystals with sizes exceeding 50 nm (Figure 1d,g). At

moderate **Ptz-NH₂** concentrations of about 2 mM, the number of the large particles is relatively small compared to the total count of NCs, i.e., < 10 % (Figure 1g).

Normalization for the NC volume for such samples, however, reveals that more than 95 % of the perovskite material is in the large particles (Figure 1g). The size of the perovskite particles has a relatively small effect on their absorption and PL wavelengths (unlike other semiconductor NCs).²⁶ The optical absorption cross section of a particle, however, strongly depends on its size. Therefore, even when the number of particles with sizes of 50 nm or larger does not exceed 10 %, their PL signal dominates the emission spectra.

At **Ptz-NH₂** concentrations of 5 mM and larger, the presence of small, about 10-nm, NCs with cubic morphology is undetectable. Such high amine concentration causes drastic changes in morphology, producing round NCs with a broad size-distribution (Figure 1e). This finding is consistent with ligand-assisted etching of the NCs,³⁹ involving dissolution of most of them, while depositing the inorganic material on a few of them and increasing their sizes. The optical spectra of samples with 5 and 10 mM Ptz-NH₂ indicate that the change of the morphology of the CsPbBr₃ NCs into large round particles still conserves their perovskite nature.

Adding **Ptz**, on the other hand, does not induce such drastic changes in the NC morphology (Figure 1f). Nevertheless, considering the adverse effects of the amine additive, we keep the concentration of **Ptz** and **Ptz-NH₂** under 1 mM to preserve the NC

morphology, and allow for ascribing the observed phenomena to interfacial interactions between the electron-rich ligands and the perovskite excitons, rather than to morphology changes in the inorganic phase.

¹H-NMR ligand analysis. While TEM analysis is quite informative about the morphology of the inorganic structures, it is inherently insensitive to phases with low electron density, making it unfeasibly challenging for monitoring the organic coatings on the perovskite surfaces. Conversely, proton NMR spectra prove informative about the composition of the organic components in the suspensions of the CsPbBr₃ NCs. Comparison of the alkene regions of the ¹H NMR spectra, i.e., around 4.5 and 6 ppm, of NC suspensions with the spectra of the comprising ligands, C₁₈H₃₅NH₂ and C₁₇H₃₃CO₂H, and the solvent used for the perovskite synthesis, C₁₈H₃₆, reveals that all these long aliphatic conjugates interact with the NCs, as evident from the downfield shifts (Figure 4a). As previously demonstrated, the NMR signals from the aliphatic protons of the C₁₈H₃₅NH₂ and C₁₇H₃₃CO₂H ligands in CsPbBr₃ NC suspensions are undiscernible.²⁶ The employed synthesis and washing procedures yield samples of NCs with C₁₈H₃₆ that exceeds the total amount of ligands by a factor of four, i.e., ($\chi(\text{C}_{18}\text{H}_{35}\text{NH}_2) + \chi(\text{C}_{17}\text{H}_{33}\text{CO}_2\text{H})$):($\chi(\text{C}_{18}\text{H}_{36})$) \approx 1:4 (Figure 4a-c).

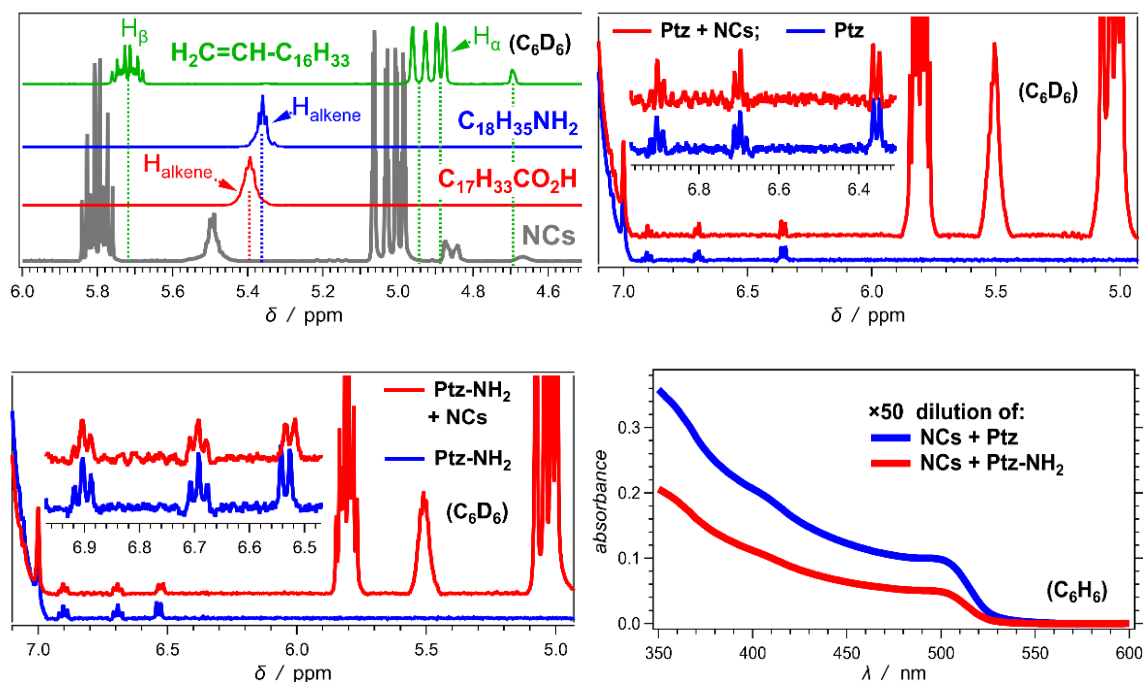


Figure 4 ^1H NMR analysis of suspensions of CsPbBr_3 NCs in deuterated benzene. (a) Comparison between the alkene regions of NMR spectra of a suspension of NCs and of solutions of the comprising components (without NCs): oleylamine, oleic acid and 1-octadecene. The alkene impurity between 4.6 and 4.8 ppm is introduced with the octadecene solvent. The downfield shifts of the protons of all alkenes in the NC samples indicate that all organic compounds bind to the NCs. For these NC samples, the molar fraction of octadecane is about 80% of the total organic compounds. (b) NMR spectra of **Ptz** (0.1 mM) in the presence and absence of NCs. Integration of the signals reveals that the total concentration of $\text{C}_{18}\text{H}_{35}\text{NH}_2$ and $\text{C}_{17}\text{H}_{33}\text{CO}_2\text{H}$ in the sample is about 9 mM, and $\text{C}_{18}\text{H}_{36}$ – about 35 mM. (c) NMR spectra of **Ptz-NH₂** (0.1 mM) in the presence and absence of NCs. (d) Absorption spectra of the samples from (b) and (c) diluted with benzene by a factor of 50. The reported molar extinction coefficient for CsPbBr_3 cubic NCs with this size, $\epsilon_{d=11\text{nm}}(400\text{ nm})$, vary between about 3×10^6 and $3 \times 10^7\text{ M}^{-1}\text{ cm}^{-1}$, [ref] suggesting that the concentration of the NCs in the sample with **Ptz** is between 0.3 and 3 μM , and with **Ptz-NH₂** it is twice smaller.

Previous studies show that it is not common for protons closest to the surface of NC to be observed in NMR while the alkene protons of $\text{C}_{18}\text{H}_{35}\text{NH}_2$ and $\text{C}_{17}\text{H}_{33}\text{CO}_2\text{H}$ moieties, which are close to the amines and the carboxylates anchored to the NC surfaces, are not identifiable as separate species when mixed together in solution-phase NMR spectra.²⁶ It

is consistent with protons closest to the surface to exhibit immobilization-induced broadening of the signals from these protons to an extent where they become undiscernible from the baseline noise. The aliphatic protons of the ligands, on the other hand, are seven and eight methylene apart from the immobilized anchoring groups, ensuring sufficient flexibility and tumbling timescales making them NMR detectable. This feature, furthermore, suggests for relatively loose packing of the aliphatic coatings on the perovskite surfaces, consistent with their dynamic nature: i.e., the rates of amine and carboxylate adsorption and desorption are comparable to the NMR acquisition timescales.²⁶ The alkene signals from the solvent, 1-octadecene, on the other hand, remain sharp even when downfield-shifted by the presence of NCs. This feature suggests that the unsaturated termini of the $C_{18}H_{36}$ moieties are close enough to the inorganic surface to cause deshielding, but far enough to allow them the degrees of conformational freedom resulting in the observed sharp peaks (Figure 4a).

The reported estimates for packing of unsaturated aliphatic ligands on $CsPbBr_3$ surfaces amounts to about 2.3 molecules per nm^2 .²⁶ This surface density is similar to that of somewhat disordered packing of other molecules on inorganic substrates.⁴⁰ When forming self-assembled monolayers with two-dimensional crystalline morphology, tight packing of alkylthiols on noble-metal surfaces amounts to about 0.7 nm^{-2} , i.e., 4×10^{14} molecules per cm^2 .⁴¹ This surface density of 4 molecules per nm^2 represents the maximum possible packing of aliphatic conjugates in surface monolayers. The reported surface density of amines and carboxylates on perovskite surfaces is, therefore, consistent

with the formation of somewhat loose monolayers. The unperturbed shapes of the alkene NMR signals from C₁₈H₃₆, however, is consistent with intercalation of the solvent molecules in the NC coatings, which does not preclude also multilayer formation.

Between 6 and 7 ppm, the ¹H NMR spectra of **Ptz** and **Ptz-NH₂** show the two triplets and one of the doublet signals from their aromatic protons (Figure 4b,c). At such low concentrations of **Ptz** and **Ptz-NH₂**, i.e., ~ 100 μM, the other aromatic doublet overlaps with the tail of the solvent peak, i.e., from C₆HD₅ in the C₆D₆ solvent. Adding NCs to solutions of **Ptz** does not cause any perturbation in its chemical shifts and peak appearance (Figure 4b). Such a lack of NC-induced shifts or broadening of the lines in the aromatic spectral region precludes strong interactions between Ptz and the perovskite particles, which is consistent with the PL-quenching and TEM-imaging results. It suggests for a dynamic PL-quenching mechanism as the slow decrease in ϕ/ϕ_0 with the increase in C_{Ptz} reveals (Figure 3d). Conversely, random collisions between NCs and **Ptz** molecules do not guarantee CT-induced PL quenching interactions. The thick aliphatic coatings on the perovskite surfaces preclude sufficient electronic coupling between the collided **Ptz** moieties and the CsPbBr₃ phase of the NCs. Nevertheless, the tips and the edges of the cubic NCs may suffer from disruptions in the aliphatic layers and provide sites for PL quenching. Small amounts of pinhole defects in the aliphatic coatings, exposing the inorganic phase to the surrounding media, can also provide sites for adsorption and immobilization of the **Ptz** moieties directly on the inorganic surface, causing the observed small but sharp decrease in PL intensity upon the initial addition of

the first 10 μM **Ptz** (Figure 3d). Considering that the concentration of NCs in these NMR samples hardly exceeds a few μM (Figure 4b,d), suggests that the amounts of **Ptz** moieties causing the initial 10% decrease in the NC PL is considerably below the NMR detection limits. Furthermore, complete immobilization of the Ptz moieties would cause peak broadening, making them undetectable in solution-phase NMR spectra.

As an alternative, we cannot exclude effects that do not involve collisional quenching and CT. For example, **Ptz**-induced changes in the activity of the desorbed oleyl conjugates can alter their propensity for binding to the CsPbBr_3 surfaces. Nevertheless, noticeable changes in the activity of the ligands with mM concentrations upon the initial additions of a few μM **Ptz** is highly unlikely. Therefore, interactions of the quencher with pinholes defects in the NC coatings remains the most plausible reason for the initial **Ptz**-induced drop in the PL of the NCs (Figure 3d).

The non-interacting **Ptz** moieties with known concentration allow for quantification of the amounts of organic conjugates in the NMR samples (Figure 4b). Integration of the NMR signals reveals that in the **Ptz** sample with NCs, the amount of oleyl ligands is about 9 mM (Figure 4b). Considering surface packing of 2 – 2.3 ligands per nm^2 , suggests for 1,400 to 1,700 ligands per a nanocrystal. Hence, 9 mM ligands suggests for 5 – 6 μM NCs in the suspension. Concurrently, the absorption spectra of these samples, along with the reported molar extinction coefficients for CsPbBr_3 NCs with this size, indicate that the concentration of NCs in this NMR sample does not exceed 3 μM (Figure

4d). Adding the fact that the NMR-estimated $C_{18}H_{36}$ amount is about 35 mM, which is also involved in the perovskite coatings, even further increases this discrepancy between the NC concentrations estimated with NMR and optical methods (Figure 4b,d). The dynamic nature of the perovskite coatings, indeed, suggests that not all ligands and solvent molecules are bound to the NCs. Adsorption-desorption rates faster than the NMR acquisition times can readily yield the observed average downfield-shifted signals. Nevertheless, the large excess of solvent molecules in comparison with what aliphatic monolayers on the NCs can accommodate renders multilayer formation a feasible possibility.

Adding $CsPbBr_3$ NCs to solutions of **Ptz-NH₂** causes a slight broadening of the phenothiazine aromatic peaks and a small upfield shift of the 6.53-ppm signal from the protons at positions 4 and 5, i.e., closest to the nitrogen, in the Ptz rings (Figure 4c). Adsorption of organic moieties on other types of semiconductor particles, such as chalcogenide quantum dots leads to split in their peaks, showing separate signals from the bound and unbound molecules.⁴² Our findings, however, do not show such peak splitting, which is consistent with the dynamic nature of perovskite coatings.²⁶ As discussed for $C_{18}H_{36}$, the sharp alkene NMR signals suggest for rates of adsorption and desorption that are much faster than the NMR acquisition times. The broadening of the **Ptz-NH₂** aromatic signals, on the other hand, is consistent with association and dissociation rates that are comparable with the NMR timescales. For a **Ptz-NH₂** molecule to bind to the $CsPbBr_3$ surfaces of the NCs, it must diffuse through the aliphatic coating. In addition, a proton exchange, leading to **Ptz-NH₃⁺**, is also essential for ligand replacement and

binding to such perovskite surfaces.²⁶ The NMR-detectable NC-induced perturbations of the phenothiazine aromatic peaks indicates that a noticeable fraction of the **Ptz-NH₂** molecules interacts relatively strongly with the CsPbBr₃ NCs. It deviates from what the NMR spectra of **Ptz** with NCs show. Considering the estimated 100- to 1,000-fold excess of the **Ptz-NH₂** concentration in comparison with the concentration of NCs, suggests for a substantial number of **Ptz-NH₂** molecules bound to a single NC, i.e., either adsorbed to the CsPbBr₃ surfaces or absorbed in the alkene coating layers.

Time resolved optical spectroscopy. Time-resolved optical spectroscopy provides a means for examining the exciton dynamics of the NCs and the kinetics reflecting the drastic PL quenching upon addition of μM amounts of **Ptz-NH₂**. The transient-absorption (TA) spectra of the NC suspensions with and without **Ptz** and **Ptz-NH₂** are quite similar in the sub-nanosecond time domain, showing features typical for perovskite materials (Figure 5a,b). The sub-picosecond TA dynamics is consistent with cooling of the hot excitons formed by the 400-nm pump (Figure 5a). The relaxation of the TA band at 520 nm and of the $-\Delta A$ shoulder at about 490 nm enhances the principal 508-nm bleach band with time constants, τ , ranging between 420 fs and 560 fs for the NCs in the absence and presence of **Ptz** and **Ptz-NH₂**, as expected for these nanomaterials.⁴³

The $\Delta A(t)$ trace of the main bleach band at around 508 nm, reveals a 100-picosecond initial deactivation, followed by slow recovery that extends in the nanosecond time domain (Figure 5c). While the NCs with **Ptz** show the largest amplitude drop in the early

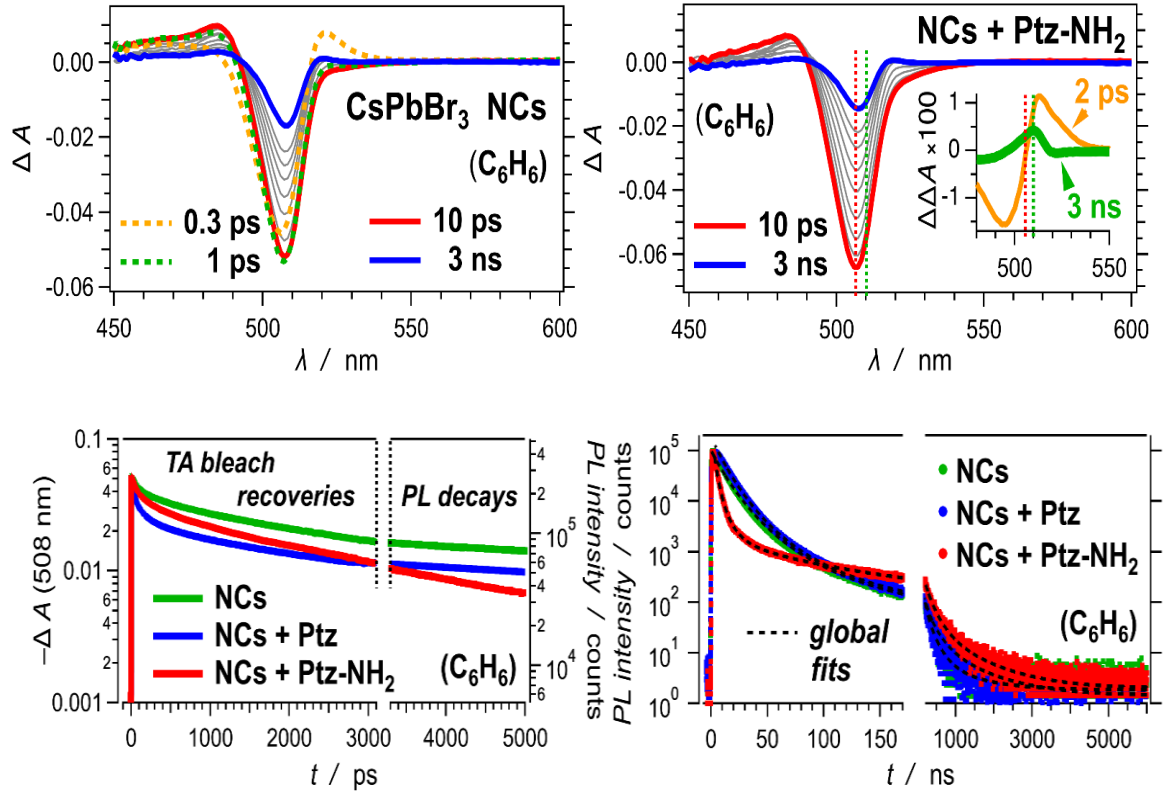


Figure 5 Time-resolved-spectroscopy analysis of CsPbBr₃ NCs, suspended in benzene, by themselves and in the presence of **Ptz** and **Ptz-NH₂**. (a) Transient-absorption (TA) spectra of the NCs by themselves. (b) TA spectra of NCs in the presence of 100 μ M **Ptz-NH₂**. The inset shows the difference between ΔA of NCs in the presence and absence of **Ptz-NH₂** at different times, i.e., $\Delta\Delta A(t) = \Delta A_N(\text{NCs}+\text{Ptz-NH}_2, t) - \Delta A_N(\text{NCs}, t)$, where the spectra are normalized, ΔA_N , for the lowest value of the principal bleach band, i.e., $\min(\Delta A(\lambda, t))$, considering that $(\min(\Delta A(\text{NCs}, \lambda, t)) / \min(\Delta A(\text{NCs}+\text{Ptz-NH}_2, \lambda, t)) \lesssim 0.1$. (c) TA decays following the bleach recovery at 508 nm for the NCs by themselves and in the presence of **Ptz** and **Ptz-NH₂**; showing also the photoluminescence (PL) traces beyond the 3-ns TA dynamic range. (a-c) For the TA measurement, $\lambda_{\text{ex}} = 400$ nm, 50 fs pulses with energy density 50 μ J cm⁻². (d) PL decays of NCs in the absence and presence of Ptz and Ptz-NH₂, recorded at 510 nm using time-correlated single-photon counting (TCSPC), $\lambda_{\text{ex}} = 406$ nm, half-height pulse width = 0.2 ns.

timescales, it's the rate of its slow bleach recovery that is similar to that of the NCs by themselves. The low energy density of the pump minimizes the formation of biexcitons

and trions.⁴³ Even at low fluence, however, charge trapping can result in TA features with lifetimes of hundreds of picoseconds.²⁴

Global-fit analysis shows additional relaxation patterns that extends in the picosecond time domain (Figure 5c,d). In all cases, a common feature emerges: i.e., nanosecond concurrent decrease of the bleach at 508 nm and the TA band at 485 nm (Figure 5c,d), which is consistent with exciton assignment.

A subtle TA feature that discerns the NCs with **Ptz** additives from the NCs without becomes noticeable at nanosecond times. At 3 ns in the 500-515-nm region, the TA spectra of the NCs with **Ptz** and **Ptz-NH₂** show slightly less negative ΔA than those of the NCs by themselves (Figure 5a,b). This relatively small difference is only about 10% of the initial amplitude of the bleach band, and subtracting the spectra for the NCs from those for the NCs with **Ptz** and **Ptz-NH₂** results in a $\Delta\Delta A$ band with a maximum at about 510 nm (Figure 5b – inset), which is a known feature for the TA of the oxidized *N*-methylphenothiazine, $\text{Ptz}^{\bullet+}$.³⁷ Despite this indication for interfacial PHT, the relatively small amplitude of this $\Delta\Delta A$ feature and the lack of significant differences in the sub-nanosecond TA dynamics, warrant a search for the underlying reasons for the Ptz-NH₂-induced PL quenching in nanosecond and microsecond time domains. Furthermore, the maximum of the $\Delta\Delta A$ band is only a couple of nanometers to the red of the minimum of the bleach band (Figure 5b). This spectral overlap renders caution when ascribing this $\Delta\Delta A$ feature to $\text{Ptz}^{\bullet+}$.

Time-correlated single-photon counting (TCSPC) analysis allows one to follow the deactivation of the emissive excitons beyond the dynamic range of the pump-probe TA spectroscopy to the microsecond time domain (Figure 5c,d). TCSPC reveals that 99 % of the PL amplitude decays within 100 ns for the CsPbBr₃ NCs with and without the phenothiazine additives (Figure 5d). Nevertheless, it takes extra 5 μ s of slow decay to bring the NC PL down to the baseline (Figure 5d). Because of the small amplitude of this microsecond PL decay, it may wrongly appear insignificant and ignorable. It is important to emphasize, however, that ϕ_{PL} depends not only on the relative amplitudes but also on the lifetimes of the light-emitting species.^{44,45} Therefore, emission-decay components with small amplitudes and long lifetimes can prove more deterministic for the intensity of steady-state PL than components with large amplitudes and short lifetimes.

Global fit analysis via poisson distribution. The PL of the CsPbBr₃ NCs and the NCs with Ptz decay in a multiexponential manner within the first 100 ns (Figure 5d), which is consistent with expected heterogeneity for the excited-state dynamics of semiconducting nanomaterials. The PL intensity of the NCs with Ptz-NH₂, however, decreases relatively fast in a multiexponential manner within the first 50 ns, followed by a monoexponential decay extending to the microsecond time domain (Figure 5d). This exciton deactivation pattern is representative of samples of identical luminophores, each of which has different number of quenchers attached to it. A model, initially developed for micelle-mediated emission quenching⁴⁶ and recently successfully applied to quantum-dot systems,⁴⁷ assuming a Poisson distribution of each of several quenchers over the NCs in a

sample, presents an excellent approach for analyzing the observed decays of the PL intensity, I_{PL} , for the CsPbBr₃ NCs in the presence and absence of phenothiazine additives:

$$I_{\text{PL}}(t) = I_{\text{PL}}(0) \exp \left(- \frac{t}{\tau_0} - \sum_{i=1}^n \langle N_i \rangle \left(1 - \exp \left(- \frac{t}{\tau_i^{(q)}} \right) \right) \right) \quad (1)$$

where $I_{\text{PL}}(0)$ is the initial amplitude of the PL intensity; τ_0 is the lifetime of the excitons in the absence of any quenchers; n is the number of types of quenchers; $\langle N_i \rangle$ is the average number of a type i quencher per a particle; and $\tau_i^{(q)}$ is the lifetime of the exciton in a particle with a single quencher i .

Keeping the different lifetimes, τ_0 and $\tau_i^{(q)}$, identical among the three samples, while permitting the corresponding $\langle N_i \rangle$ to vary, allows us to fit simultaneously the PL-decay traces of the NCs, the NCs with **Ptz** and the NCs with **Ptz-NH₂** (eq. 1). This global-fit analysis yields an inherent PL lifetime, τ_0 , of the CsPbBr₃ NCs that extends to hundreds of nanoseconds (Table1). Such long lifetimes of the excitons illustrate an immensely attractive feature of perovskite materials and are consistent with PL lingering in the microsecond time domain (Figure 5d). Quenching phenomena resulting from alternative deactivation pathways, however, dominate the exciton dynamics. In the nanosecond time

domain, the shortened lifetimes, $\tau_i^{(q)}$, range from 2 ns to about 500 ns (Table 1). The quencher populations, $\langle N_i \rangle$, for the NCs and the NCs with **Ptz** are quite similar with those yielding $\tau_i^{(q)}$ of about 60 and 500 ps dominating (Table 1). It is consistent with the minimal ϕ_{PL} drop when adding **Ptz** to CsPbBr₃ NCs (Figure 3c,d). When we add **Ptz-NH₂** to the NC suspension, on the other hand, a new quenching feature, with $\tau_i^{(q)} = 10$ ns, emerges (Table 1).

Previous work with nanoparticles of other semiconductor materials ascribes such PL quenchers to exciton traps.^{48,49} The phenothiazine additives have a relatively small effect on the number of traps housing long-lived excitons, with $\tau_5^{(q)} = 510$ ns. Addition of **Ptz** drops $\langle N_5 \rangle$ by about 25%, and of **Ptz-NH₂** – by 40% (Table 1). Conversely, **Ptz** does not strongly affect the number of traps for $\tau_4^{(q)} = 60$ ns, while **Ptz-NH₂** decreases $\langle N_4 \rangle$ by a factor of four (Table 1). The free aliphatic amine is the only difference between **Ptz** and **Ptz-NH₂**. Hence, the presence of the amine that can bind to the CsPbBr₃ surfaces is the only apparent reason for the decrease of $\langle N_4 \rangle$, which allows for ascribing the quenchers with $\tau_5^{(q)} = 60$ ns to surface traps, eliminable by R-NH₃⁺ binding. This finding is consistent with reported increases in the ϕ_{PL} of perovskite NCs when saturating their coatings with amines.²⁶ In contrast, the small effects on $\langle N_5 \rangle$ indicate that the quenchers yielding $\tau_5^{(q)} = 510$ ns are ascribable to traps that are away from the NC surfaces and are most plausibly only indirectly affected by changes in the NC organic coatings.

The quenchers resulting in some of the shortest exciton lifetimes, e.g., $\tau_2^{(q)} = 10$ ns, are significant only for the PL of the NCs in the presence of **Ptz-NH₂**, with $\langle N_2 \rangle$ of about 4

per particle (Table 1). This particular quencher is responsible for the >90% PL decrease within 20 ns after photoexcitation (Figure 5d). Because amines enhance ϕ_{PL} , most likely by eliminating surface traps, the electron-rich aromatic moiety of **Ptz-NH₂** is the apparent reason for the observed quenching.

Table 1. Results from the global-fit analysis of the PL decays and the TA bleach recovery at 508 nm for CsPbBr₃ NCs with and without **Ptz** and **Ptz-NH₂**.^a

parameter	NCs	NCs + Ptz	NCs + Ptz-NH ₂
τ_0 / ns	670 ± 40	670 ± 40	670 ± 40
$\tau_1^{(q)}$ / ns	2.0 ± 1.2	2.0 ± 1.2	2.0 ± 1.2
$\tau_2^{(q)}$ / ns	10 ± 1	10 ± 1	10 ± 1
$\tau_3^{(q)}$ / ns	23 ± 3	23 ± 3	23 ± 3
$\tau_4^{(q)}$ / ns	61 ± 4	61 ± 4	61 ± 4
$\tau_5^{(q)}$ / ns	510 ± 60	510 ± 60	510 ± 60
$\langle N_1 \rangle$	0.72 ± 0.30	0.26 ± 0.12	0.00 ± 0.26
$\langle N_2 \rangle$	0.00 ± 0.02	0.01 ± 0.30	4.1 ± 0.2
$\langle N_3 \rangle$	0.64 ± 0.07	0.01 ± 0.70	0.04 ± 0.05
$\langle N_4 \rangle$	5.1 ± 0.5	5.9 ± 0.3	1.4 ± 0.2
$\langle N_5 \rangle$	3.9 ± 0.1	2.9 ± 0.3	2.2 ± 0.1

The quenchers resulting in some of the shortest exciton lifetimes, e.g., $\tau_2^{(q)} = 10$ ns, are significant only for the PL of the NCs in the presence of **Ptz-NH₂**, with $\langle N_2 \rangle$ of about 4 per particle (Table 1). This particular quencher is responsible for the >90% PL decrease within 20 ns after photoexcitation (Figure 5d). Because amines enhance ϕ_{PL} , most likely

by eliminating surface traps, the electron-rich aromatic moiety of **Ptz-NH₂** is the apparent reason for the observed quenching. Binding of the amine to the inorganic surface provides electronic coupling between the CsPbBr₃ phase and the phenothiazine moiety through three saturated covalent bonds. According to the pathway model,⁵⁰ each covalent bond decreases CT rates by about a factor of three. Three covalent bond, therefore, cause about 20-fold drop in the CT rate constants, i.e., $k_{CT}^{(3 \text{ bonds})} = ((0.6)^2)^3 k_{CT}^{(0 \text{ bonds})}$.^{50,51} Ascribing $(\tau_2^{(q)})^{-1} = 1 \times 10^8 \text{ s}^{-1}$ to k_{CT} for diabatic PHT over three covalent bonds from CsPbBr₃ to surface-linked **Ptz-NH₂** moieties, suggests for $k_{CT}^{(0 \text{ bonds})}$ of about $2 \times 10^9 \text{ s}^{-1}$ for CT between the NCs and **Ptz** adsorbed directly on the inorganic surface. Time-resolved spectroscopy, however, does not reveal detectable new component with lifetime of about 500 ps upon addition of **Ptz** to NCs. While this finding (or the lack of finding) can originate from the assumptions in this train of thought about the CT kinetics. The small electronic coupling between an electron donor and an oxidizing inorganic substrate validates the diabatic treatment of hole tunneling through three covalent bonds. When the **Ptz** donor is adsorbed on the CsPbBr₃ surface, the increased electronic coupling renders adiabatic regime of the CT kinetics. That is, an increase in the CT rates results from the increase not only in the donor-surface electronic coupling, but also in the Franck-Condon contribution to the kinetics, i.e., lowering the transition state considerably below where the potential-energy surfaces of the initial and final states cross. This feature of directly adsorbed **Ptz** moieties on the NC surfaces can push k_{CT}^{-1} to the 100-ps time domain, competing with other exciton-deactivation processes that occur even in the absence of **Ptz** and **Ptz-NH₂** (Figure 5c). That is, an increase in the amplitude of the 100-ps

components of the TA bleach recovery, which is induced by adding of **Ptz** and **Ptz-NH₂**, warrants consideration of CT between the photoexcited NCs and phenothiazine rings directly adsorbed on the inorganic surfaces. Nevertheless, even though $k_{CT}^{(3 \text{ bonds})}$ appears two-orders-of-magnitude smaller than k_{CT} for direct donor-surface contact, this k_{CT} of $1 \times 10^8 \text{ s}^{-1}$ describes a CT process that is principally responsible for the exciton deactivation in the presence of phenothiazine derivatives. It demonstrates the utmost importance of the binding propensity of redox-active species to inorganic surfaces for extracting charges from excitons in such substrates. For halide perovskites, furthermore, even weak electronic coupling with the donor is utterly substantial, especially when the surface bonding eliminates undesired exciton traps.

Considering that an average of only four amine-derivatized electron-donor quenchers per a NC, i.e., $\langle N_2 \rangle$ (Table 1), can induce the observed PL quenching reflects the minute effects that addition of NCs induces on the ^1H NMR spectrum of **Ptz-NH₂** (Figure 4c). The estimated 0.15 and 1.5 μM amounts of NC in the NMR samples suggests that the concentration of CT-active **Ptz-NH₂**, bound to the CsPbBr₃ surfaces of the NCs, is about 0.6 – 6 μM . While the signal-to-noise ratios in the ^1H NMR spectra of 100 μM **Ptz-NH₂** is challengingly small, effects of 0.6% to 6% on the line shapes and positions should be under the detection limits of the technique. Therefore, the observed effects of NCs on the phenothiazine NMR spectrum most likely originate predominantly from **Ptz-NH₂** diffusing through the alkene layers to and from the inorganic surfaces. At each point of time, only a small portion of these **Ptz-NH₂** moieties are directly bound to the CsPbBr₃

phase and experience the electronic coupling with it resulting in the observed CT-induced PL quenching. This structure-function relationship reveals an efficient extraction of charges from photoexcited perovskite nanomaterials by organic moieties in non-polar media in the context of the known adsorption-desorption dynamics of the surface ligands.

Conclusions

Halide perovskite materials with chemical composition $A^+B^{2+}X_3^-$ have shown amazing promises for solar-energy harvesting and conversion. Their inherent susceptibility to surface etching and degradation in polar media appears to halt the enthusiasm for their implementation in commercializable developments. We should reiterate that strongly interacting moieties, such as amines, in hydrocarbon media can also cause the surface degradation. These challenges warrant deeper understanding of the structural and charge-transfer dynamics at perovskite surfaces. Considering the polarity effects on electrochemical potentials points to organic conjugates that are sufficiently electron rich to extract holes from photoexcited perovskites in non-polar media. The amine-mediated binding that can link such electron donors with the inorganic surfaces provides two important benefits: (1) ensures electronic-coupling pathways for sufficiently efficient CT; and (2) eliminates surface traps that shorten the exciton lifetime. The latter removal of undesired pathways of exciton deactivation ensures that interfacial CT can dominate the photoinduced dynamics. That is, even with relatively slow rates of about 10^8 s^{-1} , which is expected for electronic-coupling pathways through three covalent bonds, PHT leads to

exciton dissociation that is a principal outcome when the inherent exciton lifetimes extend to hundreds of nanoseconds. These findings demonstrate paradigms where the pursuit of fast charge injection and polar media is not essential for attaining high photoinduced CT efficiencies, which is of key importance for further broadening of the impacts that perovskite materials have on photonics and on solar-energy science and engineering.

Methods

Cyclic voltammetry was performed and analyzed by taking the redox potentials of Ptz in various solvents with differing dielectric constants to record the redox potential as a function of solvent polarity. Then by reducing the electrolyte concentration from 200 μM to 50 μM we extrapolate to $[0]_{\text{electrolyte}}$ in the same solvents. The redox potential for the solvents at $[0]_{\text{electrolyte}}$ is then plotted versus the final term in the Born equation to realize the redox potential of Ptz in any solvent as a function of solvent polarity.

Steady state optical measurements were performed by titrating Ptz molecules from zero to 200 μM and recorded the absorbance and photoluminescence in ten sequential aliquots.

References.

1. A decade of perovskite photovoltaics. *Nat. Energ.* **4**, 1-1 (2019).
2. Chouhan, L., Ghimire, S., Subrahmanyam, C., Miyasaka, T. & Biju, V. Synthesis, optoelectronic properties and applications of halide perovskites. *Chem. Soc. Rev.* **49**, 2869-2885 (2020).
3. Saliba, M., Correa-Baena, J.P., Gratzel, M., Hagfeldt, A. & Abate, A. Perovskite Solar Cells: From the Atomic Level to Film Quality and Device Performance. *Angew. Chem., Int. Ed.* **57**, 2554-2569 (2018).
4. Kojima, A., Teshima, K., Shirai, Y. & Miyasaka, T. Organometal Halide Perovskites as Visible-Light Sensitizers for Photovoltaic Cells. *J. Am. Chem. Soc.* **131**, 6050-+ (2009).
5. Kim, H.S. et al. Lead Iodide Perovskite Sensitized All-Solid-State Submicron Thin Film Mesoscopic Solar Cell with Efficiency Exceeding 9%. *Sci. Rep.* **2**(2012).
6. NREL. Best Research-Cell Efficiency Chart. (NREL, U.S.A, 2020).
7. Kosmatos, K.O. et al. Methylammonium Chloride: A Key Additive for Highly Efficient, Stable, and Up-Scalable Perovskite Solar Cells. *Energ. Environ. Mater.* **2**, 79-92 (2019).
8. Chondroudis, K. & Mitzi, D.B. Electroluminescence from an organic-inorganic perovskite incorporating a quaterthiophene dye within lead halide perovskite layers. *Chem. Mater.* **11**, 3028-3030 (1999).
9. Rosa-Pardo, I. et al. The synergy between the CsPbBr₃ nanoparticle surface and the organic ligand becomes manifest in a demanding carbon-carbon coupling reaction. *Chem. Commun.* **56**, 5026-5029 (2020).
10. Wang, K. et al. Ultrafast Reaction Mechanisms in Perovskite Based Photocatalytic C-C Coupling. *ACS Energy Lett.* **5**, 566-571 (2020).
11. Upadhyayula, S. et al. Permanent Electric Dipole Moments of Carboxyamides in Condensed Media: What Are the Limitations of Theory and Experiment? *J. Phys. Chem. B* **115**, 9473-9490 (2011).
12. Meggiolaro, D., Ambrosio, F., Mosconi, E., Mahata, A. & De Angelis, F. Polarons in Metal Halide Perovskites. *Adv. Energy Mater.* **10**(2020).

13. Huang, H.W., Pradhan, B., Hofkens, J., Roeffaers, M.B.J. & Steele, J.A. Solar-Driven Metal Halide Perovskite Photocatalysis: Design, Stability, and Performance. *ACS Energy Lett.* **5**, 1107-1123 (2020).
14. Li, G.R. et al. Highly Efficient Perovskite Nanocrystal Light-Emitting Diodes Enabled by a Universal Crosslinking Method. *Adv. Mater.* **28**, 3528-+ (2016).
15. Swarnkar, A. et al. Quantum dot-induced phase stabilization of alpha-CsPbI₃ perovskite for high-efficiency photovoltaics. *Science* **354**, 92-95 (2016).
16. Wang, Y. et al. Nonlinear Absorption and Low-Threshold Multiphoton Pumped Stimulated Emission from All-Inorganic Perovskite Nanocrystals. *Nano Lett.* **16**, 448-453 (2016).
17. Ramasamy, P. et al. All-inorganic cesium lead halide perovskite nanocrystals for photodetector applications. *Chem. Commun.* **52**, 2067-2070 (2016).
18. Zhang, Q. & Yin, Y.D. All-Inorganic Metal Halide Perovskite Nanocrystals: Opportunities and Challenges. *ACS Cent. Sci.* **4**, 668-679 (2018).
19. Tian, J.J. et al. Inorganic Halide Perovskite Solar Cells: Progress and Challenges. *Adv. Energy Mater.*
20. Kulbak, M. et al. Cesium Enhances Long-Term Stability of Lead Bromide Perovskite-Based Solar Cells. *J. Phys. Chem. Lett.* **7**, 167-172 (2016).
21. Berhe, T.A. et al. Organometal halide perovskite solar cells: degradation and stability. *Energ. Environ. Mater.* **9**, 323-356 (2016).
22. Kovalenko, M.V., Protesescu, L. & Bodnarchuk, M.I. Properties and potential optoelectronic applications of lead halide perovskite nanocrystals. *Science* **358**, 745-750 (2017).
23. Yin, W.J., Yang, J.H., Kang, J., Yan, Y.F. & Wei, S.H. Halide perovskite materials for solar cells: a theoretical review. *J. Mater. Chem. A* **3**, 8926-8942 (2015).
24. Mondal, N., De, A., Das, S., Paul, S. & Samanta, A. Ultrafast carrier dynamics of metal halide perovskite nanocrystals and perovskite-composites. *Nanoscale* **11**, 9796-9818 (2019).
25. Seth, S., Ahmed, T., De, A. & Samanta, A. Tackling the Defects, Stability, and Photoluminescence of CsPbX₃ Perovskite Nanocrystals. *ACS Energy Lett.* **4**, 1610-1618 (2019).

26. De Roo, J. et al. Highly Dynamic Ligand Binding and Light Absorption Coefficient of Cesium Lead Bromide Perovskite Nanocrystals. *Acs Nano* **10**, 2071-2081 (2016).
27. Bao, D.D. et al. Dipole-Mediated Rectification of Intramolecular Photoinduced Charge Separation and Charge Recombination. *J. Am. Chem. Soc.* **136**, 12966-12973 (2014).
28. Krzeszewski, M. et al. Dipole Effects on Electron Transfer are Enormous. *Angew. Chem., Int. Ed.* **57**, 12365-12369 (2018).
29. Protesescu, L. et al. Nanocrystals of Cesium Lead Halide Perovskites (CsPbX₃, X = Cl, Br, and I): Novel Optoelectronic Materials Showing Bright Emission with Wide Color Gamut. *Nano Lett.* **15**, 3692-3696 (2015).
30. Schreckenbach, G. Differential Solvation. *Chem.-Eur. J.* **23**, 3797-3803 (2017).
31. Sahai, N. & Sverjensky, D.A. Solvation and electrostatic model for specific electrolyte adsorption. *Geochim. Cosmochim. Acta* **61**, 2827-2848 (1997).
32. Tao, S.X. et al. Absolute energy level positions in tin-and lead-based halide perovskites. *Nature Commun.* **10**(2019).
33. Endres, J. et al. Valence and Conduction Band Densities of States of Metal Halide Perovskites: A Combined Experimental-Theoretical Study. *J. Phys. Chem. Lett.* **7**, 2722-2729 (2016).
34. Endres, J. et al. Electronic structure of the CsPbBr₃/polytriarylamine (PTAA) system. *J. Appl. Phys.* **121**(2017).
35. Wu, K.F. et al. Ultrafast Interfacial Electron and Hole Transfer from CsPbBr₃ Perovskite Quantum Dots. *J. Am. Chem. Soc.* **137**, 12792-12795 (2015).
36. Matyushov, D. Electron transfer in nonpolar media. *PCCP* **22**, 10653 (2020).
37. Jockusch, S. & Yagci, Y. The active role of excited states of phenothiazines in photoinduced metal free atom transfer radical polymerization: singlet or triplet excited states? *Polym. Chem.* **7**, 6039-6043 (2016).
38. Mase, K., Okumura, K., Yanai, N. & Kimizuka, N. Triplet sensitization by perovskite nanocrystals for photon upconversion. *Chem. Commun.* **53**, 8261-8264 (2017).
39. Koscher, B.A., Nett, Z. & Alivisatos, A.P. The Underlying Chemical Mechanism of Selective Chemical Etching in CsPbBr₃ Nanocrystals for Reliably Accessing Near-Unity Emitters. *Acs Nano* **13**, 11825-11833 (2019).

40. Upadhyayula, S. et al. Coatings of Polyethylene Glycol for Suppressing Adhesion between Solid Microspheres and Flat Surfaces. *Langmuir* **28**, 5059-5069 (2012).
41. Love, J.C., Estroff, L.A., Kriebel, J.K., Nuzzo, R.G. & Whitesides, G.M. Self-assembled monolayers of thiolates on metals as a form of nanotechnology. *Chem. Rev.* **105**, 1103-1169 (2005).
42. Lian, S.C., Weinberg, D.J., Harris, R.D., Kodaimati, M.S. & Weiss, E.A. Subpicosecond Photoinduced Hole Transfer from a CdS Quantum Dot to a Molecular Acceptor Bound Through an Exciton-Delocalizing Ligand. *Acs Nano* **10**, 6372-6382 (2016).
43. Makarov, N.S. et al. Spectral and Dynamical Properties of Single Excitons, Biexcitons, and Trions in Cesium-Lead-Halide Perovskite Quantum Dots. *Nano Lett.* **16**, 2349-2362 (2016).
44. Valeur, B. Molecular Fluorescence Principles and Applications. in *Molecular Fluorescence: Principles and Applications*. (ed. Wiley) 172-173 (Wiley, Germany, 2001).
45. Lakowicz, J.R. *Principles of Fluorescence Spectroscopy*, 961 (Springer, 2006).
46. Tachiya, M. Application of a generating function to reaction-kinetics in micelles. Kinetics of quenching of luminescent probes in micelles. *Chem. Phys. Lett.* **33**, 289-292 (1975).
47. Knowles, K.E., Malicki, M. & Weiss, E.A. Dual-Time Scale Photoinduced Electron Transfer from PbS Quantum Dots to a Molecular Acceptor. *J. Am. Chem. Soc.* **134**, 12470-12473 (2012).
48. Kamat, P.V., Ebbesen, T.W., Dimitrijevic, N.M. & Nozik, A.J. Primary photochemical events in CdS semiconductor colloids as probed by picosecond laser flash photolysis. *Chem. Phys. Lett.* **157**, 384-389 (1989).
49. Hu, Y.Z. et al. Biexcitons in Semiconductor Quantum Dots. *Phys. Rev. Lett.* **64**, 1805-1807 (1990).
50. Beratan, D.N., Onuchic, J.N., Winkler, J.R. & Gray, H.B. Electron-Tunneling Pathways in Proteins *Science* **258**, 1740-1741 (1992).
51. Derr, J.B., Tamayo, J., Espinoza, E.M., Clark, J.A. & Vullev, V.I. Dipole-induced effects on charge transfer and charge transport. Why do molecular electrets matter? *Can. J. Chem.* **96**, 843-858 (2018).

Chapter 3

Title: Bidirectional Solvatofluorochromism of a Pyrrolo[3,2-*b*]pyrrole–

Diketopyrrolopyrrole Hybrid

Authors: Hye Gun Ryu,^{a,b} Maximillian F. Mayther,^c **Jesse Tamayo**,^c Cloé Azarias,^d Eli M. Espinoza,^c Marzena Banasiewicz,^e Łukasz G. Łukasiewicz,^a Yevgen M. Poronik,^a Artur Jeżewski,^a John Clark,^f James B. Derr,^g Kyo Han Ahn,^{b,*} Daniel T. Gryko,^{a,*} Denis Jacquemin,^{d,h,*} Valentine I. Vullevc,^{f,g,i,*}

(a) Institute of Organic Chemistry, Polish Academy of Sciences, Kasprzaka 44-52, 01-224 Warsaw, Poland. (b) Department of Chemistry, POSTECH 77 Cheongam-Ro, Nam-Gu, Pohang, Gyungbuk 37673, Korea. (c) Department of Chemistry, University of California, Riverside, CA 92521, USA. (d) CEISAM laboratory -UMR 6230, University of Nantes 2, rue de la Houssinière, 44322 Nantes, France. (e) Institute of Physics, Polish Academy of Sciences, Al. Lotników 32/46, 02-668 Warsaw, Poland. (f) Department of Bioengineering, University of California, Riverside, CA 92521, USA. (g) Department of Biochemistry, University of California, Riverside, CA 92521, USA. (h) Institut Universitaire de France 1, rue Descartes, 75231 Paris Cedex 05, France. (i) Materials Science and Engineering Program, University of California, Riverside, CA 92521, USA.

Abstract:

Hybridization of electron donors and acceptors provides routes to long-wavelength absorbing and fluorescing dyes. Varying the coupling of low-lying charge-transfer (CT) states with the ground and different locally excited states profoundly affects the photophysics of such donor–acceptor conjugates. Herein, we hybridize an electron-deficient diketopyrrolopyrrole (DPP) moiety with an electron-rich pyrrolopyrrole (PP) that is symmetrically N-arylated with 4-nitrophenyl substituents. The lowest Franck–Condon state is located on the DPP ring structure and dominates the photophysics of the hybrid. Similar to the DPP moiety, the hybrid exhibits optical absorption that is invariant

to the solvent media. The PP donor considerably modulates its fluorescence by undergoing electron transfer to the locally excited DPP to form a CT state. For nonpolar media, an increase in solvent polarity causes a bathochromic shift of the fluorescence reaching the longest wavelengths for chloroform and DCM. A further increase in the medium polarity moves the fluorescence maximum hypsochromically back to where it is for alkane solvents. This bidirectional solvatofluorochromism accompanies a polarity-induced increase in the nonradiative decay rates leading to a decrease in the emission quantum yield. The solvent dependence of the energy level of the CT state is responsible for the observed polarity-induced fluorescence behavior of the hybrid. This emission behavior, along with the solvent invariance of the absorption, results in multimodal sensitivity to the solvation environment.

Introduction:

This article describes the photophysics of the first hybrid compound of pyrrolopyrrole (PP) and diketopyrrolopyrrole (DPP) moieties. Direct arylation of a pyrrolo[3,2-

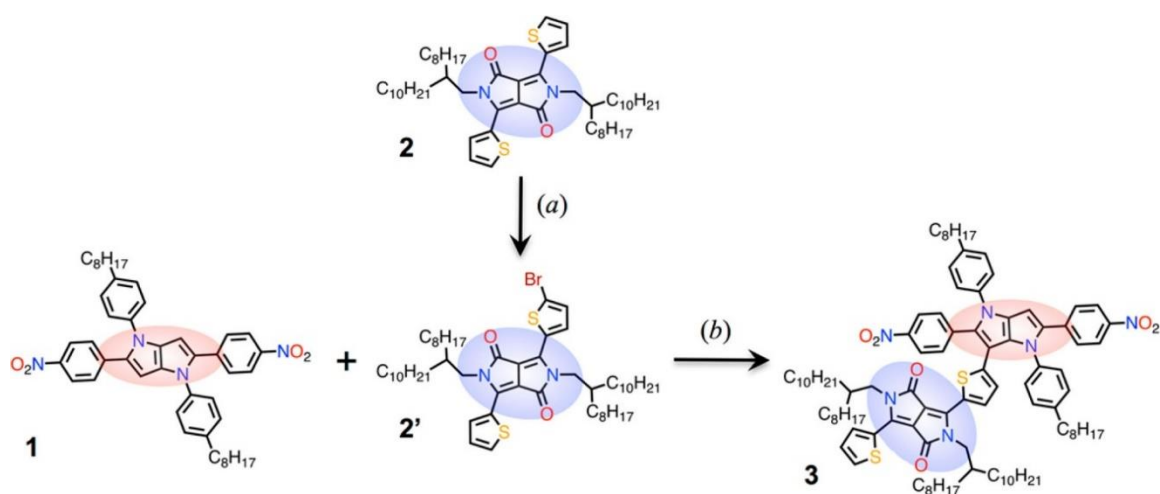


Chart 1 Dyad system showing both the donor and acceptor molecules before and after conjugation.

b]pyrrole, **1**, at position 3 with a dithienyl-DPP derivative, **2'**, readily produces the hybrid, **3** (Chart 1). Charge-transfer (CT) processes, which dominate the excited-state dynamics in media more polar than hydrocarbon solvents, lead to the emergence of photophysical properties of the hybrid that are not inherent to any of the two comprising moieties. To our knowledge, this hybrid manifests the first example of bidirectional solvatofluorochromism.

Advances in biomedical imaging and in solar energy place demands for long-wavelength absorbing dyes with new optical and electronic properties.¹⁻⁴ In this framework, the extension of π -conjugation is a broadly used strategy for lowering the energy of absorption and emission of organic conjugates.⁵⁻⁷ Furthermore, incorporating electron donors and acceptors to form push-pull complexes can also lead to significant bathochromic spectral shifts due to the introduction of a CT character to the Franck-Condon excited states.^{8,9} The pronounced change in polarization upon photoexcitation to CT states, along with variations in the donor-acceptor electronic coupling due to structural rearrangements (e.g., an increase in planarity), make such donor-acceptor conjugates immensely sensitive to solvating environment.⁹ Indeed, strong donor-acceptor electronic coupling can induce hundreds of nanometers red shifts in not only the absorption but also the fluorescence spectra.^{10,11} Conversely, weakening the ground-state donor-acceptor coupling results in negligible perturbations in the optical absorption, while the CT character of the conjugates solely governs their excited-state dynamics.¹²

Unperturbed ground-state absorption, leading to the formation of polarized fluorescent excited states, can result in solvatofluorochromism.^{13,14} That is, solvent polarity affects the position of the fluorescence bands while inducing negligible to no changes in the absorption. Recently, we have discovered that centrosymmetric acceptor–donor–acceptor constructs, composed of an electron-rich pyrrolo[3,2-*b*]pyrrole heterobicyclic core¹⁵⁻¹⁷ and two 4-nitrophenyl substituents as acceptors, display strong solvatofluorochromism.^{18,19} While the donor–acceptor coupling in these constructs is strong, the structural symmetry induces cancellation of the transition dipole moments to any of the dipolar CT excited states, making photoexcitation insensitive to the media polarity. In the excited state, however, an electron transfer to one of the nitrophenyls breaks the symmetry and leads to a polarized state that can efficiently undergo radiative deactivation, making the fluorescence sensitive to the solvent polarity.²⁰

Among the various strongly absorbing dyes with electron-deficient character, some of the most promising platforms include DPP core structures.^{21,22} For instance, suppressed charge recombination in DPP conjugates with donors attached to their lactam nitrogens present unexplored possibilities of these sensitizers for solar-energy applications.¹² Employing a DPP core as an acceptor in strongly polarized centrosymmetric donor–acceptor–donor constructs leads to quadrupolar chromophores that, in addition to their bathochromically shifted absorption and fluorescence, exhibit large two-photon absorption cross sections.^{23,24} The latter is especially true if five-membered rings are attached to the DPP core because they tend to allow for small dihedral angles, leading to enhanced electronic coupling.^{25,26}

Based on the advances in these electron-rich and electron-deficient condensed aromatic cores, herein we focus on a hybrid of DPP and PP. The hybrid has an asymmetric structure of three acceptors (a DPP moiety and two nitrophenyl substituents) connected to a PP donor (Scheme 1). The DPP moiety dominates the excited-state dynamics of the hybrid. The PP introduces solvatofluorochromism. An increase in solvent polarity causes bathochromic and hypsochromic fluorescence shifts for nonpolar and polar media, respectively. Concurrently, polarity induces fluorescence quenching. That is, while the fluorescence maxima of the hybrid are practically the same for hexanes and DMF media, its fluorescence for DMF is much weaker than for hexanes. For chloroform and DCM, the hybrid exhibits the most bathochromically shifted fluorescence. Results from electrochemistry and transient-absorption studies unequivocally show that CT processes in the excited state induce the observed trends in the photophysics of the hybrid. Such excited-state behavior opens doors for multimodal sensitivity to solvation environment.

Experimental section

Synthesis

All chemicals were used as received (Aldrich and TCI) unless otherwise specified. Reagent-grade solvents (DCM, hexane, and toluene) were distilled prior to use. All reported ^1H NMR and ^{13}C NMR spectra were recorded on a 500 MHz instrument. Chemical shifts (δ/ppm) were determined using TMS as an internal reference, and the values of the coupling constants, J , are reported in Hz. Chromatography was performed using silica (Kieselgel 60, 200–400 mesh). For the synthesis of **1**, **2**, and **2'**, we followed published procedures.^{19,26}

3-(5-(2,5-Bis(4-nitrophenyl)-1,4-bis(4-octylphenyl)-1,4-dihydropyrrolo[3,2-*b*]pyrrolo-3-yl)thiophen-2-yl)-2,5-bis(2-octyldodecyl)-6-(thiophen-2-yl)pyrrolo[3,4-*c*]pyrrole-1,4(2*H*,5*H*)-dione (3)

Compound **1** (9 mg, 0.012 mmol), compound **2'** (47.1 mg, 0.05 mmol), KOAc (5 mg, 0.05 mmol), and a catalytic amount of PdCl(C₃H₅)(dppb) (0.3 mg, 0.5 μmol) were placed in a Schlenk flask, which was flushed with argon prior to use. Then, 0.5 mL of dry DMA was added, and the resulting mixture was stirred at 130 °C for 3 days. The residue was purified by silica gel column chromatography (eluent: 2% EtOAc in hexane) and later recrystallized from *i*-PrOH. The obtained crystals (9 mg, 46% yield) were dried under reduced pressure. ¹H NMR (500 MHz, CD₂Cl₂): δ/ppm = 8.83 (d, *J* 3.0 Hz, 1H), 8.73 (d, *J* 3.6 Hz, 1H), 8.01 (d, *J* 8.8 Hz, 2H), 7.98 (d, *J* 8.7 Hz, 2H), 7.65 (d, *J* 4.5 Hz, 1H), 7.31 (d, *J* 8.7 Hz, 2H), 7.29–7.20 (m, 5H), 7.15 (d, *J* 8.0 Hz, 2H), 7.02 (d, *J* 8.0 Hz, 2H), 6.99 (d, *J* 8.0 Hz, 2H), 6.63 (s, 1H), 6.47 (d, *J* 3.6 Hz, 1H), 4.01 (d, *J* 7.4 Hz, 2H), 3.73 (d, *J* 7.3 Hz, 2H), 2.65 (t, *J* 7.6 Hz, 2H), 2.55 (t, *J* 7.7 Hz, 2H), 1.89 (br.s, 1H), 1.72 (br.s, 1H), 1.64 (br.s, 2H), 1.51 (br.s, 2H), 1.38–1.11 (m, 84H + grease residues), 0.92–0.80 (m, 18H + grease residues). ¹³C NMR (126 MHz, CD₂Cl₂): δ/ppm = 161.8, 161.7, 146.5, 145.9, 143.6, 142.5, 140.5 (2 signals), 139.8, 138.6, 136.5, 136.3, 136.1, 135.9, 135.1, 133.4, 132.4, 132.3, 131.5, 130.7, 130.4 (2 signals), 130.2, 129.8, 129.3, 128.5, 128.1, 127.7, 125.7, 123.8, 123.5, 108.3, 107.6, 102.9, 95.3, 71.5, 46.4, 46.2, 38.2, 35.8 (2 signals), 32.3 (3 signals), 32.2, 31.9, 31.7, 31.5 (2 signals), 31.4, 30.4 (4 signals), 30.0 (17 signals) ppm. HRMS (ESI): *m/z* calcd for C₁₀₀H₁₃₈N₆O₆S₂K⁺: 1621.9756 [M+K]⁺; found: 1621.9783.

Absorption and emission spectroscopy

Steady-state absorption spectra are recorded in a transmission mode using JASCO V-670 and PerkinElmer Lambda 35 spectrophotometers. Steady-state fluorescence spectra are measured, also in a transmission mode, with a FluoroLog-3 spectrofluorometer equipped with Delta Diode for the time-resolved emission measurements.^{27,28} The experiments are conducted at room temperature using a 1 cm quartz cuvette. The fluorescence quantum yields, ϕ_f , are determined by comparing the integrated emission intensities of the samples with the integrated fluorescence of a reference sample, rhodamine 101, with a known fluorescence quantum yield, $\phi_f^{(0)}$.

Transient-absorption spectroscopy

The transient-absorption spectra are recorded in transmission mode with 2 mm quartz cuvettes using a Helios pump–probe spectrometer (Ultrafast Systems, LLC, Florida, USA) equipped with a delay stage allowing maximum probe delays of 3.2 ns at 7 fs temporal step resolution.²⁹ Immediately prior to the measurements, all samples are purged with argon. The laser source for the Helios is a SpitFire Pro 35F regenerative amplifier (Spectra Physics, Newport, CA, USA) generating 800 nm pulses (≥ 35 fs, 4.0 mJ per pulse, at 1 kHz). The amplifier is pumped with an Empower 30 Q-switched laser run at 20 W. A MaiTai SP oscillator provides the seed beam (55 nm bandwidth).³⁰ The wavelength of the pump is tuned using an optical parametric amplifier, OPA-800CU (Newport Corporation, Newport, CA, USA), equipped with signal second and forth harmonic generators. For optimal OPA performance, the pulse duration from the amplifier was tuned to 50 fs. The idler is tuned to 1860 nm, and its fourth harmonic, 465

nm (~ 10 μ J per pulse), is used for the pump after attenuation. The power of the signal and the idler prior to the second harmonic generator are stabilized at about 150 mW. Singular value decomposition provides the principal components of the transient-absorption spectra and kinetics. Multiexponential global fits yield the time constants for the decay of the singlet excited states and the rise and decay of the CT states.

Electrochemistry

Cyclic voltammetry is conducted using a Reference 600 Potentiostat/Galvanostat/ZRA (Gamry Instruments), connected to a three-electrode cell, at scan rates of 20–500 mV s^{-1} .^{31,32} Anhydrous DCM is employed for the sample preparation, with different concentrations of tetrabutylammonium hexafluorophosphate, $n\text{-(C}_4\text{H}_9)_4\text{NPF}_6$, as supporting electrolyte. Prior to recording the voltammograms, the samples are extensively purged with argon while maintaining constant volume by adding more of the anhydrous solvent. For each sample, a set of voltammograms is recorded where the electrolyte concentration is increased from 25 mM to 200 mM in steps of 25 mM. The half-wave potentials, $E^{(1/2)}$, are determined from the midpoints between the anodic and cathodic peak potentials for reversible or quasireversible oxidation and reduction.^{32,33} The anodic and cathodic peak potentials are determined from the zero points of the first derivatives of the voltammograms, that is, the potentials where $\partial I/\partial E = 0$ at $\partial E/\partial t = \text{constant}$.³⁴ To correct for potential drifts in the reference electrode (which is SCE, connected with the cell via a salt bridge), ferrocene is used as a standard ($E^{(1/2)} = 0.45 \pm 0.01$ V vs SCE for MeCN, 100 mM Bu_4NBF_4).³⁵ Voltammograms of the standard are recorded before and after each set of measurements. From the dependence of $E^{(1/2)}$ on the

electrolyte concentration, the potential for each neat solvent is estimated from extrapolation to zero electrolyte concentration.^{32-34,36} This method for extrapolation of $E^{(1/2)}$ to zero concentration, however, does not account for potential aggregation with dissociation constants lower than the mM range.³⁷

For spectroelectrochemical measurements, we use an UV/visible light source and a CCD spectrometer that are connected with the cuvette holder via optical fibers (Gamry Instruments). We add 2 mL of the sample solution with supporting electrolyte to a Honeycomb Spectroelectrochemical Cell (Pine Research Instrumentation, Inc.) and connect the platinum electrodes to the Reference 600 potentiostat. Along with the cyclic voltammograms, the intensities, $I(E)$, of the light passing through the working electrode are recorded at different potentials, E , while swiping the voltage. The change in the absorbance, ΔA , for each potential, corresponding to the spectra of the electrochemically formed oxidized or reduced species, is calculated using the intensity at 0 V vs the reference for $I(0)$, i.e., $\Delta A(E) = \log(I(0)/I(E))$.^{12,32,38}

Theoretical calculations

All (TD-)DFT calculations were performed using the Gaussian 09.D01 program. For these calculations, we used tightened self-consistent field (10^{-10} au) and geometry optimization (10^{-5} au) convergence thresholds and a large DFT integration grid (so-called *ultrafine* grid, a pruned 99 590 grid). We performed geometry optimization and frequency calculations for the ground state and the two lowest singlet excited states in two solvents (cyclohexane and dichloromethane). All DFT and TD-DFT calculations used the M06-2X hybrid exchange-correlation functional.³⁹ This functional is known to

provide slightly excessive transition energies but delivers consistent data (high correlation) with experiments. Following the basis set combination approach proposed elsewhere,⁴⁰ we used the 6-31G(d) atomic basis set for determining the geometrical and vibrational parameters, whereas the transition energies were computed with 6-31+G(d). The nature of both the ground state and excited state, that is, their stationary point nature, was confirmed by Hessian calculations that returned 0 (minima) imaginary vibrational modes. Environmental effects were accounted for using the linear response (LR) variant of the polarizable continuum model (PCM)⁴¹ in its nonequilibrium limit for the vertical absorption. For the emission wavelengths, the excited state structures were optimized with the LR-PCM in its equilibrium limit, whereas the emission energies were computed with the corrected LR (cLR)⁴² PCM model in its nonequilibrium limit. Excited states are represented using density difference plots, in which the excited state density was determined at the TD-DFT level using the Z-vector approach. The vibrationally resolved emission spectrum was determined using the FCClasses code^{43,44} applying the Franck–Condon approximation and using default parametric values that were found to be sufficient for obtaining a converged Franck–Condon factor.

Results and Discussion

Design and synthesis

Two recent advances motivate the design of the hybrid with extended π -conjugation, compound **3**: (i) our discovery of a particularly strong solvatofluorochromic behavior of a symmetrically 2,5-dinitrophenylated pyrrolo[3,2-*b*]pyrrole **1**,¹⁹ and (ii) despite the large dihedral angles induced by hindrance in penta- and hexa-aryl-substituted pyrrolo[3,2-

b]pyrroles, aromatic rings at positions 3 and 6 exhibit sufficient electronic coupling with the PP core to affect its electronic properties.⁴⁵ For this study, we choose a dithiophene derivative of DPP, **2**, because thiophene and thiophene-linked substituents cause bathochromic spectral shifts.²⁵ Furthermore, five-membered rings improve π -conjugation due to decreased dihedral angles with respect to the polycyclic core.^{21,25}

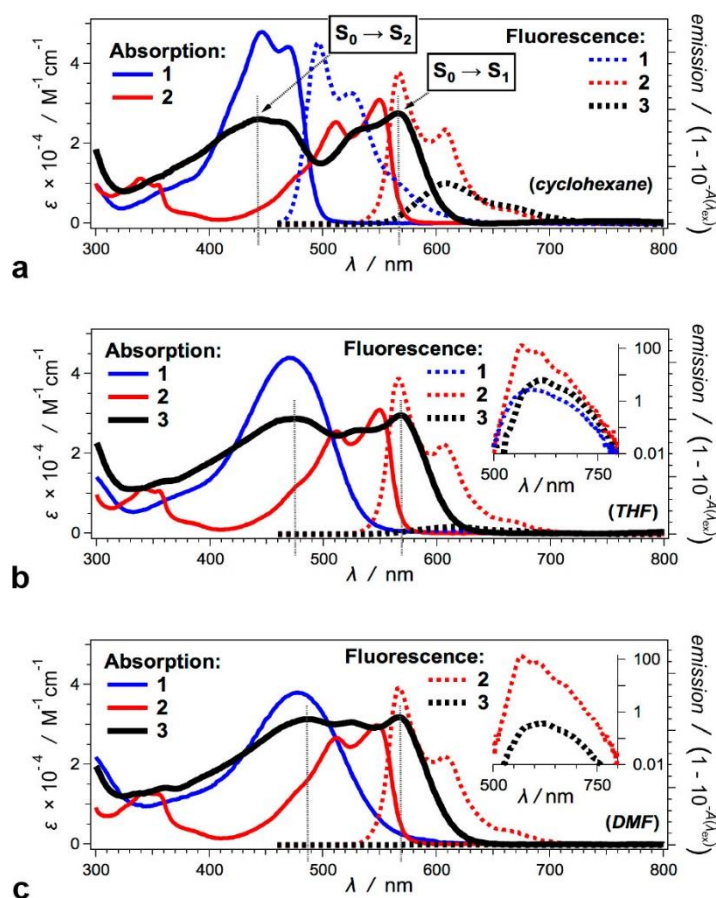


Figure 1. Absorption and fluorescence spectra of 1, 2, and 3, for: (a) cyclohexane, (b) tetrahydrofuran (THF), and (c) *N,N*-dimethylformamide (DMF); the emission of 1 for DMF is not detectable. The fluorescence spectra are divided by the intensity of the absorbed light at the excitation wavelength ($1 - 10^{-4} A(\lambda_{\text{ex}})$), making the integrated emission proportional to ϕ_f . The insets present the fluorescence spectra plotted against logarithmic abscissa ($\lambda_{\text{ex}} = 450$ nm).

Established procedures allow for the synthesis of **2**, and the monobromination of it affords **2'** (Scheme 1).^{26,46} Subjecting the bromide derivative **2'** to optimized conditions for direct arylation⁴⁷ with **1** at its electron-rich pyrrolopyrrole core leads to the formation of the hybrid dye **3** with a reasonable yield (Scheme 1).

Optical Properties of **1**, **2**, and **3**

The absorption spectra of **3** for various solvent media show two transitions: (i) at about 570 nm resembling the absorption of **2** that is bathochromically shifted and (ii) at 460–480 nm, similar to the absorption of **1** shifted about 20 nm to the red (Figures 1 and 2a). Comparison of the spectra of **3** with those of the parent compounds, **1** and **2**, reveals that attaching **1** to one of the thienyl substituents of **2** leads to bathochromic shifts in the absorption (20 nm) and the emission (50–70 nm) (Figures 1 and 2a,b). The Stokes' shifts of **3** are about three-to-four times larger than those of **2** (Figure 2c), which is consistent with an increase in relaxation energy accompanying the optical transitions of **3**.

The fluorescence spectra of **3** are quite like those of **2**. For alkane solvents, the shapes of the emission spectra of **1**, **2**, and **3** closely resemble one another, exhibiting three discernible vibronic features. Toluene, and other solvents with increased polarity, cause a loss in the vibronic structure in the emission of **1**, as previously shown,¹⁹ (52) while the spectral shapes of **2** and **3** remain solvent independent). The long-wavelength absorption bands of **1**, **2**, and **3** follow the same trends. For alkanes, they all show well-defined

vibronic structures (Figure 1a). An increase in solvent polarity does not significantly perturb the absorption spectra of **2** and **3** (the red-edge band of the spectrum of **3**). As the polarity increases, however, the absorption of **1** broadens and loses its vibronic structure observed for alkane solvents (Figure 1). Therefore, it appears that the DPP component, **2**, of the hybrid **3** dominates the transition from the excited to the ground state.

To what extent do the inherent properties of **1** affect the photophysics of **3**? The most obvious similarity between **1** and **3** is the polarity-induced quenching of their fluorescence. While the fluorescence quantum yield, ϕ_f , of **2** has negligible solvent dependence, an increase in medium polarity causes a drastic decrease in ϕ_f of **1** and **3** (Figure 2d). The lifetimes, τ , of the singlet excited state of **3** reveal that solvent polarity enhances the rates of nonradiative decay. While the rate constants of radiative decay, k_f , vary between about 1×10^8 and $4 \times 10^8 \text{ s}^{-1}$, the rate constants of nonradiative deactivation, k_{nr} , increase with solvent polarity by a factor of 200 (Table 1). Therefore, while the DPP component dominates the transitions between S_0 and S_1 states of **3**, the PP moiety strongly affects the nonradiative deactivation of the photoexcited hybrid, **3**.

The solvatofluorochromic behavior of **1** is its most characteristic spectral feature.¹⁹ Increasing solvent polarity causes a fluorescence bathochromic shift exceeding 100 nm, while the absorption of **1** shifts only by about 20 nm (Figure 2a,b). A CT-induced break in the acceptor–donor–acceptor symmetry of the excited state of **1** is the underlying reason for the observed solvatofluorochromism.²⁰

Conversely, **2** exhibits neither solvatochromism nor solvatofluorochromism (Figure 2a–c). Akin to **2**, the red-edge band of the absorption of **3**, ascribed to the $S_0 \rightarrow S_1$ transition, shows no solvent dependence (Figures 1 and 2a). The second absorption band of **3**, ascribed to the $S_0 \rightarrow S_2$ transition, shifts from about 460 to 490 nm with an increase in

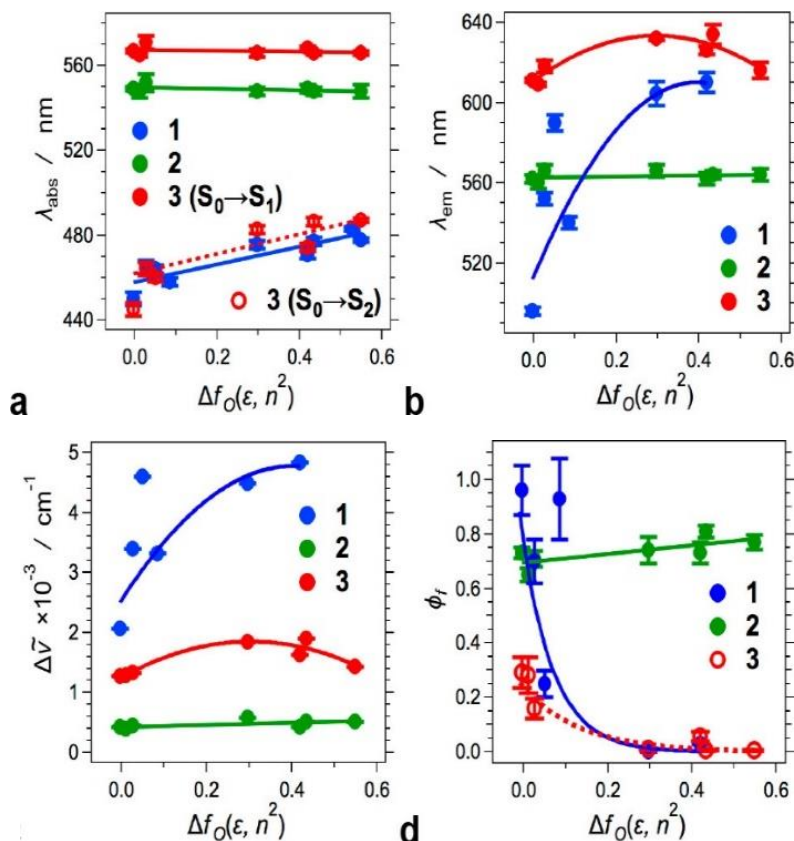


Figure 2 Dependence of photophysical properties of **1**, **2**, and **3** on solvent polarity represented in terms of the Onsager solvation function, $\Delta f_O(\epsilon, n^2) = f_O(\epsilon) - f_O(n^2)$, where $f_O(x) = 2(x - 1)/(2x + 1)$. Solvents used: cyclohexane, *n*-hexane, CCl_4 , toluene, 1,4-dioxane, THF, chloroform, DCM, DMSO, and DMF. Polarity dependence of: (a,b) the wavelengths of the absorption, λ_{abs} , and fluorescence, λ_{em} , maxima, (c) Stokes' shifts, $\Delta\tilde{\nu} = \lambda_{abs}^{-1} - \lambda_{em}^{-1}$, and (d) fluorescence quantum yields, ϕ_f .

the medium polarity (Figure 1). These findings suggest that the solvent polarity lowers the energy level of the S_2 state more than that of the S_1 state.

While the $S_0 \rightarrow S_1$ transition of **3** is insensitive to the solvent medium, **3** manifests a solvatofluorochromic behavior that is quite different from that of **1**. A moderate increase in solvent polarity, e.g., from alkanes to DCM, causes a more than 20 nm bathochromic shift in the fluorescence of **3**. A further increase in the polarity causes a hypsochromic shift (Figure 2b). This property is inherent solely to **3** and appears to emerge from the hybridization of **1** and **2** (Scheme 1).

Theoretical analysis

To identify the nature of the optical transitions, we resort to time-dependent density functional theory (TD-DFT) computations. The electron-density difference (EDD) between the first two excited states and the ground state reveals the nature of the $S_0 \rightarrow S_1$ and the $S_0 \rightarrow S_2$ transitions (Figure 3a). The lowest singlet-excited state, S_1 , responsible for the absorption at about 570 nm, is localized on the DPP unit, with absolutely no contribution from the pyrrolo[3,2-*b*]pyrrole. This state is symmetric and possesses a small CT dipole moment ($\mu_{CT} = 0.7$ D). The $S_0 \rightarrow S_1$ transition does not change the polarity of the hybrid, **3**, which is consistent with the lack of solvatochromism for the long-wavelength absorption band of **3** (Figures 1 and 2a).

In contrast, the second singlet excited state, S_2 , responsible for the absorption at about 470 nm, involves the pyrrolo[3,2-*b*]pyrrole moiety. The $S_0 \rightarrow S_2$ transition moves the electron density from the pyrrolo[3,2-*b*]pyrrole core (in blue in Figure 3a) toward the nitro groups (in red). Comparing **3** with quadrupolar pyrrolo[3,2-*b*]pyrrole, which lacks 3 and 5 substituents, reveals that the presence of the DPP moiety induces a significant asymmetry in S_2 . The intramolecular CT state is significantly biased toward the nitro

group closer to the thienyl linker with DPP. For cyclohexane, TD-DFT predicts a μ_{CT} of 5.9 D for this state. Thus, the $S_0 \rightarrow S_2$ transition significantly polarizes the hybrid, which is consistent with the observed positive solvatochromism of the second absorption band (Figures 1 and 2a). Furthermore, when changing the implemented solvent media in the TD-DFT calculations from cyclohexane to DCM, the first and second vertical absorption bands shift by -0.006 and -0.080 eV, respectively, complementing the experimental results.

To provide further insights into the spectral features of **3**, we identify the emitting states using TD-DFT computations. Optimization of S_1 and S_2 states for cyclohexane (the solvent delivering one of the highest ϕ_f) and DCM (yielding one of the smallest) reveals medium effects on the lowest excited states. For both solvents, the state localized on the DPP core of **3** remains the one presenting the lowest energy after relaxing the excited-state geometries. The close match between the shapes of the experimentally measured and the TD-DFT-determined emission spectra (Figure 3b) confirms that the origin of the observed emission is principally from the lowest excited state localized on the DPP moiety.

Upon transitioning from the ground to the excited state, the dihedral angle between the PP core and the DPP moiety decreases from 58.6° to 41.4° for cyclohexane and from 57.7° to 40.0° for DCM. The electronic transition affects the other dihedral angles to a lesser extent. Therefore, the thiophene linker enhances the π -conjugation between the two components of the hybrid when transitioning from the ground to the excited state. This

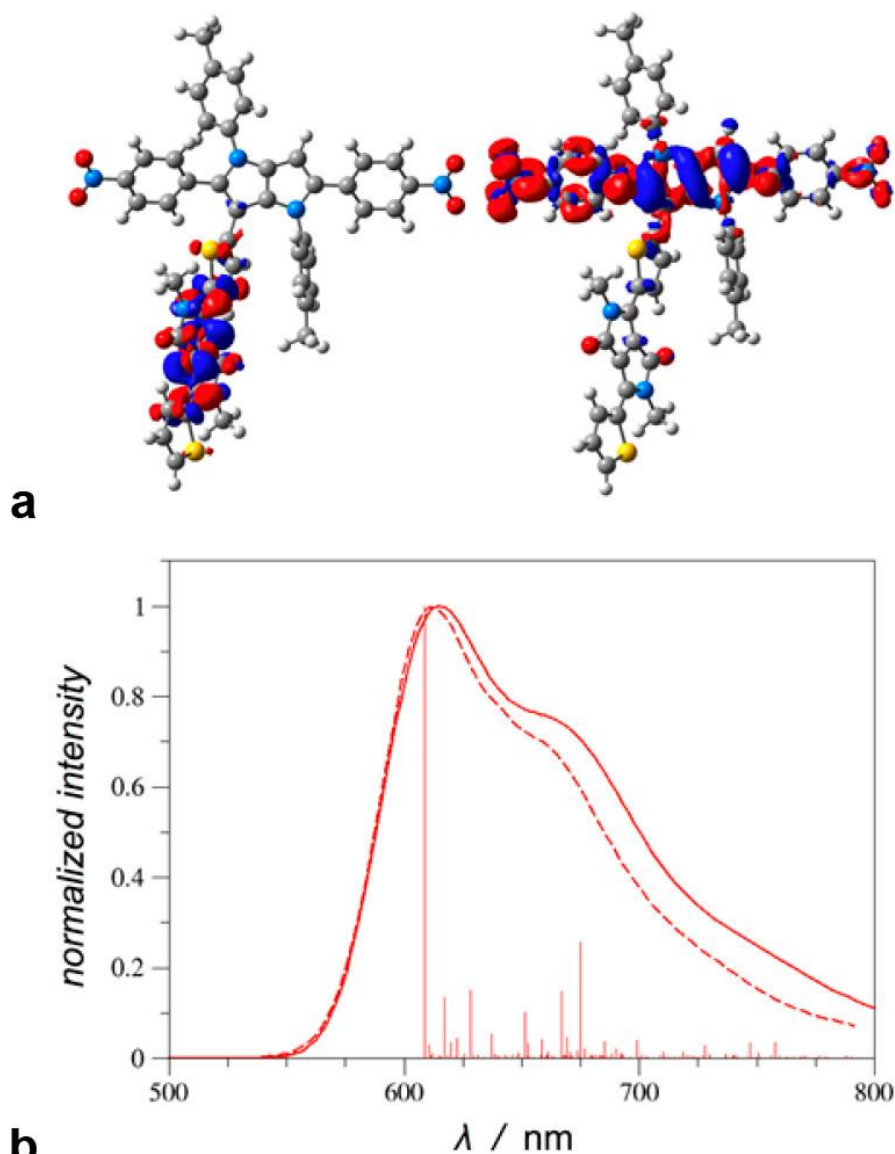
enhancement in the electronic coupling between the PP and DPP moieties in the excited state of **3** causes a small change in the emitting excited state. EDD emission plots, determined for the S_1 geometries, deliver a picture similar to the one for the $S_0 \rightarrow S_1$ transitions but with slightly enhanced contributions on the carbon atoms connecting the DPP and PP units. This difference between the EDDs of the $S_0 \rightarrow S_1$ and $S_1 \rightarrow S_0$ transitions may be indicative for the solvent-induced shifts in the fluorescence spectra of **3**, while the red-edge bands of its absorption remain unaffected.

In the linear-response regime, the computed emission wavelengths for cyclohexane and DCM are 601 and 644 nm, respectively, whereas in the corrected linear-response approach they are 572 and 576 nm, respectively. The computed emission oscillator strengths for the two solvents are large (0.99 for cyclohexane and 1.15 for DCM). Thus, the decrease in ϕ_f with increasing solvent polarity is not a result of a decrease of the intrinsic rates of radiative deactivation of S_1 , which is consistent with the experimental trends (Table 1).

Table 1. Solvent Dependence of the Photophysics of **3**

solvent	$\lambda_{\text{abs}}/\text{nm}^{\text{a}}$	$\lambda_{\text{em}}/\text{nm}^{\text{b}}$	ϕ_f^{c}	$\bar{\tau}/\text{ns}^{\text{d}}$	$k_f \times 10^{-8}/\text{s}^{-1\text{e}}$	$k_{\text{nr}} \times 10^{-8}/\text{s}^{-1\text{f}}$
<i>n</i> -hexadecane	568 \pm 2	616 \pm 3	0.31 \pm 0.07	3.30 \pm 0.33	0.94 \pm 0.29	2.1 \pm 0.3
cyclohexane	567 \pm 1	611 \pm 1	0.29 \pm 0.05	2.46 \pm 0.14	1.2 \pm 0.3	2.9 \pm 0.3
<i>n</i> -hexane	565 \pm 1	609 \pm 1	0.28 \pm 0.07	2.49 \pm 0.19	1.1 \pm 0.4	2.9 \pm 0.4
toluene	571 \pm 3	618 \pm 3	0.16 \pm 0.04	1.02 \pm 0.26	1.6 \pm 0.8	8.2 \pm 0.8
THF	568 \pm 1	626 \pm 2	0.057 \pm 0.018	0.133 \pm 0.016	4.3 \pm 1.8	71 \pm 1.8
chloroform	566 \pm 2	632 \pm 1	0.010 \pm 0.003	0.0383 \pm 0.0059	2.6 \pm 1.1	260 \pm 1.1
DCM	566 \pm 1	634 \pm 4	0.004 \pm 0.001	0.0256 \pm 0.0064	1.6 \pm 0.8	390 \pm 0.8
DMF	566 \pm 1	616 \pm 4	0.004 \pm 0.002	0.0240 \pm 0.0045	1.6 \pm 1.4	410 \pm 1.4

^aWavelength of the absorption maximum of the red-most band of the spectra. ^bWavelength of the fluorescence maximum. ^cBased on measurements, using a methanol solution of rhodamine 101 as a standard. ^dThe intensity-weighted average lifetimes, $\bar{\tau} = (\sum_i \alpha_i \tau_i^2) / (\sum_i \alpha_i \tau_i)$, were obtained from the results from multiexponential fits of the emission decays, $F(\lambda_{\text{em}}, t) = \sum_i \alpha_i \exp(-t/\tau_i)$, or of the decays of the S_1 transient absorption, $\Delta A(\lambda_{\text{S1}}, t)$. ^eAverage rate constant of radiative decay, $k_f = \phi_f / \bar{\tau}$. ^fAverage rate constant of nonradiative decay, $k_{\text{nr}} = (1 - \phi_f) / \bar{\tau}$. The propagated errors for k_f and k_{nr} are the same, estimated for the ratios between ϕ_f and $\bar{\tau}$.



a

b

Figure 3 TD-DFT analysis of the optical transitions of 3, with cyclohexane implemented as the solvation medium. (a) EDD plots for the first (left) and second (right) singlet excited states determined on the ground-state geometry. The blue and red regions indicate decrease and increase of electron density upon absorption, respectively. Contour threshold is set at 0.001 atomic units (au). (b) Comparison between the experimentally measured fluorescence of 3 for cyclohexane (dotted lines) and the computed emission of the DPP core of 3 (sticks and solid line convoluted with a Gaussian of HWHM = 0.08 eV). The theoretical zero-to-zero energy was set to the experimental value to visualize the comparison between band topologies.

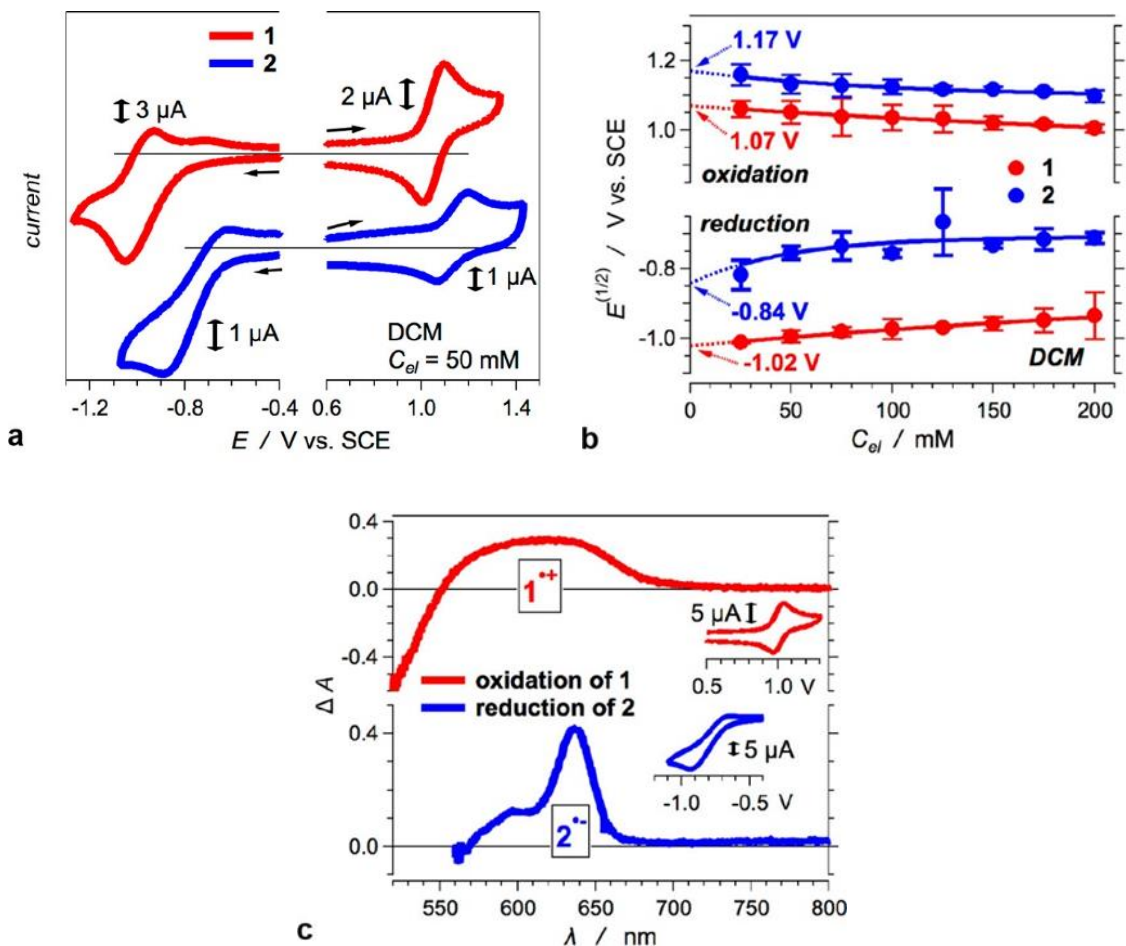


Figure 4 Electrochemical and spectroelectrochemical properties 1 and 2. (a) Cyclic voltammograms showing the reduction and oxidation of 1 and 2 for DCM in the presence of 50 mM electrolyte, $(n\text{-C}_4\text{H}_9)_4\text{NPF}_6$; scan rate 50 mV s^{-1} . (b) Dependence of the half-wave reduction potentials, $E^{(1/2)}$, of oxidation and reduction of 1 and 2 on the electrolyte concentration, C_{el} . (c) Change in absorption during oxidation of 1 and reduction of 2 for DCM in the presence of 100 mM $(n\text{-C}_4\text{H}_9)_4\text{NPF}_6$. The insets show the corresponding voltammograms.

Electrochemical properties of **1** and **2**

For DCM, **1** undergoes chemically reversible oxidation and reduction, and **2** shows reversible oxidation and quasireversible reduction (Figure 4a). The half-wave potentials, $E^{(1/2)}$, show an important trend pointing to the origin of the medium-polarity dependence of the optical properties of **3** (Figure 4). The reduction potentials of the reduction and oxidation of **2** are more positive than those of **1**, i.e., $E_{1\cdot+/1}^{(1/2)} < E_{2\cdot+/2}^{(1/2)}$ and $E_{1/1\cdot-}^{(1/2)} < E_{2/2\cdot-}^{(1/2)}$ (Figure 4b). For DCM, therefore, **1** can act as an electron donor and **2** as an acceptor, when either of them is photoexcited in proximity of each other.^{35,36}

This CT feature is consistent with the solvent dependence of the photophysics of the hybrid. The energy level of the CT state of **3**, $1^{+}2^{-}$, is sensitive to the media polarity. For nonpolar solvents, the CT state lies above the S_1 state, and the radiative deactivation of **3** is of a DPP conjugate. An increase in the solvent polarity lowers the energy level of the CT state below that of the S_1 one, making the photoinduced charge separation (CS), followed by charge recombination (CR), an efficient pathway for a nonradiative transition to the ground state.

The absorption spectra of **3** contain no evidence for direct photoexcitation from the S_0 to the CT state, i.e., no apparent CT band, and no polarity-induced shift of the band at 570 nm (Figures 1 and 2a).^{12,38} While the thiophene linker provides a sufficient electronic coupling to aid CT between the PP donor and the DPP acceptor in **3**, the coupling is not strong enough to make the $S_0 \rightarrow$ CT optical transition possible.

Excited-State Dynamics

Transient absorption (TA) spectroscopy confirms that CT is responsible for the solvent dependence of the excited-state dynamics of the hybrid. Photoexcitation of **3** leads to TA spectra typical for DPP conjugates,¹² showing the ¹DPP* transient along with the ground-state bleach and the stimulated emission (Figure 5). The TA spectra of **3** closely resemble those of **2** even when excited to the S₂ state. The TA spectra of **1**, however, are distinctly different from the spectra of **2** and **3** (Figure 5a–c).

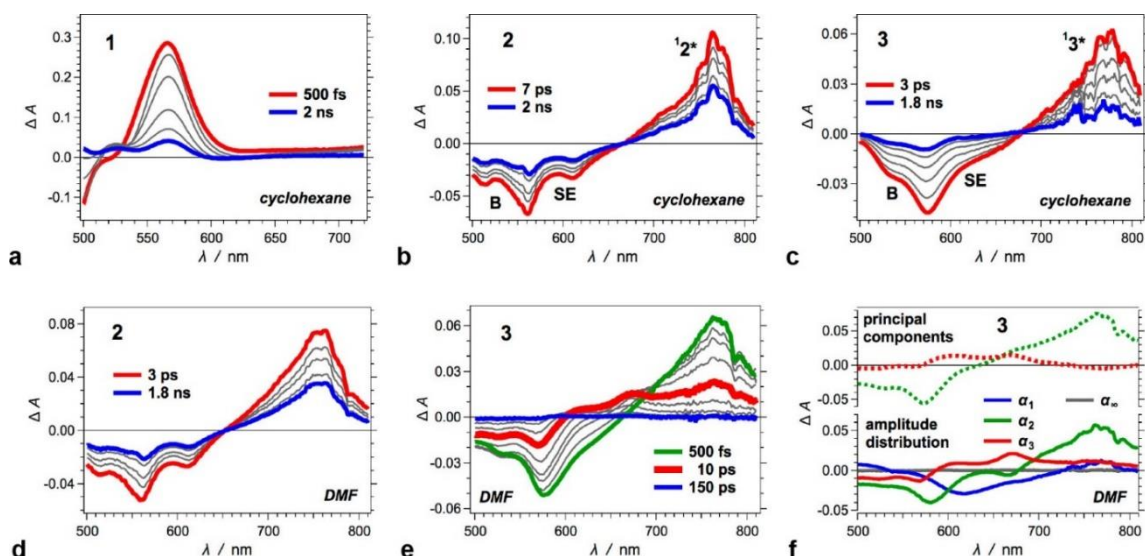


Figure 5 TA dynamics of **1**, **2**, and **3** ($\lambda_{\text{exc}} = 465 \text{ nm}$, $4 \mu\text{J}$ per pulse). (a–c) TA spectra for cyclohexane, showing where the transients of the singlet excited states of **2** and **3** absorb, $1\ 2^*$ and $1\ 3^*$, respectively, along with the stimulated emission (SE) and the ground-state bleach (B). (d,e) TA spectra for DMF. (f) Principal components obtained from singular value decomposition of the TA spectra of **3** for DMF and the distribution of the amplitudes, a_i , from a multiexponential global fit, $\Delta A(\lambda, t) = \alpha_{\infty}(\lambda) + \sum_i a_i(\lambda) \exp(-t/\tau_i)$, where the obtained lifetimes are $\tau_1 = 1.6 \text{ ps}$, $\tau_2 = 7.2 \text{ ps}$, and $\tau_3 = 40 \text{ ps}$.

For nonpolar solvents, **3** undergoes nanosecond decays with TA spectra forming a defined isosbestic point as they decrease in amplitude (Figure 5c). For polar media, however, the picosecond decay of **3** reveals an early rise of TA features between about 580 and 700 nm (Figure 5e). We ascribe these TA features to a CT state, resembling the absorption of **1**^{•+} and **2**^{•-} (Figures 4c and 5e). Regardless of the type of solvent, **2** exhibits TA dynamics similar to that of **3** for nonpolar media (Figure 5b,d). Therefore, the PP moiety in the hybrid appears to provide CT pathways responsible for the polarity-induced fluorescence quenching.

Global fits reveal multiexponential decay of the TA of ¹**3**^{*}, which is plausibly a result of the large size of the hybrid and slow rates of interexchange between conformers. For nonpolar solvents, the multiexponential decays of ¹**3**^{*} lead to bleach recovery and a decrease in the intensity of the stimulated emission, which is consistent with a S₁ → S₀ transition. For polar solvents, the fast decay components of the ¹**3**^{*} accompany a rise of the CT state and depletion of the stimulated emission, without bleach recovery (Figure 5f), which is consistent with CS (e.g., $k_{CS} = 6.1 \times 10^{11} \text{ s}^{-1}$ and $1.5 \times 10^{10} \text{ s}^{-1}$ for DMF and THF, respectively). The slow components of the decay of ¹**3**^{*} appear like a S₁ → S₀ transition, leading to a bleach recovery and not to a growth of the CT state (Figure 5f). The polarity dependence of these slow decay components (e.g., $k_{CS} = 1.4 \times 10^{11} \text{ s}^{-1}$ and $7.0 \times 10^9 \text{ s}^{-1}$ for DMF and THF, respectively), however, suggests the involvement of CT processes. For conformers mediating CR that is faster than CS, the latter is the rate-limiting step, and the sequential CS and CR processes, i.e., S₁ → CT → S₀, appear the same as the S₁ → S₀ transition, i.e., without a buildup of CT TA.¹²

The photophysical properties of the hybrid, **3**, are consistent with transitions involving a nonfluorescent CT state. The absorption of **3** exhibits no solvent dependence. Therefore, we can view the S_1 state as a locally excited state, e.g., $^1\mathbf{3}^* = \text{PP-}^1\text{DPP}^* = \mathbf{1}^1\mathbf{2}^*$. For nonpolar media, the energy level of the CT state, $\mathbf{1}^{+}\mathbf{2}^{-}$, is above that of S_1 , $\mathbf{1}^1\mathbf{2}^*$. Hence, S_1 decays directly to S_0 . Increasing the solvent polarity lowers the CT state.

When the CT state is slightly below but still close to S_1 , mixing between them may cause bathochromic spectral shifts. The TD-DFT studies suggested the possibility for such mixing for the relaxed S_1 state but not for the Franck–Condon excited state. That is, the EDD of the relaxed S_1 state (corresponding to the $S_1 \rightarrow S_0$ transition) shows slightly more density changes localized on the carbons linking DPP with the PP moiety than the EDD on the S_0 minimum (corresponding to the $S_0 \rightarrow S_1$ transition). It is consistent with the fluorescence bathochromic shift for moderately polar solvents, while the $S_0 \rightarrow S_1$ absorption remains unperturbed.

In the Franck–Condon approximation, TD-DFT calculations do not predict the presence of low-lying dark excited states. To avoid the prediction of spurious (nonphysical) CT states,⁴⁸ we select the M06-2X meta-GGA hybrid functional for our calculations, which yields results that agree well with the experimental absorption and fluorescence data. Other functionals, such as B3LYP, may possibly predict low-lying dark CT states, but they would likely be due to self-interaction artifacts, rather than presenting the correct physical description. Higher levels of theory, e.g., EOM-CCSD, would reliably predict the existence of a dark CT state, but they are beyond the reach for systems as large as the hybrid **3**.

Further polarity-induced lowering of the CT state decreases the extent of its mixing with S_1 , causing hypsochromic fluorescence shift for solvents more polar than chloroform and DCM (Figure 2b). The decrease in solvent polarity increases not only the CS driving force, $-\Delta G_{CS}^{(0)}$, but also the outer reorganization energy. Therefore, even for solvents with moderate polarity, such as THF and chloroform, the CS rates are large enough to cause the observed drastic decrease in ϕ_f and τ (Table 1).

Overall, the moderate solvatofluorochromism of the hybrid **3** has a distinctly different origin from the pronounced solvent effect on the fluorescence of its component **1**. The PP **1** is a symmetric acceptor–donor–acceptor conjugate. Breaking the electronic-structure symmetry of the excited state of **1** polarizes it and results in enormous polarity-induced Stokes' shifts that result in the observed solvatofluorochromism.⁽⁵⁴⁾ Conversely, the hybrid **3** has an asymmetric structure, acceptor₁–donor(acceptor₂)–acceptor₁, where acceptor₂ is the DPP moiety. Changes in the solvent polarity modulate the energy of the CT state involving the DPP acceptor. The CT state is coupled with the relaxed S_1 state but not with the Franck–Condon S_1 conformer. Therefore, shifts in the CT energy affect the fluorescence rather than the absorption of **3**.

Conclusions

A few synthetic steps provide routes to a DPP dye hybridized with an electron-rich PP moiety containing electron-deficient nitrophenyl substituents. The red emission of the dye displays pronounced environmental sensitivity, while solvent polarity does not affect its absorption. The invariance of the absorption, along with the polarity-induced fluorescence quenching and the bidirectional solvatofluorochromism of the hybrid dye

(which is positive for nonpolar media and negative for polar), makes this type of molecular design immensely promising for multimodal sensing of the microenvironment based on intensity and the wavelength maximum of the emission signal.

References:

1. Chen, H., Dong, B.L., Tang, Y.H. & Lin, W.Y. A Unique "Integration" Strategy for the Rational Design of Optically Tunable Near-Infrared Fluorophores. *Accounts of Chemical Research* **50**, 1410-1422 (2017).
2. McKenna, B. & Evans, R.C. Towards Efficient Spectral Converters through Materials Design for Luminescent Solar Devices. *Advanced Materials* **29**(2017).
3. Ilic, S., Zoric, M.R., Kadel, U.P., Huang, Y.J. & Glusac, K.D. Metal-Free Motifs for Solar Fuel Applications. *Annual Review of Physical Chemistry, Vol 68* **68**, 305-331 (2017).
4. Meier, H., Huang, Z.S. & Cao, D.R. Double D-pi-A branched dyes - a new class of metal-free organic dyes for efficient dye-sensitized solar cells. *Journal of Materials Chemistry C* **5**, 9828-9837 (2017).
5. Grimsdale, A.C., Chan, K.L., Martin, R.E., Jokisz, P.G. & Holmes, A.B. Synthesis of Light-Emitting Conjugated Polymers for Applications in Electroluminescent Devices. *Chemical Reviews* **109**, 897-1091 (2009).
6. Takeda, T. & Haley, M.M. Synthesis and photophysical properties of expanded dehydrobenzoannulene macrotricycles. *Canadian Journal of Chemistry* **95**, 298-302 (2017).
7. Hissler, M., Lescop, C. & Reau, R. pi-Conjugated systems: Can phosphole offer more than pyrrole? *Pure and Applied Chemistry* **77**, 2099-2104 (2005).
8. Bures, F. Fundamental aspects of property tuning in push-pull molecules. *Rsc Advances* **4**, 58826-58851 (2014).
9. Klymchenko, A.S. Solvatochromic and Fluorogenic Dyes as Environment-Sensitive Probes: Design and Biological Applications. *Accounts of Chemical Research* **50**, 366-375 (2017).

10. Jones, G. et al. Photoinduced electron transfer in arylacridinium conjugates in a solid glass matrix. *Journal of Physical Chemistry B* **111**, 6921-6929 (2007).
11. Benniston, A.C. et al. Charge shift and triplet state formation in the 9-mesityl-10-methylacridinium cation. *Journal of the American Chemical Society* **127**, 16054-16064 (2005).
12. Purc, A. et al. Gating That Suppresses Charge Recombination-The Role of Mono-N-Arylated Diketopyrrolopyrrole. *Journal of the American Chemical Society* **138**, 12826-12832 (2016).
13. Kuwabara, T., Orie, J., Segawa, Y. & Itami, K. Curved Oligophenylenes as Donors in Shape-Persistent Donor-Acceptor Macrocycles with Solvatofluorochromic Properties. *Angewandte Chemie-International Edition* **54**, 9646-9649 (2015).
14. Okamoto, H., Kohno, M., Satake, K. & Kimura, M. An azacrowned phthalimide as a metal-ion sensitive and solvatofluorochromic fluorophore: Fluorescence properties and a mimic integrated logic operation. *Bulletin of the Chemical Society of Japan* **78**, 2180-2187 (2005).
15. Krzeszewski, M. et al. Nonplanar Butterfly-Shaped pi-Expanded Pyrrolopyrroles. *Chemistry-a European Journal* **22**, 16478-16488 (2016).
16. Janiga, A. & Gryko, D.T. 1,4-Dihydropyrrolo 3,2-b pyrrole and Its pi-Expanded Analogues. *Chemistry-an Asian Journal* **9**, 3036-3045 (2014).
17. Janiga, A., Bednarska, D., Thorsted, B., Brewer, J. & Gryko, D.T. Quadrupolar, emission-tunable pi-expanded 1,4-dihydropyrrolo 3,2-b pyrroles - synthesis and optical properties. *Organic & Biomolecular Chemistry* **12**, 2874-2881 (2014).
18. Lukasiewicz, L.G. et al. Symmetry Breaking in Pyrrolo 3,2-b pyrroles: Synthesis, Solvatofluorochromism and Two-photon Absorption. *Chemistry-an Asian Journal* **12**, 1736-1748 (2017).
19. Friese, D.H. et al. Pyrrolo 3,2-b pyrroles-From Unprecedented Solvatofluorochromism to Two-Photon Absorption. *Chemistry-a European Journal* **21**, 18364-18374 (2015).
20. Dereka, B., Rosspeintner, A., Krzeszewski, M., Gryko, D.T. & Vauthey, E. Symmetry-Breaking Charge Transfer and Hydrogen Bonding: Toward Asymmetrical Photochemistry. *Angewandte Chemie-International Edition* **55**, 15624-15628 (2016).
21. Grzybowski, M. & Gryko, D.T. Diketopyrrolopyrroles: Synthesis, Reactivity, and Optical Properties. *Advanced Optical Materials* **3**, 280-320 (2015).

22. Qu, S.Y. & Tian, H. Diketopyrrolopyrrole (DPP)-based materials for organic photovoltaics. *Chemical Communications* **48**, 3039-3051 (2012).
23. Alam, M.M. et al. pi-Extended diketopyrrolopyrrole-porphyrin arrays: one- and two-photon photophysical investigations and theoretical studies. *Physical Chemistry Chemical Physics* **18**, 21954-21965 (2016).
24. Schmitt, J. et al. A Theranostic Agent Combining a Two-Photon-Absorbing Photosensitizer for Photodynamic Therapy and a Gadolinium(III) Complex for MRI Detection. *Chemistry-a European Journal* **22**, 2775-2786 (2016).
25. Burckstummer, H., Weissenstein, A., Bialas, D. & Wurthner, F. Synthesis and Characterization of Optical and Redox Properties of Bithiophene-Functionalized Diketopyrrolopyrrole Chromophores. *Journal of Organic Chemistry* **76**, 2426-2432 (2011).
26. Grzybowski, M. et al. Polar Diketopyrrolopyrrole-Imidazolium Salts as Selective Probes for Staining Mitochondria in Two-Photon Fluorescence Microscopy. *Chemistry-a European Journal* **21**, 9101-9110 (2015).
27. Xia, B., Bao, D.D., Upadhyayula, S., Jones, G. & Vullev, V.I. Anthranilamides as Bioinspired Molecular Electrets: Experimental Evidence for a Permanent Ground-State Electric Dipole Moment. *Journal of Organic Chemistry* **78**, 1994-2004 (2013).
28. Thomas, M.S. et al. Kinetics of Bacterial Fluorescence Staining with 3,3'-Diethylthiacyanine. *Langmuir* **26**, 9756-9765 (2010).
29. Jia, C.C. & Guo, X.F. Molecule-electrode interfaces in molecular electronic devices. *Chemical Society Reviews* **42**, 5642-5660 (2013).
30. Upadhyayula, S. et al. Permanent Electric Dipole Moments of Carboxyamides in Condensed Media: What Are the Limitations of Theory and Experiment? *Journal of Physical Chemistry B* **115**, 9473-9490 (2011).
31. Larsen-Clinton, J.M. et al. Fluorinated aminoanthranilamides: non-native amino acids for bringing proteomic approaches to charge-transfer systems. *Physical Chemistry Chemical Physics* **19**, 7871-7876 (2017).
32. Espinoza, E.M. et al. Nitropyrene Photoprobes: Making Them, and What Are They Good for? *European Journal of Organic Chemistry* **2016**, 343-356 (2016).
33. Larsen, J.M. et al. Building blocks for bioinspired electrets: molecular-level approach to materials for energy and electronics. *Pure and Applied Chemistry* **87**, 779-792 (2015).

34. Espinoza, E.M., Larsen, J.M. & Vullev, V.I. What Makes Oxidized N-Acylanthranilamides Stable? *Journal of Physical Chemistry Letters* **7**, 758-764 (2016).
35. Bao, D. et al. Electrochemical Oxidation of Ferrocene: A Strong Dependence on the Concentration of the Supporting Electrolyte for Nonpolar Solvents. *Journal of Physical Chemistry A* **113**, 1259-1267 (2009).
36. Bao, D. et al. Electrochemical Reduction of Quinones Interfacing Experiment and Theory for Defining Effective Radii of Redox Moieties. *Journal of Physical Chemistry B* **114**, 14467-14479 (2010).
37. Bird, M.J. et al. Effects of electrolytes on redox potentials through ion pairing. *Journal of Electroanalytical Chemistry* **804**, 107-115 (2017).
38. Bao, D.D. et al. Dipole-Mediated Rectification of Intramolecular Photoinduced Charge Separation and Charge Recombination. *Journal of the American Chemical Society* **136**, 12966-12973 (2014).
39. Zhao, Y. & Truhlar, D.G. The M06 suite of density functionals for main group thermochemistry, thermochemical kinetics, noncovalent interactions, excited states, and transition elements: two new functionals and systematic testing of four M06-class functionals and 12 other functionals. *Theoretical Chemistry Accounts* **120**, 215-241 (2008).
40. Le Guennic, B. & Jacquemin, D. Taking Up the Cyanine Challenge with Quantum Tools. *Accounts of Chemical Research* **48**, 530-537 (2015).
41. Tomasi, J., Mennucci, B. & Cammi, R. Quantum mechanical continuum solvation models. *Chemical Reviews* **105**, 2999-3093 (2005).
42. Caricato, M. et al. Formation and relaxation of excited states in solution: A new time dependent polarizable continuum model based on time dependent density functional theory. *Journal of Chemical Physics* **124**(2006).
43. Santoro, F., Improta, R., Lami, A., Bloino, J. & Barone, V. Effective method to compute Franck-Condon integrals for optical spectra of large molecules in solution. *Journal of Chemical Physics* **126**(2007).
44. Santoro, F., Improta, R., Lami, A., Bloino, J. & Barone, V. Effective method to compute Franck-Condon integrals for optical spectra of large molecules in solution (vol 126, pg 084509, 2007). *Journal of Chemical Physics* **126**(2007).
45. Krzeszewski, M., Thorsted, B., Brewer, J. & Gryko, D.T. Tetraaryl-, Pentaaryl-, and Hexaaryl-1,4-dihydropyrrolo 3,2-b pyrroles: Synthesis and Optical Properties. *Journal of Organic Chemistry* **79**, 3119-3128 (2014).

46. Yoo, D. et al. A Timely Synthetic Tailoring of Biaxially Extended Thienylenevinylene-Like Polymers for Systematic Investigation on Field-Effect Transistors. *Advanced Functional Materials* **25**, 586-596 (2015).
47. Alberico, D., Scott, M.E. & Lautens, M. Aryl-aryl bond formation by transition-metal-catalyzed direct arylation. *Chemical Reviews* **107**, 174-238 (2007).
48. Magyar, R.J. & Tretiak, S. Dependence of spurious charge-transfer excited states on orbital exchange in TDDFT: Large molecules and clusters. *Journal of Chemical Theory and Computation* **3**, 976-987 (2007).

Appendix:

Facile synthesis and cleaning of CsPbBr₃ nanocrystals for High Photoluminescence.

Authors: Jesse Tamayo, Cambria Bennett, Pauline Do, Tori Do, Karen El-Maraghy,
Maximillian F. Mayther & Valentine I. Vullev. Underline indicates undergraduate.

Introduction:

All-inorganic perovskites have gained much interest in the past years due to their attractiveness in optoelectronic materials such as photovoltaics, lasers, LEDs and photodetectors. Additionally, their facile synthesis allows for scalability and tunable optical properties. Specifically, by adjusting the halide composition, X, one is able to span the visible spectrum of light. Halides may be either single halide composites of chloride, bromide or iodide or stoichiometric variants of the halide composition such Br_{0.5}/I_{0.5} where some ratio of the halide is used to tune the absorption and emission of the particles.

During the standard synthesis of perovskite crystals, the growth of the crystals can be confined to the nanometer scale by utilizing long chain organic ligands capped by carboxylic acids and amines. The typical synthesis is a hot injection method wherein the size and morphology can be controlled through ligand chain length and reaction temperature. CsPbBr₃ nanocrystals used herein form a cubic phase regardless of halide when the temperature of the synthesis is between 120-200 °C.

Impurity doping such as the addition of Ni^{2+} , cation exchange of Mn^{2+} for Pb^{2+} , and inclusion of Bi^{3+} have been introduced to improve the PLQY and thermal stability. These choices provide great enhancements to the reported PLQY however the drawback is the additional cost of precursors.

Herein, we introduce a systematic study of how proper post-synthetic cleaning of CsPbBr_3 nanocrystals yields particles with high PLQY. We reveal how the photophysics, heterogeneity, and native ligands change during the cleaning process.

Results and Discussion:

Adopting previously reported procedures,¹ we prepare CsPbBr_3 perovskite nanocrystals (NCs) that assume cubic shapes. (TEM 1). Specifically, to produce cesium oleate, CsCO_3 (81 mg, 0.25 mmol) and oleic acid (0.25 mL, 0.8 mmol) were suspended in 4 mL octadecene and stirred at 110 °C for 1 hour under vacuum and placed under nitrogen. In parallel, PbBr_2 (69 mg, 0.19 mmol) was suspended in 5 mL octadecene and also stirred at 110 °C for 1 hour under vacuum and placed under nitrogen. Oleic acid (0.5 mL, 0.16 mmol) and oleylamine (0.5 mL, 0.15 mmol) were injected in the PbBr_2 suspension and the temperature of the mixture was elevated to 150 °C. Concurrently, the temperature of the cesium oleate solution was elevated to 180 °C. A quick injection of the hot cesium oleate solution (0.4 mL) into the vigorously stirred PbBr_2 mixture resulted in the formation of yellow colored suspension with distinct greenish fluorescence. During the hot-injection synthesis in 1-octadecene ($\text{C}_{18}\text{H}_{36}$) solvent, oleylamine ($\text{C}_{18}\text{H}_{35}\text{NH}_2$) and

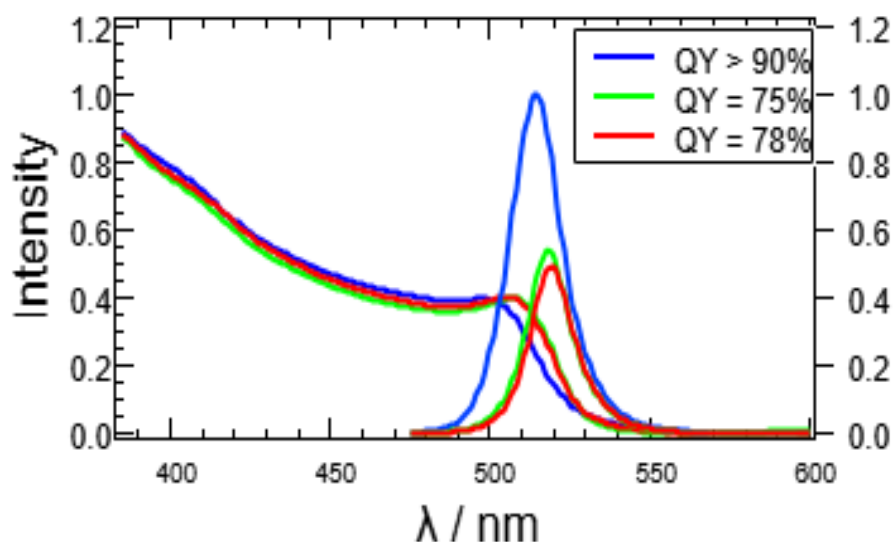


Figure 1 Steady state absorption and photoluminescence normalized to show the difference in quantum yield produced by each supernatant. (SN1-blue trace, SN2-green trace, SN3-red trace).

oleic acid ($C_{17}H_{33}CO_2H$) coat the formed NCs and maintain their structural integrity and colloidal stability in hydrocarbon solvents.

The reaction mixture was immediately cooled down in a water bath. Addition of 1 mL acetone to the cooled mixture and centrifugation at 10,000 rpm for 3 minutes resulted the formation of a yellow pellet that was collected and resuspended in 0.600 ml benzene.

This solution was centrifuged for 30 seconds at 10,000 rpm and the supernatant (SN1) was collected. This process was repeated 2X more times and the supernatant (SN2 and SN3) retained each time. Transmission electron microscopy (TEM) images of the supernatant confirmed the formation of the NCs.

Each of the 3 supernatant samples were analyzed via UV-Vis absorbance, steady state fluorescence, time correlated single photon counting (TCSPC), ^1H -NMR, and TEM.

UV-Vis absorbance (fig. 1) spectra were recorded on a Jasco-V670 UV-Vis absorption

spectrophotometer. Spectra were collected from 650 nm to 350 nm and baseline corrected. The optical density at 400 nm was held between 0.4 and 0.6. The absorbance of SN1 (blue trace) shows a hypsochromic shifted band edge. This shift is indicative to the monodispersity of the sample yielding a smaller edge length of nanocrystals. In comparison, SN2 and SN3 (green and red trace) are bathochromically shifted relative to SN1. The nanocrystal distribution observed via TEM unequivocally shows a greater size distribution trending towards larger sizes.

The steady-state emission spectra and the time-correlated single-photon counting (TCSPC) fluorescence decays are measured, using a FluoroLog-3 spectrofluorometer (Horiba-Jobin-Yvon, Edison, NJ, USA), equipped with a pulsed diode laser ($\lambda = 406$ nm, 196 ps pulse width).

The steady-state emission was collected with 1 nm slit width on both excitation (400 nm) and emission windows. Spectra was collected in the range of 415 nm to 600 nm. The optical density at excitation was held to 0.1-0.2 to ensure inner filter effects were minimized. The photoluminescence quantum yield (PLQY) was recorded for each sample. The quantum yield is calculated by equation 1

$$\Phi_{PL} = \Phi_{Ref} \chi \frac{n_{NC}^2}{n_{Ref}^2} \chi \frac{[Area]_{NC}}{[Area]_{Ref}} \chi \frac{1-10^{-Abs_{Ref}}}{1-10^{-Abs_{NC}}} \quad (1)$$

Where Φ_{Ref} is the quantum yield of the reference i.e. fluorescein (PH 10 buffer) and n_{NC} and n_{Ref} represent the refractive indices of the solvents used, benzene and water respectively. $[Area]_{NC}$ and $[Area]_{Ref}$ represent the integrated PL of the respective samples. Abs_{Ref} and Abs_{NC} are the absorbance of the samples at 400 nm. The limitation to this method is that the QY is a function of the reference standard.

SN1 shows the highest PLQY exceeding 90% is all samples. This sample has the best monodispersity amongst all samples. Considering the photoluminescence quantum yield can also be expressed as equation (2). Wherein k_{PL} , k_{nr} , k_t are the rate constants of photoluminescence, non-radiative dissipation, and energy transfer, respectively. In this instance the PLQY is determined by the rate constants of these non-radiative processes as they compete with photoluminescence.

$$\Phi_{PL} = \frac{k_{PL}}{k_{PL} + k_{nr} + k_t}$$

(2)

It can be said that k_{PL} has increased which contributes to the increase in quantum yield. There are two possibilities as to why k_{PL} has increased. One is that the reduction in concentration of non binding ligands, i.e. octadecene as the synthesis solvent, which has

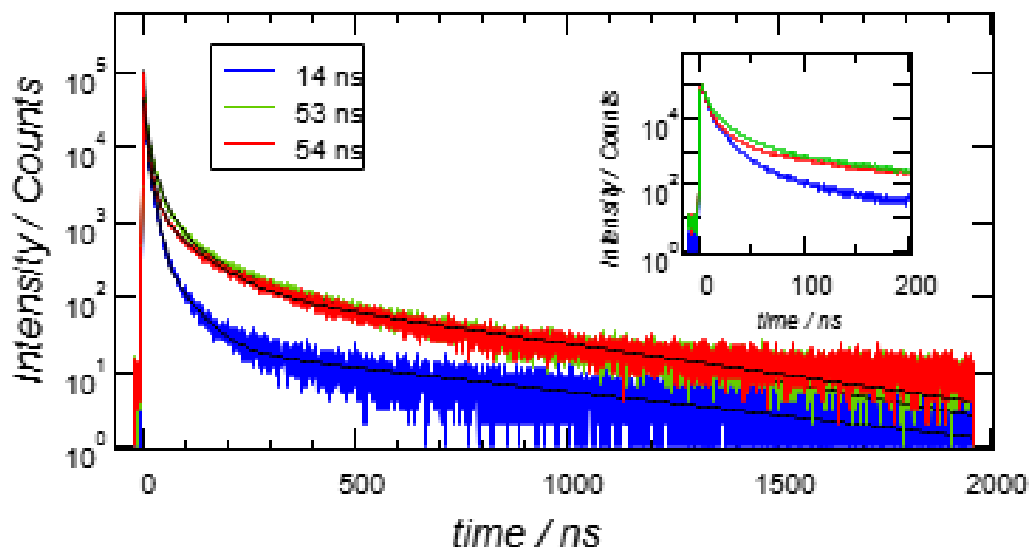


Figure 2 TCSPC decays shows a decrease in the PL lifetime of SN1 which exhibits the highest PLQY. Inset: Early time of the decays shows a nearly monoexponential decay after 50 ns.

been reduced in the cleaning process enables the primary amine containing ligand, oleylamine to easily reach the surface of the nanocrystal and passivate any surface traps caused by crystal lattice imperfections. The second is that since there is an increase in the monodispersity of the sample compared to SN2 and SN3 the emission averaging is more defined. To better answer these possibilities, we examined the PL lifetimes for each supernatant. (fig 2) The PL lifetime can be analyzed via the following equation, (3) and by fitting with multiexponential formulas.

$$\tau_{PL} = \frac{1}{k_{PL} + k_{nr} + k_t} \quad (3)$$

Each supernatant was examined via TCSPC and each decay fit with multiexponential decay functions and the lifetime is reported as an average lifetime (τ) given by equation

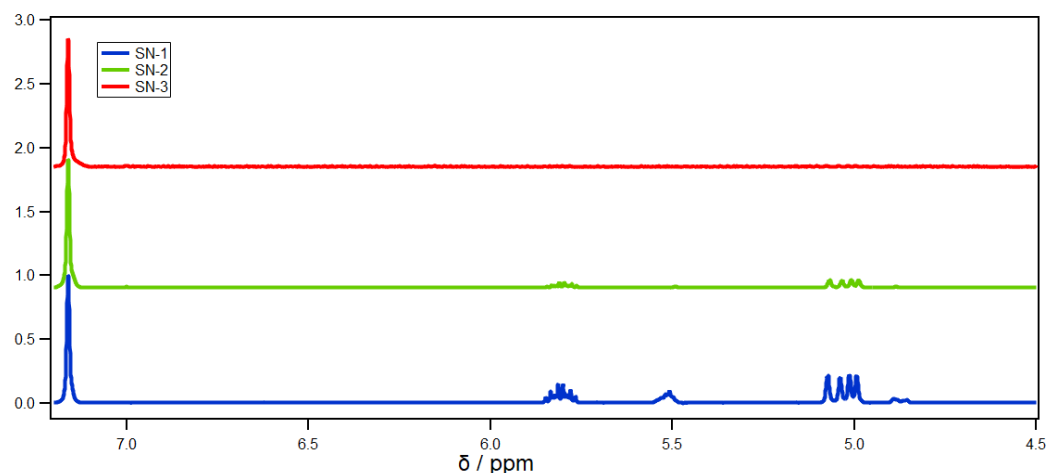


Figure 3 Supernatants 1-3 show gradual decrease of octadecene 5.7 and 5.0 and also oleylamine and oleic acid 5.5.

$$\bar{\tau} = \frac{\alpha_1 \tau_1^2 + \alpha_2 \tau_2^2}{\alpha_1 \tau_1 + \alpha_2 \tau_2} \dots \dots \dots (4)$$

The average lifetimes reveal indeed SN1 has a superior average lifetime of 14 ns while SN2 and SN3 have closely spaced lifetimes of 53 and 54 ns respectively. Considering equation 3 and the fact that the monodispersity of SN1 is improved over the other samples and the possibility of trap suppression we can easily conclude the decreased lifetime is a product of both of these factors.

While the photophysics can provide us with some information to formulate conclusions proton NMR also is useful when determining the concentration of organic ligands and solvent molecules present with the nanocrystals. The successive washing of the particles and redispersion in hexane shows a gradual decrease in octadecene and oleylamine and oleic acid two important ligands (fig 3) to the colloidal stability of the nanocrystals.

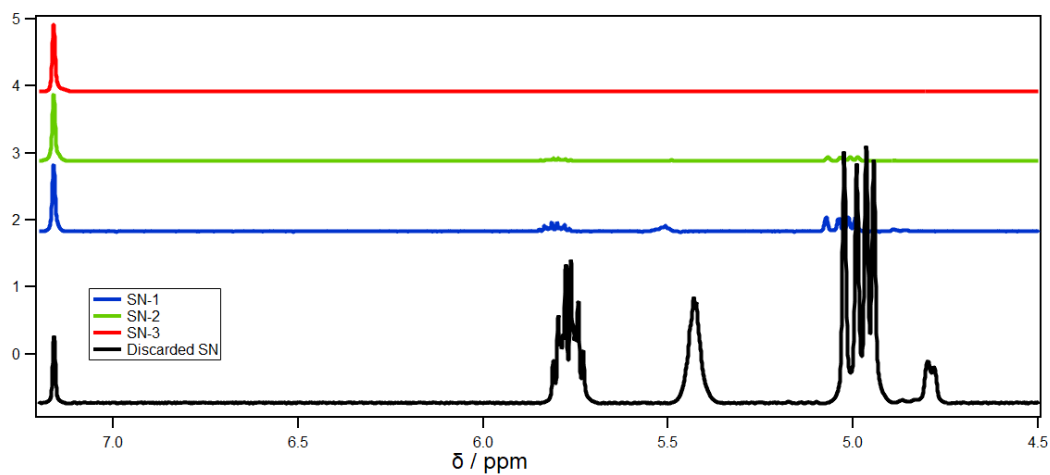
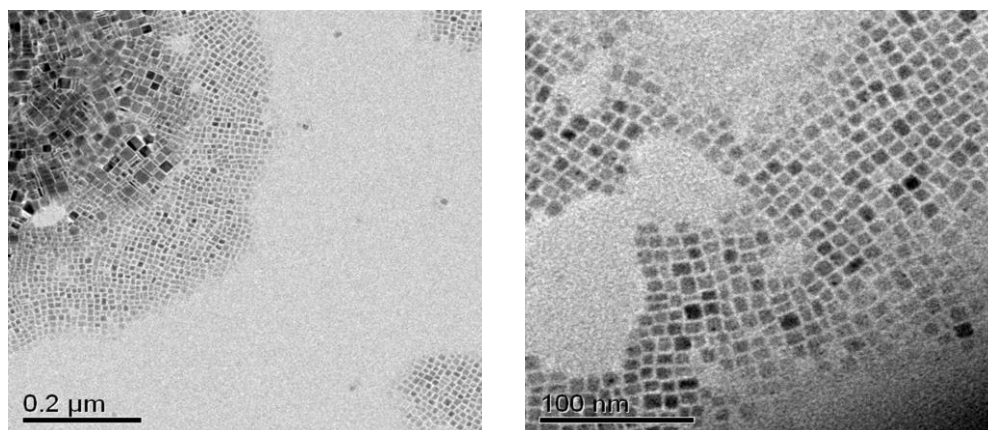
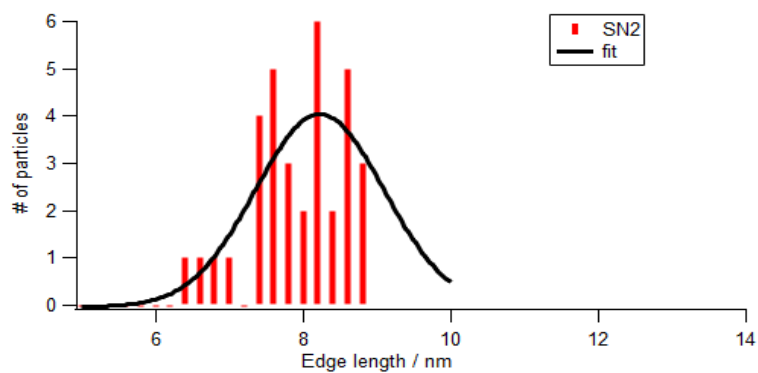


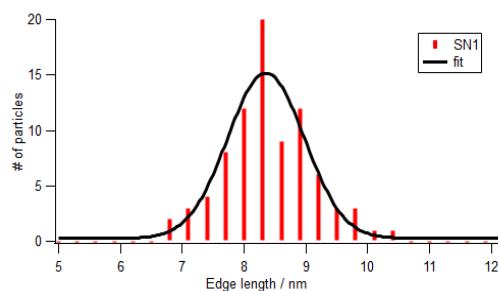
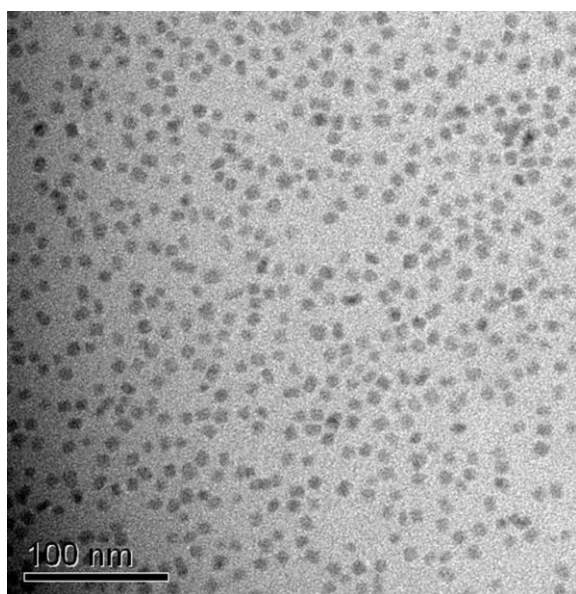
Figure 4 NMR spectra showing the original discarded supernatant for comparison of the relative concentration decrease of solvent and ligand molecules



TEM 2 SN2 A wide view and close in view of the sample shows the major change in dispersity regarding the nanocrystal sizes and the increase in nanocrystal size 9.0 nm and std. dev. 1.23 nm.



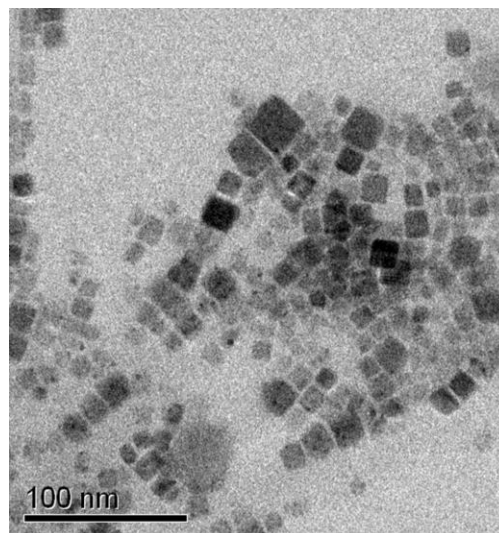
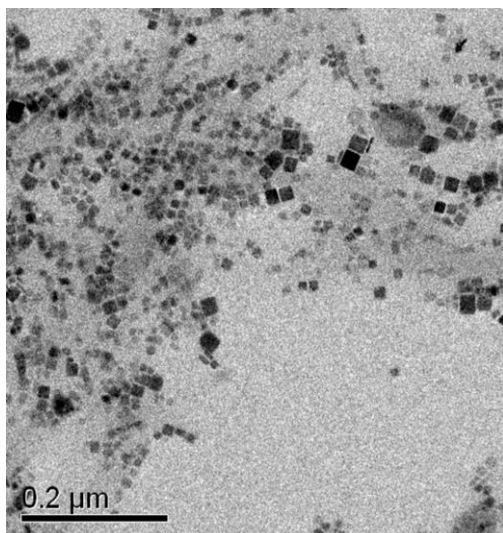
TEM provides a solid means to ascertain the size distribution and dispersity of the particles. The images clearly shows a decrease in the monodispersity of the samples. Importantly the average edge length does not vary much but the standard deviation more than doubles as we examine the supernatants.



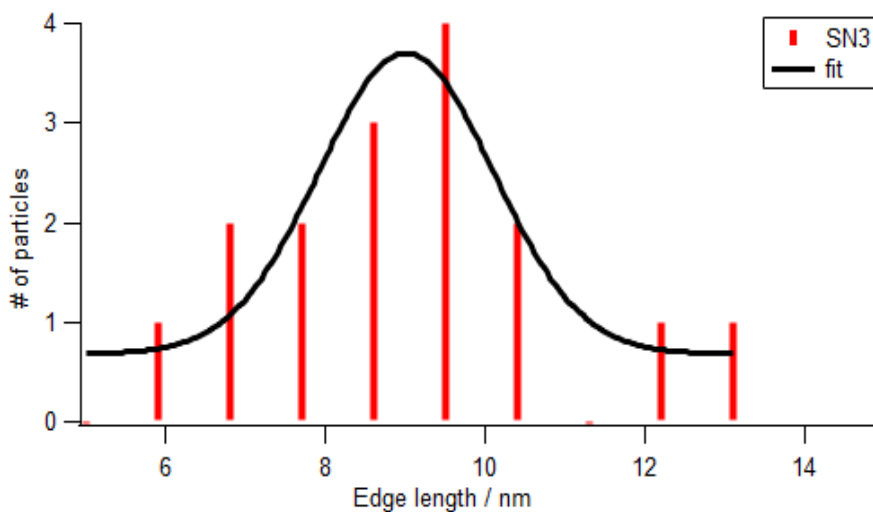
Sample	<Edge length>	Std. Dev.
SN1	8.40	0.87
SN2	9.17	1.23
SN3	9.00	1.54

TEM 1 SN1 shows monodisperse nanocrystal sizes along with histogram which shows an edge length of 8.4 nm with a std. dev. of 0.87 nm. The lowest edge size and std. dev. of the three samples.

Of consideration is when comparing the NMR to the TEM we can see the ligand density decrease while the nanocrystal monodispersity increases. The is similar to what was observed in my work regarding interfacial charge transfer in that where the ligand density is perturbed the presence of larger crystals grows larger. More work would need to be done to analyze the relative change in total volume of nanocrystals to understand if the particles are aggregating or being etched.



TEM 3 SN3 The wide view clearly shows the larger abundance of nanocrystals and a wide range of size distributions. The nanocrystals average edge length is 9.0 nm with a std. dev of 1.54 nm.



Conclusion:

A simple method to synthesized and clean CsPbBr₃ nanocrystals has been investigated as to the role of using an antisolvent in the cleaning procedure and how it affects the photophysics, sample monodispersity, and ligand loading. The superior supernatant has

the most ligands after cleaning, the best monodispersity, highest PLQY and improved PL lifetimes.

This method uses simple antisolvent without extra precursors that are required in doping methods. This method is easily scaled upon batch size and has implications for perovskite synthesis and interfacial modifications.

References:

1. Protesescu, L. et al. Nanocrystals of Cesium Lead Halide Perovskites (CsPbX_3 , X = Cl, Br, and I): Novel Optoelectronic Materials Showing Bright Emission with Wide Color Gamut. *Nano Letters* **15**, 3692-3696 (2015).
2. De Roo, J. et al. Highly Dynamic Ligand Binding and Light Absorption Coefficient of Cesium Lead Bromide Perovskite Nanocrystals. *Acs Nano* **10**, 2071-2081 (2016).
3. Schreckenbach, G. Differential Solvation. *Chemistry-a European Journal* **23**, 3797-3803 (2017).